

Structural and Machine Design Using Piezoceramic Materials

A Guide for Structural Design Engineers

Final Report to NASA Langley Research Center

NASA Grant Number NAG-1-1998

Grant Monitor Renee C. Lake

April 30, 2000

Prepared by:

Daniel J. Inman & Harley H. Cudney

Center for Intelligent Materials Systems and Structures

Virginia Polytechnic Institute and State University

Contact Information:

Telephone: 540-231-2900

E-mail: cimss@vt.edu

Table of Contents

<u>Synopsis</u>	1
<u>I. Introduction to Piezoelectric Materials</u>	2
<u>Historical Development of Piezoelectric Ceramics</u>	2
<u>II. Solid-State Physics of Piezoelectric Ceramics</u>	5
<u>Introduction</u>	5
<u>Piezoceramic Classifications</u>	6
<u>Hard Piezoceramics</u>	6
<u>Soft Piezoceramics</u>	8
<u>Notation</u>	9
<u>Polarization and the Resulting Piezoelectric Actions</u>	11
<u>Piezoelectric Material Descriptive Coefficients and Properties</u>	13
<u>Physical Properties</u>	13
<u>Dielectric Properties</u>	15
<u>Piezoelectric Properties</u>	16
<u>Thermal Considerations</u>	19
<u>III. Circuit Model of Piezoceramics</u>	20
<u>Introduction</u>	20
<u>Electrical impedance of a piezoceramic</u>	21
<u>Experimental verification of electric impedance of PZT</u>	24
<u>Experimental verification of two different circuit models</u>	25
<u>Experimental confirmation of a selected PZT model</u>	26
<u>Summary</u>	28
<u>IV. Mathematical Modeling of Bending Actuators</u>	30
<u>Piezoceramic Actuators</u>	31
<u>Mathematical modeling of Unimorph and Bimorph beam type actuators</u>	33
<u>The Pin-Force-Model</u>	34
<u>Enhanced Pin-Force-Model</u>	37
<u>Euler-Bernoulli Model</u>	39
<u>Symmetric Model - Bimorph</u>	39
<u>Unsymmetric Model - Unimorph</u>	43
<u>Multilayer Actuator - Energy Based Derivation of the Governing Equations</u>	45
<u>Example Section</u>	50
<u>Energy Method</u>	50
<u>Classical Beam Theory</u>	53
<u>Predicted Results</u>	58
<u>Comparison of Pin-Force, Enhanced Pin-Force and Euler-Bernoulli Models</u>	58

<u>Comparison of the Unimorph and Bimorph Structures</u>	63
<u>FEM-Comparison</u>	65
 <u>V. Design of a MIMO Plate Control Testbed</u>	67
<u>Introduction</u>	67
<u>Modeling</u>	67
<u>Piezo-electronics design</u>	69
<u>Actuator Amplifiers and Smoothing Filters</u>	69
<u>Sensor Design</u>	71
<u>Summary</u>	74
 <u>VI. Electronics Design for Piezoelectric Systems</u>	76
<u>A Self-Sensing Piezoelectric Actuator for Collocated Control</u>	77
<u>Introduction</u>	77
<u>Presentation of the Self-Sensing Actuator</u>	77
<u>Implementation of Piezoelectric Actuators and Sensors</u>	78
<u>Piezoelectric Strain Sensor</u>	78
<u>Piezoelectric Rate of Strain Sensor</u>	79
<u>Self-Sensing Actuator</u>	80
<u>Rate of Strain Sensing with the Self-Sensing Actuator</u>	80
<u>Experimental Results</u>	83
<u>Summary</u>	84
<u>Design of Sensoriactuators</u>	84
<u>Introduction</u>	84
<u>Strain rate analog compensation</u>	84
<u>Hybrid Digital/Analog compensation</u>	85
<u>Two-weight Analog Compensator</u>	88
<u>Tuning the compensator</u>	90
<u>Experiments and results</u>	91
<u>Summary</u>	91
<u>Power Factor Correction</u>	91
<u>INTRODUCTION</u>	91
<u>THEORETICAL DEVELOPMENT</u>	92
<u>IN PRACTICE</u>	94
<u>EXAMPLE WITH RESULTS</u>	95
<u>Shunted Piezoelectric Materials</u>	96
<u>Introduction</u>	96
<u>Inductive (Resonant) Shunting</u>	96
<u>Resistive Shunting</u>	97
<u>Capacitive Shunting</u>	98
<u>Switched Shunting</u>	99

<u>Summary</u>	99
<u>VII. Application: Adding Damping to a Plate</u>	100
<u>Positive Position Feedback (PPF)</u>	101
<u>dSPACE and Simulink Block Diagram</u>	102
<u>Active Control Test Setup and Procedure</u>	103
<u>Active Control Test Results</u>	105
<u>VIII. Impedance-based Health Monitoring Technique</u>	110
<u>Implementing the NDE in the Test Setup</u>	111
<u>Health Monitoring Results</u>	112
 IX. Mathematical Symbols.....	115
 X. Suppliers of Piezoceramic Materials and Engineered Actuators.....	116
 <u>XI. References</u>	117
<u>Smart Materials/Actuators</u>	117
<u>Actuators (General)</u>	119
<u>Plates</u>	119
<u>Modeling Piezoelectric Materials</u>	122
<u>Piezoelectric Systems</u>	122

Synopsis

Using piezoceramic materials is one way the design engineer can create structures which have an ability to both sense and respond to their environment. Piezoceramic materials can be used to create structural sensors and structural actuators. Because piezoceramic materials have transduction as a *material* property, their sensing or actuation functions are a result of what happens to the material. This is different than discrete devices we might attach to the structure. For example, attaching an accelerometer to a structure will yield an electrical signal proportional to the acceleration at the attachment point on the structure. Using an electromagnetic shaker as an actuator will create an applied force at the attachment point. Active material elements in a structural design are not easily modeled as providing transduction at a point, but rather they change the physics of the structure in the areas where they are used. Hence, a designer must not think of adding discrete devices to a structure to obtain an effect, but rather must design a structural system which accounts for the physical principles of all the elements in the structure.

The purpose of this manual is to provide practicing engineers the information necessary to incorporate piezoelectric materials in structural design and machine design. First, we will review the solid-state physics of piezoelectric materials. Then we will discuss the physical characteristics of the electrical—active material—structural *system*. We will present the elements of this system which must be considered as part of the design task for a structural engineer. We will cover simple modeling techniques and review the features and capabilities of commercial design tools that are available. We will then cover practical how-to elements of working with piezoceramic materials. We will review sources of piezoceramic materials and built-up devices, and their characteristics. Finally, we will provide two design examples using piezoceramic materials, first as discrete actuators for vibration isolation, and second as structurally-distributed sensor/actuators for active acoustic control.

I. Introduction to Piezoelectric Materials

Historical Development of Piezoelectric Ceramics

Piezoceramic materials are not new. In this section we briefly review the history of piezoceramic materials to convey an appreciation of the science of piezoelectric material applications and a sense of how piezoelectric materials were developed. Historical details can be found in many texts including those by Cady (1946), Mason (1950), Shields (1966), Jaffe (1971) and Ikeda (1990). Much of what is written in this section is greatly expanded in these texts.

The history of piezoelectricity dates to 1880 when Pierre and Jacques Curie first discovered the piezoelectric effect in several substances. The most noted of these substances were Rochelle salt, quartz, and tourmaline. Quartz and tourmaline occur naturally, while Rochelle salt can be crystallized from potassium sodium tartrate.

The discovery of piezoelectricity by the Curie brothers was not an accident. Pierre Curie had studied the relationship between pyroelectricity and crystal symmetry. From his studies, he was led to look for piezoelectricity in substances possessing certain crystalline structures. Further, he surmised which direction to apply pressure in order to manifest the piezoelectric effect.

Piezoelectricity derives its name from the Greek word "*piezo*" which means pressure, so the literal translation is "pressure electricity." Certain materials and substances have the property of generating a charge (or voltage) when pressure is applied to them. Conversely, their shape changes when the material is in an electrical field. Thus, piezoelectricity is a coupling between electrical and mechanical systems, which we will call transduction. The *direct* piezoelectric effect is the electric polarization that is developed through mechanical pressure applied to the material. The *converse* effect is the development of material strain in response to the application of an electrical field. In piezoceramic materials, both the direct and converse effects are fundamentally due to the properties of the crystalline structure of the material.

In the direct effect use of piezoelectric materials, the magnitude of the voltage generated by an applied pressure ranges from a fraction of a volt to several thousand volts. The factors influencing the voltage generated include the macroscopic size and the particular microstructure of the material. In the converse effect application of piezoceramic materials, the magnitude of the strain is likewise a function of the material geometry and microstructure. Strain values are directly related to the magnitude of the applied electric field.

From its discovery until early in the twentieth century, piezoelectricity was predominately a scientific curiosity. In 1916, Paul Langevin of France developed the first engineering use of piezoelectricity by developing an ultrasonic submarine detector. The device, called the "Langevin type transducer", used a quartz element sandwiched between two metal plates. The plates, when excited by the quartz, emitted sound waves into the water. A second quartz device was used to measure the rebounding waves. The time between the emitting and receiving signals was measured and used to calculate the distance to the reflecting source. While the device was quite crude and rudimentary, it was the forerunner to the sonar devices in widespread use today.

In 1917, a conference under the direction of Robert A. Milliken and sponsored by the National Research Council was convened. At this meeting, Langevin's transducer was publicly announced. Walter G. Cady was invited to participate in the conference because of his interest in submarine detection methods. This announcement and other discussions at the conference sparked Cady's interest in piezoelectricity. Cady subsequently embarked on a lifelong journey in developing piezoelectric principles and applications. Much of the progress and development of piezoelectricity from 1917 through the 1940s is solely due to this man's work. Cady should be noted as a pioneer in the area.

As knowledge of the phenomena moved from the laboratory users to application engineers, many uses for piezoelectric materials were developed. During the 1930's, the microphone and the crystal phonograph pickup were developed. The crystal ADP (ammonium-dihydrogen-phosphate) was developed in the mid-1930's. This crystal possessed the rugged characteristics of quartz and the strong piezoelectric characteristics of Rochelle salt. EDT (ethylene diamine tartrate), DKT (dipotassium tartrate), BaTiO_3 (), and ADP are the significant materials among the many piezoelectric crystals to be discovered during the period of time from the 1930's through the 1950's.

The developments in quartz crystals lead to radio communications advances. During the 1940s, researchers at Bell Telephone Laboratories led the development of wave filters in multi-channel telephony work. In World War II, the United States alone used over 50 million quartz crystal elements, primarily in communication devices.

Barium titanate was first produced in 1940. It was the first of the *Perovskite* family of ferroelectric crystals to receive recognition as a piezoceramic. This discovery came about through the work in the area during World War II. Barium titanate is a ferroelectric ceramic and has piezoelectric properties very similar to Rochelle salt, but with the advantages that it is not water-soluble and can withstand higher operating temperatures. Also, many physical shapes can be achieved with Barium titanate because it is a ceramic substance.

Shortly after the development of Barium titanate, ceramic materials possessing better piezoelectric and physical properties were developed. The most notable of these materials are lead metaniobate (PMN) and lead zirconate titanate (PZT) and to date are among the most used of piezoelectric materials in structural and acoustic applications. These developments were followed by the development of piezoelectric semiconductor film transducers and piezoelectric polymers. The piezoelectric polymer in longest use is polyvinylidene fluoride film (PVDF), and other copolymer films with piezoelectric properties are being produced.

The development of PMN and PZT materials has been on-going since the 1940's. These two material classes are isomorphous and their characteristic material constants are well defined. These materials display a cubic lattice structure above a certain temperature (known as the Curie temperature) and tetragonal lattice structure below the Curie temperature. Because of this phenomena, these materials can be processed to have both molecular dipoles (in each molecule, the effective center of positive charge is some distance away from the effective center of negative charge, with that distance being the length of the dipole), as well as piezoelectric properties. Much of the developmental work was performed at the Bell Laboratories under the direction of Warren P. Mason. Mason records many of the details of the work in his book (Mason, 1950). This work and discoveries by Bernard Jaffe in 1954 led to the addition of oxides to ceramic compounds to achieve desired properties. Significant development occurred at the Clevite Corporation throughout the 1950s and 60s. Their developments led to the series of PZT materials commercially available today.

Research continues into creating better piezoelectric materials. Recently, a new form of piezoelectric material has been created. Called "single crystal piezoelectric materials," these

material are created by growing single crystals into full-scale materials. They are just now (year 2000) becoming commercially available, and boast a strain approaching one percent.

Today, applications of piezoelectric materials are very broad. Some of the most significant application advances have occurred in the area of structural control and sensing. This area was initially termed "smart structures" or "adaptive structures" but has since evolved into what is now called "multifunctional structures." The vast majority of the applications in this area employ contemporary polycrystalline ceramics instead of naturally occurring crystals due to their versatility and tailorability. These ceramics are hard, dense materials that can be manufactured in a wide array of shapes and sizes. The electric and mechanical principle directions can be oriented precisely with respect to the structural shape of the ceramic. They are immune to the environmental effects that were deterrents to the use of their predecessors. In short, they are superior materials that possess characteristics that allow their use to be widespread in today's technological society.

II. Solid-State Physics of Piezoelectric Ceramics

Introduction

Piezoelectric ceramics are electro-mechanical coupled materials with unique relationships describing the interaction between the systems. A simplified schematic of the interactions that exist in a piezoceramic material is shown in Fig. 1. The primary interactions addressed in current structural mechanics are denoted with solid lines. The secondary interactions are denoted with dashed lines. The secondary interactions are ignored as higher order effects in the vast majority of structural applications.

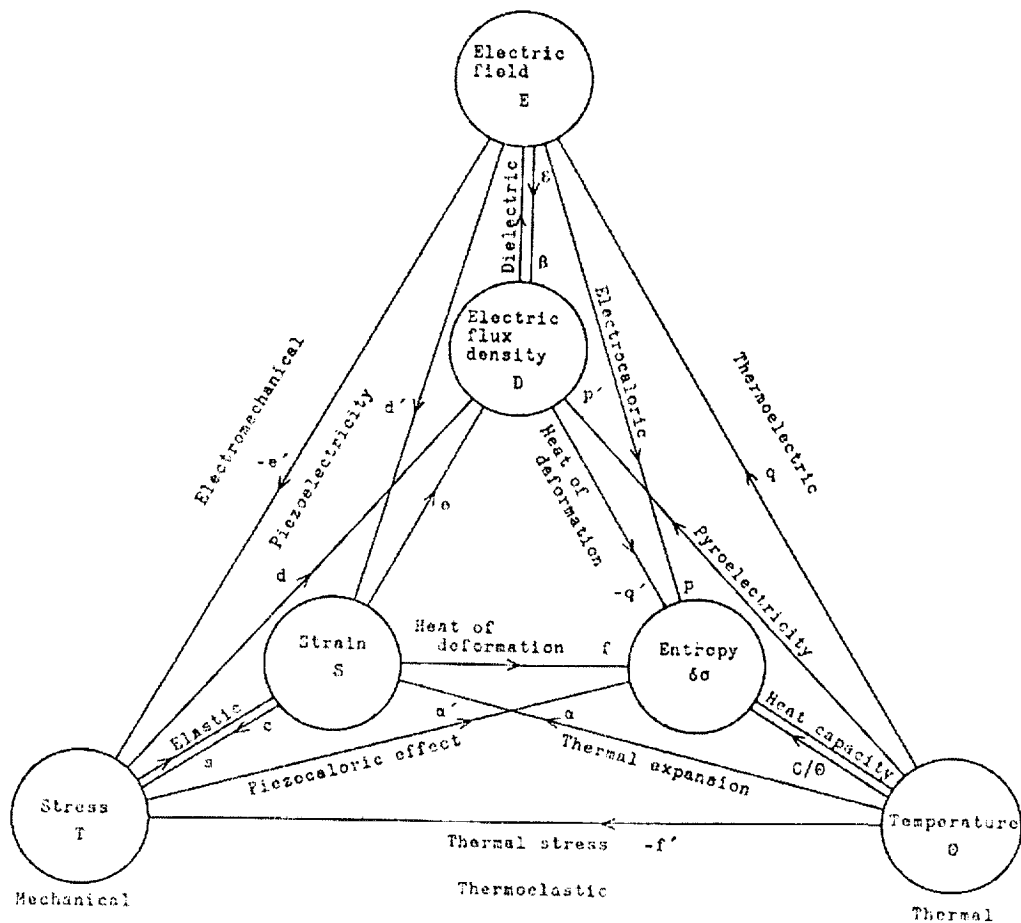


Figure 1. Phenomena Interactions in Piezoceramic Materials. (Ikeda, 1990, p. 4)

The primary focus of the remainder of this chapter is the introduction and description of the piezoceramic materials that possess interactions as shown in Fig. (1) that are currently used in structural applications. Definitions of the classifications of the family of piezoceramic materials are presented followed by a presentation of the constants and coefficients that quantify the primary interactions shown in Fig. (1). The constitutive relations, modeling

methods, application analysis methods and manufacturing / application guides are included in subsequent sections.

Piezoceramic Classifications

The most commonly used piezoceramic materials in structural control / sensing and acoustics applications are variations of lead zirconate titanate and Barium titanate. The properties of these materials vary significantly due to small alterations in the constituent materials. Over the past 50 years, a large number of piezoceramic materials have been produced by small variations and additions to the constituent materials. However, a large percentage of the currently used piezoceramics fit into specifications and standards set by various governing agencies. Because most manufacturers have selected specific names for their piezoceramic materials, the most common classification method is presented here to aid in the understanding of manufacturer data sheets and to allow comparison between the manufacturers.

The most commonly used piezoceramic materials in structural control / sensing and acoustics applications are variations of lead zirconate titanate, lead metaniobate, and Barium titanate. Currently, the most commonly used of these materials is lead zirconate titanate. The properties of all of these materials vary significantly due to small alterations in the constituent materials. Over the past 50 years, a large number of piezoceramic materials have been produced by small variations in the weight percentages of the constituent materials and by additions of other materials in small weight percentages to the base constituent materials. However, a large percentage of the currently used piezoceramics can be classified or categorized generally.

In general, lead zirconate titanate based materials are characterized by high piezo-electric and dielectric constants over large temperature ranges and stress amplitudes. "Hard" and "soft" variations of lead zirconate titanate exist. These materials are relatively tailorable and have found use in a wide array of applications. These materials are the currently the material of choice for applications as electro-mechanical and electro-acoustic transducers. Modified lead metaniobate materials are used in applications requiring high sensitivity and clean impulsive responses. In general, they possess low dielectric constants thus making them well suited for high frequency work. These materials are routinely employed in NDE applications.

Although most manufacturers have selected specific names for their piezoceramic materials, often they may be classified according to a "standard" or general classification. Many lead zirconate titanate and modified lead metaniobate materials produced by a wide variety of manufacturers are very similar in terms of performance and composition. Among the most common classifications for lead zirconate titanate materials are the "DOD Types" or "Navy Types" as defined in DOD-STD-1376. Table 1 shows a listing of materials from several common companies according to the general material type as specified by the Navy standard. A much more general description of the materials is the "Hard" and "Soft" groupings. These groupings are not standards, but are generalities based on the ceramic properties.

Hard Piezoceramics

Navy Types I and III are generally considered to be "hard" lead zirconate titanate piezoceramics. These ceramics are capable of withstanding high mechanical stress and high electrical excitation levels. These materials are well suited for application of high

Table 1. Material by Manufacturer Comparison Table.

Company	Chan- nel	EDO	Kera- mos	Morgan Matrox	Motor- ola	Poly- tech	Sensor Tech	Valpey- Fisher
Navy Type I	C- 5400	EC-64	K-270	PZT-4			BM400	VP-A40
Navy Type II	C- 5500	EC-65	K-350	PZT-5A	3195		BM500	VP-A50
Navy Type III	C- 5800	EC-69	K-278	PZT-8			BM800	VP-A80
Navy Type VI	C- 5700	EC-76		PZT-5H	3203		BM532	VP-A55
Modified Lead Meta niobate		EC-82	K-81 K-83 K-85				BM900 BM920 BM940	VP-M18, VP-M38, VP-M58

voltage, or as high power generators and transducers. These materials generally have low loss factors and high mechanical quality.

Navy Type I materials are suitable for use in sonar, ultrasonic cleaning and other high power applications. This material has low mechanical and dielectric losses, and can produce large mechanical drive amplitudes. Typical maximum operating dc fields for Navy Type I materials range from 450 to 500 volts/mm (11.4 - 12.7 kV/in).

Navy Type III materials are used in high power applications such as ultrasonic cleaning, cell disruption, phacoemulsification and other high power ultrasonics. These materials have very high mechanical quality, and are able to withstand high levels of mechanical stress and electrical excitation. Typical maximum operating dc fields for Navy Type III materials range from 450 to 500 volts/mm (11.4 - 12.7 kV/in).

Table 2. Common "hard" lead zirconate titanate piezoceramic materials.

DOD Navy Type	Common PZT Name	Material	General Applications and Characteristics
I	PZT-4	Modified PZT	Acoustic radiating, ultrasonic cleaning, sonar, high voltage generators
II	PZT-8	Modified PZT	Low loss factors, high mechanical quality, good sensitivity

Soft Piezoceramics

"Soft" lead zirconate titanate piezoceramics possess high sensitivity and permittivity. These ceramics possess piezoelectric constants that are generally higher than those of the "hard" grouping. However, these ceramics are susceptible to self-heating beyond their operating range when subject to high electrical excitation. The Curie temperature of the materials can vary significantly. The time and temperature stability of these materials are generally much lower than the hard ceramics. These materials are well suited for low-power motor type applications, receivers, and low-power generators. Navy Types II and VI are the most notable among the soft ceramics.

Navy Type II materials have high sensitivity and permittivity. The time stability and temperature dependent linearity of these materials is good. These materials are often used as the receiver or generator element in accelerometers, vibration pickups, hydrophones, medical doppler transducers, and low power structural control motors and receivers. These materials are currently the most commonly used materials in structural applications due to their strong performance over a wide range of temperatures. Typical maximum operating dc electrical field values range between 225 and 250 V/mm (5.72 and 6.36 kV/in).

Navy Type VI materials have very high permittivity, coupling and piezoelectric constants. However, their time stability and temperature dependent linearity are poor relative to other "soft" and "hard" materials. The Curie temperature for these materials is the lowest of all of the lead zirconate titanate piezoceramic materials. These materials will self-heat past their Curie temperature if used in high power applications. These materials generally exhibit large hysteresis that must be compensated in order to maintain high precision accuracy. Applications where these materials are commonly used include nano-positioning (with temperature compensation), medical diagnostics, non-destructive evaluation methods and low power structural control and sensing applications. Typical maximum operating dc

Table 3. Common "soft" lead zirconate titanate piezoceramic materials.

DOD Navy Type	CommonP ZT Name	Material	Applications and Characteristics
II	PZT-5A		Accelerometers, hydrophones, low power structural control, stable sensors; High sensitivity, permittivity, good time and temperature stability
V	PZT-5J	Modified PZT	Fuses, hydrophones, low power structural control; High permittivity, high piezoelectric constants Sensitive receivers, applications requiring fine motion control; low power structural control;
VI	PZT-5H		Very high piezoelectric constants, coupling, permittivity, low Curie temperature, lower temperature and time stability

electrical field values range between 225 and 250 V/mm (5.72 and 6.36 kV/in). In general, these materials display significantly greater deflection-field hysteresis loops than “hard” materials due to self-heating and material loss characteristics.

In general, lead zirconate titanate based materials are characterized by high piezoelectric and dielectric constants over large temperature ranges and stress amplitudes. These materials are the currently the material of choice for applications as electro-mechanical and electro-acoustic transducers. Modified Barium titanate materials are used in applications requiring lower power levels but high sensitivity.

Notation

As a convention, the orthogonal rectangular Cartesian axes 1, 2 and 3 (analogous to X, Y and Z) are assigned to the material as shown in Figure 2 below. The 3 axis, known as the polar axes, is always defined to be parallel to the direction of the polarization within the ceramic. This direction is set during the manufacturing process as a permanent polarization is induced into the material by the application of a high static DC voltage. Often, a polarization vector is shown on manufacturer data sheets. This vector points from the positive to the negative poling electrode. Standard notation sets the positive 3 axes in the direction opposite the poling vector. Care should be taken to observe the exact notation employed in manufacturer data sheets as some manufacturers set the positive direction of 3 axes in the same direction as the poling vector.

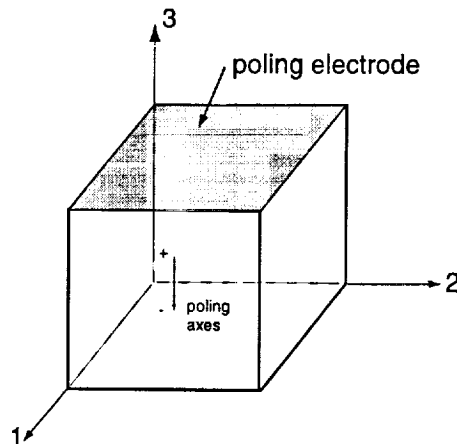


Figure 2. Designation of the material axes.

All piezoelectric properties depend on the direction within the material. Many properties also depend on both the mechanical and electrical boundary conditions. To completely identify the descriptive coefficients, super and sub-scripts are attached to each coefficient. The directionality of a coefficient is indicated by the subscripts 1, 2, 3, 4, 5 and 6 attached to the coefficient. Subscripts 1, 2 and 3 indicate the principal axes; 4, 5 and 6 denote shear around the 1, 2 and 3 axes respectively. Because polar symmetry exists, the 1 and 2 axes are identical (differing only by a right angle). For simplicity, reference is made only to the 3 and 1 directions and it is understood that 1 also implies 2. Occasionally the subscripts “p” and “h” are used to denote specific conditions. “p” signifies that the stress (or strain) is equal in all directions perpendicular to the 3 axis and that the electrodes are on the faces perpendicular to the 3 axes. “h” indicates the electrodes are again on the faces perpendicular to the 3 axes (for ceramics) and that the stress is hydrostatic in nature (equal magnitude in the 1, 2 and 3 directions). The boundary conditions, when applicable, are

indicated by a superscript attached to the coefficient. The boundary condition superscripts used are T, S, D and E signifying:

T = constant stress (mechanically free)

S = constant strain (mechanically constrained)

D = constant electrical displacement (open circuit)

E = constant field (short circuit).

In general, the superscripts describe external factors that affect the property while subscripts describe the relationship of the property to the principal axes of the material. Because piezoelectric materials are electro-mechanical coupled materials, the descriptive symbols differ slightly from those traditionally used in linear elastic mechanics. Typical symbols are shown in Table 4. The symbols and their definitions are given in Appendix A. A description of the primary symbols follows in this section.

Most piezoelectric constants have double subscripts. These subscripts denote coupled

Table 4. Typical Symbols Used in Describing Piezoceramic Properties.

<p>s^E_{33} — Indicates that the property is measured with the electrode circuit closed</p> <p>— Indicates that the <u>stress</u> or strain is in the 3 direction</p> <p>— Indicates that the stress or <u>strain</u> is in the 3 direction</p> <p>— Compliance = strain / stress</p> <p>Note: all stresses, other than the stress indicated in one subscript, are held constant.</p>	<p>s^D_{36} — Indicates that the property is measured with the electrode circuit open</p> <p>— Indicates that the <u>stress</u> or strain is shear around the 3 direction</p> <p>— Indicates that the stress or <u>strain</u> is in the 3 direction</p> <p>— Compliance = strain / stress</p> <p>Note: all stresses, other than the stress indicated in one subscript, are held constant.</p>
<p>k^T_3 — Indicates that the stresses on the material are constant (example: no applied forces)</p> <p>— Indicates that the electrodes are perpendicular to the 3 axes</p> <p>— Relative Dielectric Constant</p>	<p>k^S_1 — Indicates that all strains in the material are constant (example: completely blocked boundaries)</p> <p>— Indicates that the electrodes are perpendicular to the 1 direction</p> <p>— Relative Dielectric Constant</p>
<p>k_{31} — Indicates that the electrodes are perpendicular to the 3 axes</p> <p>— Indicates that the stress or strain is in the 1 direction</p> <p>— Electromechanical Coupling</p>	<p>k_p — Indicates that the electrodes are perpendicular to the 3 axes and the stress or strain is equal in all directions perpendicular to the 3 axes</p> <p>— Electromechanical Coupling</p>
<p>g_{31} — Indicates that the electrodes are perpendicular to the 3 axes</p> <p>— Indicates that the stress or strain is in the 1 direction</p> <p>— $\frac{\text{field}}{\text{applied stress}} = \frac{\text{strain}}{\text{applied charge/electrode area}}$</p>	<p>g_h — Indicates that the electrodes are perpendicular to the 3 axes (ceramics only) and the stress is equal in all directions (hydrostatic stress)</p> <p>— $\frac{\text{field}}{\text{applied stress}} = \frac{\text{strain}}{\text{applied charge/electrode area}}$</p>
<p>d_{31} — Indicates that the electrodes are perpendicular to the 3 axes</p> <p>— Indicates that the stress or strain is in the 1 direction</p> <p>— $\frac{\text{strain}}{\text{applied field}} = \frac{\text{short circuit charge/electrode A}}{\text{applied stress}}$</p>	<p>d_{33} — Indicates that the electrodes are perpendicular to the 3 axes</p> <p>— Indicates that the stress or strain is in the 3 direction</p> <p>— $\frac{\text{strain}}{\text{applied field}} = \frac{\text{short circuit charge/electrode A}}{\text{applied stress}}$</p>

electrical and mechanical interactions. The first subscript gives the direction of the electrical field associated with the applied voltage or charge produced. The second subscript gives the direction of the mechanical stress or strain. Examples of constants used to describe a piezoceramic material are given in Table 4.

Polarization and the Resulting Piezoelectric Actions

The most widely used piezoelectric materials are polycrystalline ceramics based on variations of the three primary classes of piezoelectric ceramics: lead zirconate titanate, lead metaniobate and barium titanate. In their original state, these ceramics are isotropic and possess no piezoelectric properties. Like piezoelectric materials, their crystals do not possess a center of symmetry. However, the crystals are randomly oriented thus rendering the material isotropic and essentially void of piezoelectric characteristics. Through the application of a high static electric field while the ceramic is at an elevated temperature, the crystals are oriented and the material becomes anisotropic. More importantly, the ceramic retains a remnant of the polarization after the field is removed which induces piezoelectric properties. The original dimensions of the ceramic change due to the polarization as depicted in Figure 3. Most manufacturers mark the direction of the poling axes with a small dot or electrode on the surface held at the high voltage during the poling process.

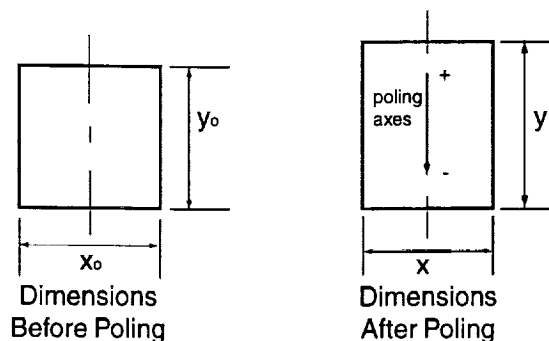


Figure 3. Effects of poling on the material dimensions.

The response of a poled piezoceramic to an applied field lower than the poling field is a change in the dimensions. A voltage with the same polarity as the poling voltage causes the piezoceramic to expand in the 3 direction and contract in the 1 direction. Conversely, a voltage with polarity opposite the poling voltage (depoling direction) causes a contraction in the 3 direction and an expansion in the 1 direction. These responses are shown in Figure 4. It should be noted that some manufacturer data sheets have this notation backwards.

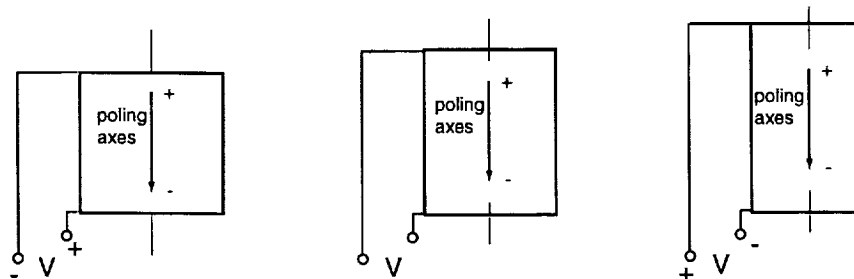
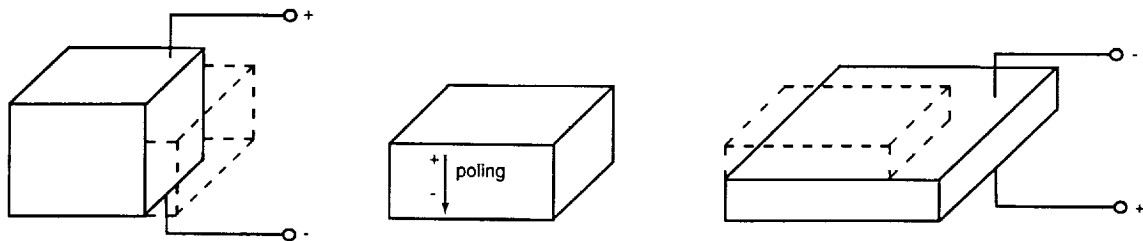


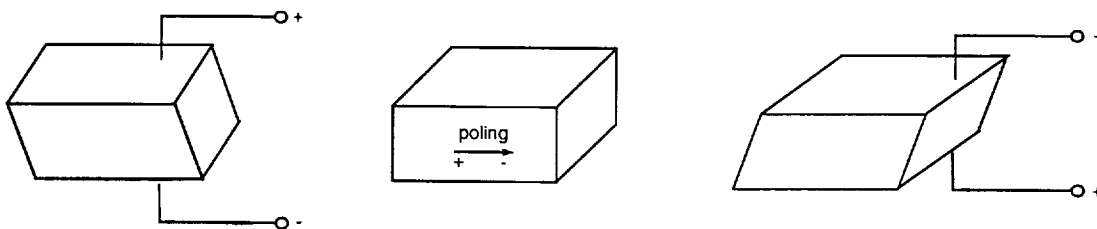
Figure 4. Response of a Poled Ceramic to an Applied Electrical Field.

Limitations exist on the magnitudes of the allowable applied voltages. Exceeding the threshold voltage fields results in degradation or complete elimination of the dielectric and piezoelectric properties of the material. In particular, a large voltage applied in the “depoling direction” (the direction opposite the poling direction) may result in degradation or elimination of the original poling. The electric dipoles may be partially flipped resulting in material property degradation, or completely flipped 180° thereby resulting in the material being repoled in the opposite direction. The maximum depoling field a piezoceramic can withstand without sustaining permanent degradation is called the “coercive field.” The magnitude of the coercive field is a function of the material constituents and the processing.

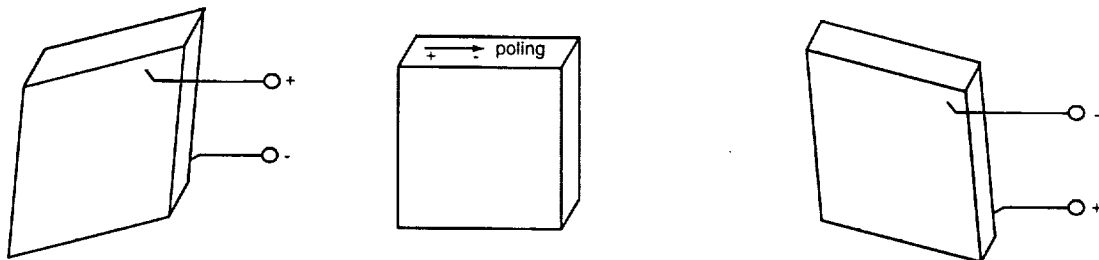
All applied electrical fields cause deformations in a piezoceramic. However, the total deformation is a function of the shape, orientation of the 3 direction within the shape, and the placement of the electrical leads. Operation of the piezoceramic in this manner is known as the “motor” or converse effect. This is the mode of operation of motors and other motion producing active elements. The three primary deformations as shown in Figure 5 are 1: thickness and in-plane expansion / contraction; 2: thickness shear; and 3: face shear. Although the modes are shown as distinct modes in Figure 5, piezoceramic motors will exhibit a combination of modes.



In-plane and thickness expansion / contraction modes



Thickness shear modes



Face shear modes

Figure 5. Deformation modes of piezoceramics.

Additionally, all applied forces and deformations result in a charge appearing on the electrodes of the ceramic. If the electrodes are not short-circuited, a voltage is developed between the surfaces. Operation of a piezoceramic in this fashion manifests the direct or

"generator" effect. This is the mode of operation of sensors. The magnitudes of the resulting charge and the related voltage are a function of the direction of the applied force or strain, the structural shape, orientation of the 3 direction within the shape, and the placement of the electrical leads. Figure 6 depicts the most common applied forces and the resulting piezoceramic voltages assuming the electrodes are not short-circuited.

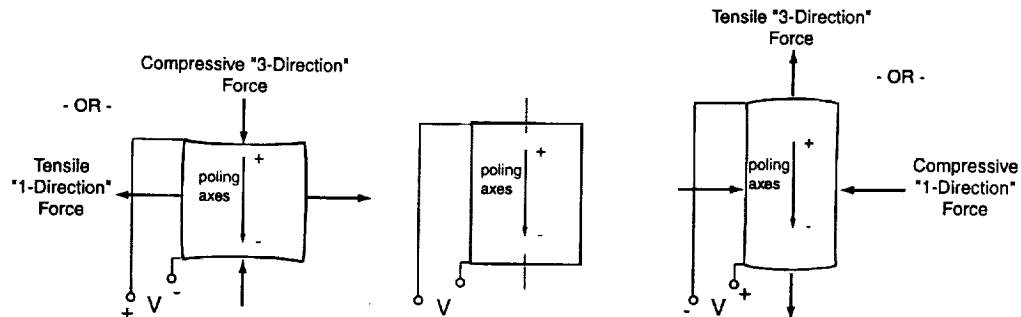


Figure 6. Piezoelectric Voltages Due to Applied Forces.

If an alternating field is applied to the piezoceramic, the piezoceramic will vibrate at the frequency of the applied field. Like all mechanical systems, a piezoceramic element has fundamental frequencies normally called the resonance frequencies. Typically, the first resonance frequency is the most significant and is called the fundamental resonance frequency. When the piezoceramic is driven at a frequency equal to the fundamental frequency, the resulting vibration amplitudes are significantly greater than those achieved by a DC field with the same absolute magnitude. The fundamental frequency occurs when the thickness of the piezoceramic element is equal to one-half a wavelength. Correspondingly, large amplitude motion will be realized when ever the thickness of the piezoceramic is equal to an odd number multiple of half a wavelength. The frequencies at which this large motion occurs are called overtone resonance frequencies (3rd overtone, 5th overtone, ect).

Piezoelectric Material Descriptive Coefficients and Properties

The properties of piezoceramic materials are generally classified according to their basic type. Being a solid, piezoceramics possess physical properties very similar to the common elastic solid materials commonly known. Being a dielectric, piezoceramics possess the properties unique to dielectrics. Finally, because of the dielectric properties, the piezoceramic possesses piezoelectric properties unique to this class of materials. The primary properties in each of these groups are presented in this section.

Physical Properties

Density Δ

The density of piezoceramics is defined as the ratio of mass to the material volume in the poled state. Typical units on the density are kg/m^3 or g/cm^3 .

Young's Modulus Y

All solid materials are characterized by the stiffness ratio of stress to strain commonly known as Young's modulus. Because of the electro-mechanical coupling, the value of Young's modulus is dependent upon the electrical boundary conditions. Mechanically stressing a piezoceramic produces an electrical response that opposes the resulting strain.

Therefore, the modulus when the electrodes are open is higher than the modulus when the electrodes are closed (shorted). Because the material is at best transversely isotropic, the modulus is also dependent on the direction in the material. Examples of Young's Modulus Y are shown in Figure 7 for clarity.

<p>Y^E — Indicates that the property is measured with the electrode circuit closed</p> <p>33 — Indicates that the <u>stress</u> is in the 3 direction — Indicates that the <u>strain</u> is in the 3 direction</p> <p>— Young's Modulus = stress / strain</p> <p>Note: all applied stresses, other than the stress indicated in the first subscript, are zero.</p>	<p>Y^D — Indicates that the property is measured with the electrode circuit open</p> <p>55 — Indicates that the <u>stress</u> is shear around the 2 axes — Indicates that the <u>strain</u> is shear around the 2 axes</p> <p>— Young's Modulus = stress / strain</p> <p>Note: all applied stresses, other than the stress indicated in the first subscript, are zero.</p>
--	--

Figure 7. Young's Modulus for Piezoceramic Materials

Curie Temperature

The Curie temperature is defined as the critical temperature at which the material's dielectric constant peaks and all polarization is lost resulting in a complete loss of all piezoelectric properties. This results as the crystals have greater mobility to move into a random pattern as the temperature rises. After cooling below the Curie temperature, the material will not regain its piezoelectric properties. In general, piezoelectric materials should be operated well below their Curie temperature.

Maximum Operating Temperature

The maximum operating temperature is the temperature at which degradation of the piezoelectric properties begins. It is always lower than the Curie temperature, and depends on the material composition. Some manufacturers list the maximum operating temperature on manufacture data sheets. Often, the recommended maximum operating temperature is one-half of the Curie temperature. It should be noted that some piezoceramics, particularly the "soft" ceramics are susceptible to self-heating under dynamic load. High frequency operation of these ceramics at ambient temperatures near the maximum operating temperature may result in the material's actual temperature exceeding the maximum operating temperature. "Hard" piezoceramics should be used in applications that involve high power dynamic cyclic loading of the piezoceramic to avoid the self-heating problem. Hard piezoceramics are commonly used in ultrasonic cleaners and other very high frequency devices.

Equivalent Circuit and the Mechanical Q

Because piezoceramics are coupled electro-mechanical systems, an electrical circuit can be used to describe their behavior when subject to certain drive conditions. Near resonance, the piezoceramic can be represented with the circuit shown in Figure 8. The four parameters are the series capacitance C_1 , resistance R_1 , inductance L_1 , and the shunt capacitance C_0 . The circuit representation is good only if the parameters are independent of frequency which occurs only if the piezoceramic resonator has no other vibration modes near the resonance of interest. The resistance R_1 in the equivalent circuit represents the mechanical losses of the piezoceramic resonator. At very low frequencies with respect to the

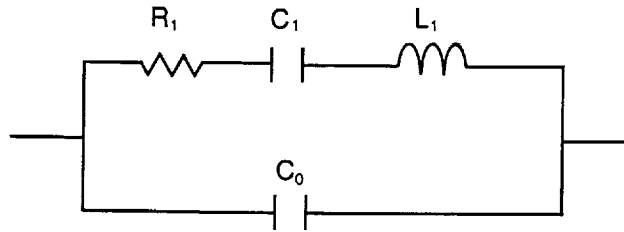


Figure 8. Equivalent electrical circuit representing piezoelectric materials

The ratio of the reactance (the imaginary part of the impedance) to the resistance (real part of the impedance) in the circuit is defined as the Mechanical Q. It should be noted that the shape of the piezoceramic affects the value of Q.

Dielectric Properties

The Relative Dielectric Constant K and Dielectric Loss "tan δ"

The relative dielectric constant is a dimensionless quantity that is analogous to the dielectric constant of a capacitor: it is a measure of the electrical charge that the material retains compared to the charge that would be stored by electrodes of the same area but separated by a vacuum. Equation 1 gives the constant K as:

$$K_{ij} = \frac{\epsilon_{ij}}{\epsilon_0} \quad (1)$$

where the constant ϵ_0 is the permittivity of free space and has a value of 8.85×10^{-12} farads/meter, and ϵ_{ij} is the permittivity of the material in the desired mode.

The dielectric constant is dependent on the material direction and therefore carries a single subscript denoting the directional dependence. The subscript "1" indicates the constant is perpendicular to the polar axes while "3" indicates the constant is parallel to the axes. The magnitude of the dielectric constant depends on the boundary conditions applied to the material. If the material is free to expand and contract, the dielectric constant is higher than the constant associated with fully constrained boundaries. Therefore two dielectric constants related through the electromechanical coupling factor k as shown in Equation 2 below are used to characterize the material,

$$\begin{aligned} K_1^s &= K_1^T (1 - k_{15}^2) \\ K_3^s &= K_3^T (1 - k_{33}^2) \end{aligned} \quad (2)$$

Figure 9 explains the notation for the dielectric coefficients.

Due to the magnitude of the electromechanical coupling coefficient k , the ratio between

<p>K^T₃ — Indicates that the stresses on the material are constant (example: no applied forces)</p> <p>— Indicates that the electrodes are perpendicular to the 3 axes</p> <p>— Relative Dielectric Constant</p>	<p>K^S₁ — Indicates that all strains in the material are constant (example: completely blocked boundaries)</p> <p>— Indicates that the electrodes are perpendicular to the 1 direction</p> <p>— Relative Dielectric Constant</p>
--	--

Figure 9. Notation for relative dielectric constant.

the free and clamped dielectric constants may be as high as 2:1. Piezoceramic materials usually possess dielectric constants in the range of several hundred to several thousand, and are subject to change under high voltage fields.

When subject to harmonic sinusoidal voltages, the charge stored in a piezoceramic is complex possessing both real and an imaginary parts due to dielectric absorption and resistive leakage. Defining the complex dielectric constant as $\epsilon^* = \epsilon' - j\epsilon''$ leads to the "dielectric loss" which is: $\tan \delta = \epsilon'' / \epsilon'$.

Capacitance C

At frequencies well below the resonant frequency, a piezoceramic element is fundamentally a capacitor. The capacitance of the element is generally not considered to be a material dielectric property like the relative dielectric constant K because the capacitance is dependent on the material dimensions and the dielectric constant K. The capacitance of a piezoceramic element can be calculated using Equation 3.

$$C = \frac{K \epsilon_0 A}{t} \quad (3)$$

where A is the area of the electroded surface and t is the thickness between the electrodes. Note that due to the directionality of the dielectric constant K, the capacitance is dependent on the direction also. At resonance, the dielectric constant K is reduced by the factor $(1 - k^2)$ where k is the coupling factor of the particular mode.

The charge developed on a piezoceramic element is related to the capacitance precisely defined in a capacitor: $Q = C V$ where Q is the charge, C is the capacitance and V is the voltage.

Piezoelectric Properties

Coupling Coefficient k^2

The electromechanical coupling coefficient is arguably the most important of all of the properties. It is the best single measurement of the strength of a piezoelectric effect. It describes the conversion of energy by the ceramic element from mechanical to electrical form (or from electrical to mechanical form). In essence, it measures the fraction of the electrical energy from an applied field that is converted to mechanical energy (or vice versa when the piezoceramic is stressed) as shown in Figure 10.

k_{31} <ul style="list-style-type: none"> Indicates that the electrodes are perpendicular to the 3 axes Indicates that the stress or strain is in the 1 direction <p>Electromechanical Coupling</p>	k_p <ul style="list-style-type: none"> Indicates that the electrodes are perpendicular to the 3 axes and the stress or strain is equal in all directions perpendicular to the 3 axes <p>Electromechanical Coupling</p>
k_r <ul style="list-style-type: none"> Indicates that ceramic is disk shaped, the electrodes are perpendicular to the 3 axes and the stress or strain is radial <p>Electromechanical Coupling</p>	$k^2 = \frac{\text{electrical energy converted to mechanical energy}}{\text{input electrical energy}}$ $k^2 = \frac{\text{mechanical energy converted to electrical energy}}{\text{input mechanical energy}}$

Figure 10. Piezoceramic coupling coefficients

Because the conversion from one energy form to another is always incomplete, k^2 is always less than unity. Typical values of the electro-mechanical coupling coefficient k^2 range from 0.40 to 0.70 for most piezoceramics. Values as high as 0.90 have been measured for Rochelle salt at its Curie temperature. The magnitude of the coupling factors depends upon the degree of poling that exists in the material. The most common coupling factors are derived from the constitutive equations and have the form as shown in equation 4 below.

$$\begin{aligned} k_{33} &= \frac{d_{33}}{\sqrt{s_{33}^E \epsilon_3^T}} & k_{31} &= \frac{d_{31}}{\sqrt{s_{11}^E \epsilon_3^T}} \\ k_{15} &= \frac{d_{15}}{\sqrt{s_{44}^E \epsilon_1^T}} & k_p &= \frac{d_{31}}{\sqrt{2 / (s_{11}^E + s_{11}^E) \epsilon_3^T}} \end{aligned} \quad (4)$$

While the coupling factor does quantify the fraction of energy converted from one form to another, it is not to be confused with conversion efficiency. In the quasi-static energy conversion form, if there are no dissipation in the system, the net efficiency is 100%. This is a result of recoverable energy being stored in the material and returned to the source upon completion of the cycle. Therefore, the coupling coefficient k^2 can be thought of as a measure of the ineffective energy or unavailable energy.

Further understanding of this term can be gained by considering a single piezoceramic element under applied pressure. Part of the energy from the applied pressure is converted into an electrical charge that appears on the electrodes (analogous to a charged capacitor), and the remaining energy is stored in the element as mechanical energy (analogous to a compressed spring). When the pressure is removed, the element will return to its original dimensions and the charge will disappear from the electrode surfaces.

The coupling coefficient is physically related to the piezoceramic's resonance and anti-resonance frequencies. Although analytical methods for predicting the electro-mechanical coupling exist, standard test methods are easily applied for measuring the coupling coefficient and are therefore often the determination method chosen. Because of the directionality of the material, subscripts denote the directionality of the coupling coefficient and the type of motion involved. Examples of the common electro-mechanical coefficients are given above for clarity.

The coupling coefficient is a characteristic index for the performance of a transducer. It indicates the utility of the material in the transducer in the sense of quantifying how much energy remains in the material rather than being converted to another form. A high k^2 value indicates a measure of the magnitude of the transducer bandwidth and is a performance measure of the transducer.

The electro-mechanical coupling coefficient is related to the elastic constants: stiffness c and compliance s . The relationships between the stiffness constants are given in equations 5.

$$\begin{aligned} s_{11}^D &= s_{11}^E (1 - k_{31}^2) & s_{33}^D &= s_{33}^E (1 - k_{33}^2) \\ s_{11}^D &= s_{12}^E - k_{31}^2 s_{11}^E & s_{44}^D &= s_{44}^E (1 - k_{15}^2) \end{aligned} \quad (5)$$

Insight into the physical meaning of the electro-mechanical is realized through the following simple example. Consider a piezoceramic that has a k_{31} value of 0.35. If 1 erg of electrical energy is applied to the 3 axis of the ceramic, the mechanical energy stored in the resulting deformation along the 1 axis is: $1 \text{ erg} \times (0.35)^2 = 0.1225 \text{ erg}$.

Piezoelectric Coefficient “d” Constant

The piezoelectric “d” constants or “strain” constants relate the mechanical strain produced by an applied electric field. When used in this manner, the action is often referred to as a “motor”, and the effect is called the “motor effect.” The direct relationship may also be defined for the constant relating the short circuit charge density to the applied mechanical stress. This is the well-known piezoelectric effect and is occasionally called the “generator” action. The d constants are properties of the material and are not affected by the boundary conditions. The most common forms of the d constant and the appropriate units are shown below.

d_{31} — Indicates that the electrodes are perpendicular to the 3 axes — Indicates that the piezoelectrically induced strain or the applied stress is in the 1 direction	d_{33} — Indicates that the electrodes are perpendicular to the 3 axes — Indicates that the piezoelectrically induced strain or the applied stress is in the 3 direction
d_{15} — Indicates that the electrodes are perpendicular to the 1 axes — Indicates that the piezoelectrically induced strain or the applied stress is shear around the 2 axes	$d = \frac{\text{strain}}{\text{applied field}} = \frac{\text{short circuit charge/electrode area}}{\text{applied stress}}$ Typical units: $\frac{\text{m/m}}{\text{V/m}}$ - OR - $\frac{\text{coulombs / m}^2}{\text{Newton / m}^2}$

Figure 11. Notation for piezoelectric electric field-strain coefficients

The d constant directly relates the magnitude of the strain and thus the displacement generated by an applied field. Materials with large d constants are typically sought after for use as motion transducers.

The d constant is used directly to calculate the change in dimensions of a piezoceramic element. Consider an element that has dimensions of length L, width W, and thickness t. The free change in the dimensions are calculated as:

$$\Delta W = \frac{d_{31} W V}{t}, \Delta L = \frac{d_{31} L V}{t}, \text{ and } \Delta t = d_{33} V. \quad (6)$$

Piezoelectric Coefficient “g” Constant

g_{31} — Indicates that the electrodes are perpendicular to the 3 axes — Indicates that the applied stress or piezoelectrically induced strain is in the 1 direction	g_{33} — Indicates that the electrodes are perpendicular to the 3 axes — Indicates that the applied stress or piezoelectrically induced strain is in the 3 direction
g_{15} — Indicates that the electrodes are perpendicular to the 1 axes — Indicates that the applied stress or piezoelectrically induced strain is shear around the 2 axes	$g = \frac{\text{strain developed}}{\text{applied charge density}} = \frac{\text{open circuit electric field}}{\text{applied stress}}$ Typical units: $\frac{\text{m/m}}{\text{coulombs / m}^2}$ - OR - $\frac{\text{V/m}}{\text{Newton / m}^2}$

Figure 12. Notation for piezoelectric electric field-stress coefficients

The “g” constants or “voltage” constants relate the electric field produced by a mechanical stress. The converse relationship may also be defined for the constant relating the strain developed to the applied charge density. Like the d constants, these constants are

not affected by the boundary conditions. The most common forms of the g constant and the appropriate units are shown below.

Relationships Between the “d” and “g” Constants

The “d” and “g” constants are related through the dielectric constant. If any two of the “d”, “g” and dielectric constants are known for a particular mode, the third is uniquely determined. Equations 7 show the relations between the constants.

$$d_{33} = K_3 \epsilon_o g_{33} \quad d_{31} = K_3 \epsilon_o g_{31} \quad d_{15} = K_3 \epsilon_o g_{15}. \quad (7)$$

Thermal Considerations

Thermal Coefficient of Expansion

All solid materials are characterized by a coefficient of thermal expansion (CTE). This dimensionless quantity relating the material strain due to a temperature change is a material property and is not affected by the boundary conditions. The magnitude of the CTE varies with the material.

Pyroelectric Effects

All piezoelectric ceramics exhibit pyroelectric effects when exposed to temperature changes. This effect is the development of an electric field on the electrodes of the ceramic when exposed to a thermal change. The magnitude of the field depends on the material properties, the magnitude of the temperature change and the relative dielectric constant for the material. It should be noted that a temperature drops results in a depoling field in the piezoceramic. This can occur in the cool-down period after a piezoceramic is used in a dynamic application. Under some conditions, a large temperature drop over a short period of time may be sufficient to create a depoling field that exceeds the coercive field of the piezoceramic. To avoid the occurrence of such a field, the leads to the piezoceramic should be short-circuited during the cool down time, or the length of time over which the cool down occurs should be long enough to ensure that the charge is able to “leak” away

Material and Piezoelectric Properties as Functions of Temperature

Piezoelectric and material properties of most piezoceramic materials are temperature dependant. The degree of temperature dependence varies among the materials. Also, material properties such as d_{31} exhibit different temperature dependence.

III. Circuit Model of Piezoceramics

Introduction

The proper interface circuit model of a piezoelectric material for shunt circuit (electrical absorber) is developed and analyzed theoretically and experimentally. The emphasis is placed on the physical connection between a capacitor and a voltage source with a resistor. The first model considered is that the capacitor is connected in series with a voltage source and a resistor. The second model consists of a capacitor connected in parallel with a voltage source and a resistor. This paper presents the analyses of these two different circuit models for a piezoceramic by discussing the electric impedance, resistance, and phase angle of a piezoceramic and determines the accurate model to use for shunt applications.

Many researchers have developed the equivalent impedance and electrical circuit model of piezoelectricity based on electrical representation of the coupled electrical and mechanical problems. One of the traditional circuit models used for a piezoelectric resonator is Van Dyke's circuit model (IEEE, 1990) as shown in Figure 13. In this circuit diagram, the components L , C , R are mass, elastic compliance and mechanical damping transformed into electrical magnitude by the reverse piezoelectric effect. C_0 is the capacitance in the absence of mechanical deformation at the resonance frequency. However, the main drawback of this equivalent circuit only represents the behavior of a piezoelectric crystal in the resonant frequency. This model does not present the impedance of the piezoelectric resonator away from the center of the fundamental resonant peak.

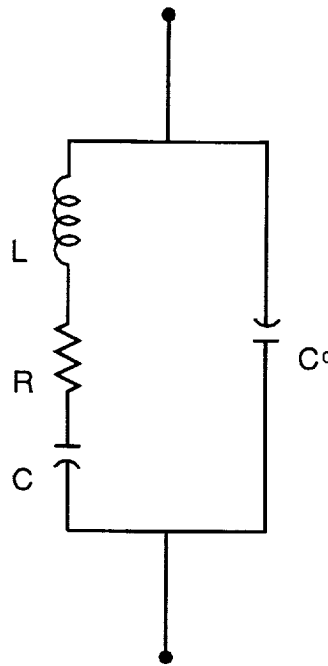


Figure 13. Equivalent circuit model of a piezoelectric resonator.

The development of an electrical impedance and interface circuit design over broad frequency ranges is essential in structural control, especially shunt circuit applications [2]. If a piezoelectric material is attached to a structure, it is strained as the structure deforms and converts a portion of the mechanical energy into electrical energy. This electrical energy is dissipated as Joule heating through the shunt components. The first step in an interface circuit design is to understand the piezoceramic characteristics as part of an electrical equivalent circuit.

Figure 14 shows two simplified equivalent circuits of a piezoceramic. One consists of a series capacitor with a voltage source and a resistor. The other consists of a parallel capacitor with a voltage source and a resistor. The capacitance, C , represents piezoceramic capacitance, which is proportional to the ceramic's permittivity and area and inversely proportional to the piezoceramic thickness. The AC voltage source amplitude is equal to the open circuit voltage of piezoelectric material and varies from micro-volts to hundreds volts, depending on the excitation magnitude. These two circuit models are discussed as in terms of the resistance of PZT as an internal resistance, which is frequency-dependent.

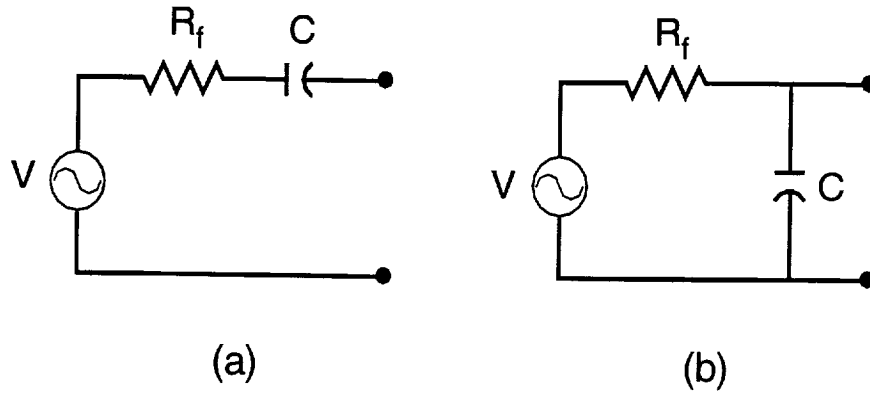


Figure 14. Two equivalent circuit model of a piezoelectric material.

Electrical impedance of a piezoceramic

In linear piezoelectricity, the constitutive relationship of a piezoelectric material can be written in the form (IEEE, 1990):

$$S_1 = s_{11}^E T_1 + d_{31} E_3, \quad (8)$$

$$D_3 = d_{31} T_1 + \epsilon_{33}^T E_3 \quad (9)$$

where the S_1 and T_1 represent the strain (*dimensionless*) and stress (N/m^2) in direction 1 (see Figure 15). D_3 ($Coulomb/m^2$) and E_3 ($Volt/m$) represent the electric displacement and the electric field intensity in direction 3, respectively. Furthermore, s_{11}^E (m^2/N) and ϵ_{33}^T ($Farad/m$) the compliance in direction 1 at constant electric field intensity (i.e., $E=0$) and free (i.e., $T=0$) dielectric permittivity, respectively. Furthermore, d_{31} ($m/Volt$) is called the piezoelectric strain constant measured in 1 direction, due to an electric field applied in direction 3.

The equation of motion for a PZT vibrating in the x (1)-direction can be expressed as

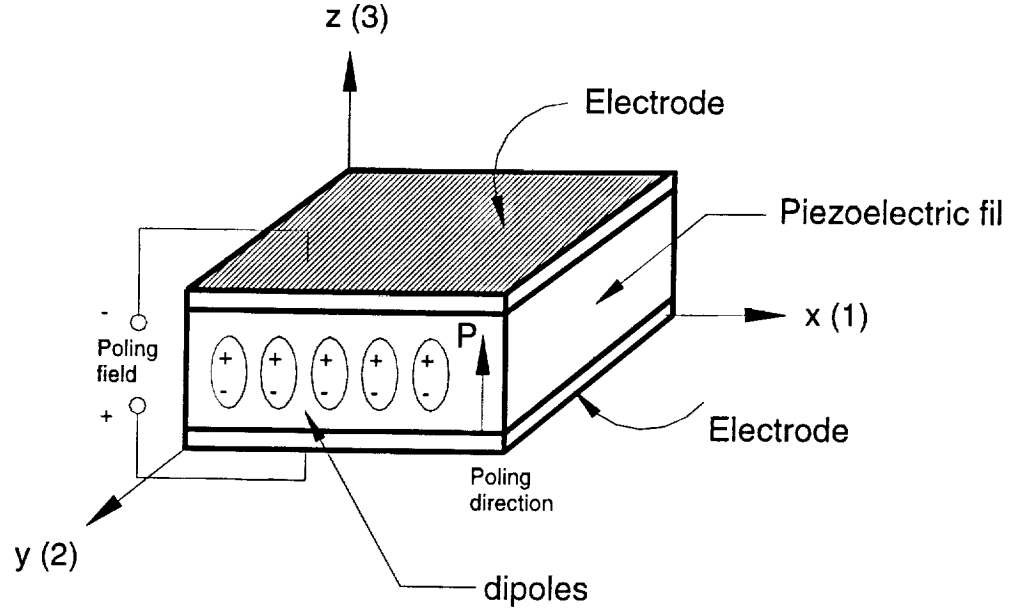


Figure 15. Piezoelectric element and notations.

follows:

$$\rho \frac{\partial^2 u}{\partial t^2} = \frac{1}{s_{11}^E} \frac{\partial^2 u}{\partial x^2} \quad (10)$$

where ρ (kg/m^3) is the mass density and u is the displacement in the x -direction (see Figure 16). Solving Equation (10) by separating the displacement u into time and spatial domain solution yields:

$$u = Ue^{i\omega x} = (A \sin kx + B \cos ky) e^{i\omega x}, \quad (11)$$

where

$$k = \sqrt{\omega^2 \rho s_{11}^E} \quad (12)$$

For a stress free actuator at $x = \pm L/2$, then Equation (9) gives:

$$S_1 = \partial u / \partial x = d_{31} E_0 e^{i\omega x} \quad (13)$$

where we have defined $E = E_0 e^{i\omega x}$. The coefficient, A , in Equation (11) can be determined from Equation (13):

$$A = \frac{d_{31} E_0}{k \cos(kL/2)} \quad (14)$$

Hence, the longitudinal strain is given by:

$$\frac{\partial u}{\partial x} = \frac{d_{31} E_0}{k \cos(kL/2)} \cos(kx) e^{i\omega x} \quad (15)$$

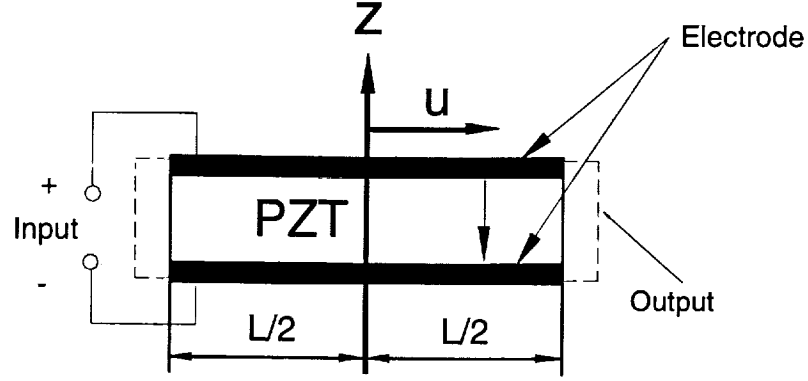


Figure 16. Electrical and mechanical interaction of PZT.

The electrical impedance, Z_e , of piezoceramic can be expressed as follows:

$$Z_e = \frac{V}{I} \quad (16)$$

where V and I are the voltage and current:

$$V = \int_0^T E_3 dz, \quad I = i\omega \int_A D dx dy \quad (17)$$

Substituting Equation (15) into Equation (9), D_3 is easily obtained,

$$D_3 = \left[K_{31}^2 \frac{\cos(kx)}{\cos(kL/2)} + (1 - K_{31}^2) \right] \epsilon_{33}^T E_3 \quad (18)$$

Substituting Equation (18) into Equation (16), the electrical impedance of PZT is then found to be

$$Z_e = \frac{t E_0 e^{i\omega x}}{i\omega b L \left(2K_{31}^2 \frac{\tan(kL/2)}{kL} + (1 - K_{31}^2) \right) \epsilon_{33}^T E_0 e^{i\omega t}} \quad (19)$$

This forms the impedance model of a piezoceramic material which is verified in the following section.

Experimental verification of electric impedance of PZT

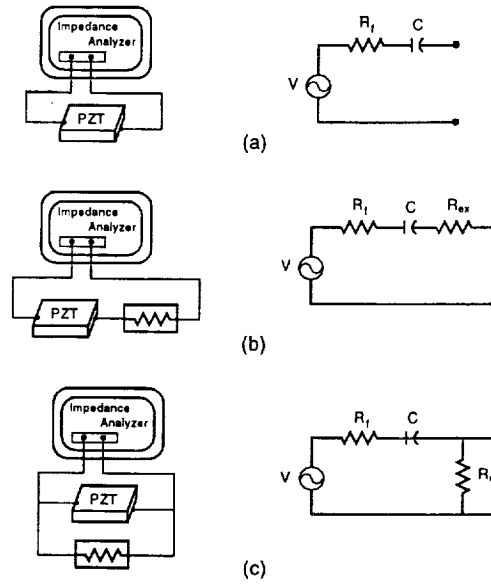


Figure 17. Three different connections with an impedance analyzer: (a) PZT only, (b) PZT connected in series with an extra resistor, and (c) PZT connected in parallel with an extra resistor

Experiments have been conducted to verify the electric impedance method of PZT presented in the previous section. Figure 17 shows an experimental apparatus, a HP 4192A Impedance/Gain-Phase Analyzer is connected to the material PZT 5H to measure the electric impedance. The impedance analyzer sends an input sweep signal to PZT and measures the feedback current through the frequency range (5-10k Hz). The PZT has a width $b=34$ mm, length $L=72.4$ mm, and thickness $t=0.267$ mm. The basic material properties for the PZT material are listed in Table 5.

Figure 18 illustrates the measured and predicted impedance of PZT. The theoretical prediction (dashed line) agrees well with the experimental data (solid line). In the view of result, it is clear that the impedance of a capacitor dominates the electric impedance of PZT.

Table 5. Main piezo-electric parameters of the PZT 5H

d_{31} (m/V)	Young Modulus	K_{31}	ρ (Kg/m ³)	ϵ_{33}^T (Farad/m)	g_{31} (Vm/N)
-320×10^{-12}	6.2×10^{10}	0.44	7800	3.363×10^{-8}	-9.5×10^{-3}

Experimental verification of two different circuit models

The series and the parallel connection between a capacitor and a voltage source with an internal resistor [Figure 14] are tested in order to determine the most appropriate model of PZT. An impedance analyzer was used to perform this test for measuring the resistance values of three different sizes of PZT materials. Three samples of different widths (small, middle and large) $b=12, 34,$ and 72.4 mm and lengths $L=24, 72.4,$ and 72.4 mm, and the same thickness $t=0.267$ mm, respectively were studied. Figure 7 shows resistance values for three different sizes of PZTs. It is noticed that the resistance values are decreased with increasing the frequency. At low frequency, the resistance can be regarded as an open-circuit due to high impedance (M Ω). However, it is not clear if the resistance in the high frequency ranges can be treated as a short circuit. To answer this problem, we measured the resistance of the wire connecting the impedance analyzers and PZTs. The measured resistance is about 3 ohm, and the resistance of a large size at 100k Hz measured about 10

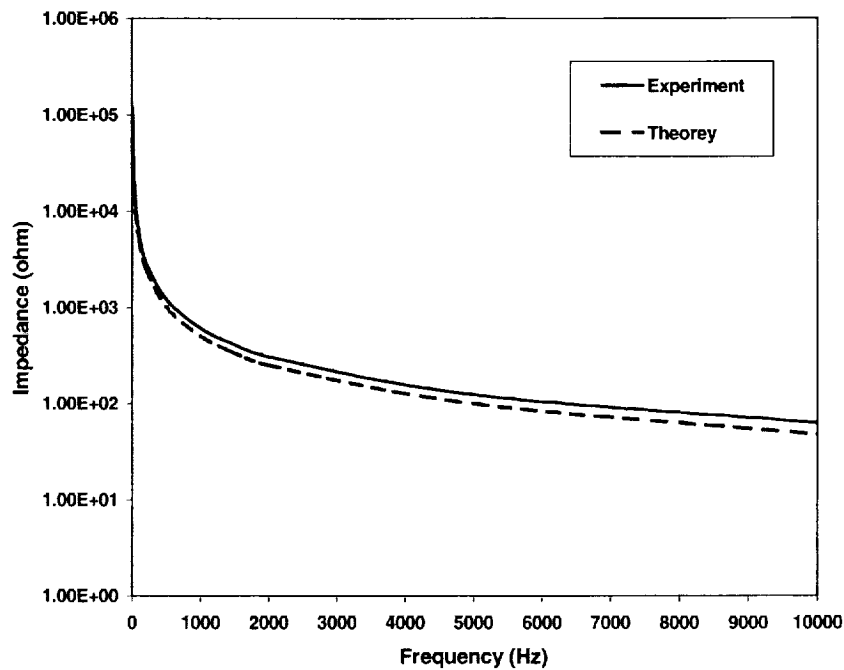


Figure 18. Analytical and experimental Impedance of PZT

ohm. Based on these measurements, it is reasonable to treat the resistor values of our specimens at high frequencies as short circuits. It should be noted that the smaller the size of the PZT, the larger the resistance value is, as shown in Figure 19. This can be understood as considering that the resistance is not proportional to the area of a capacitor.

These resistance values are analyzed to choose a correct circuit model of PZT with a voltage source. In circuit model in Figure 14(a), the fact that the capacitor displays high impedance at low frequencies makes the total resistance to be an open circuit. In circuit model in Figure 14(b), the total resistance becomes the same as the final resistance value. For example, $R_f = 20$ ohm for a middle specimen. The latter analysis does not agree with the experimental result at low frequencies. When we consider the circuit analyses of the two models in the high frequency range, the total resistance values of a circuit model of Figure 14(a) become the final resistance, R_f . However, in case of Figure 14(b), the voltage source equals zero, considering the capacitor to be a short circuit. This is another

contradiction. Therefore, the circuit model in Figure 14(b) does not well represent the characteristic behavior of PZT material.

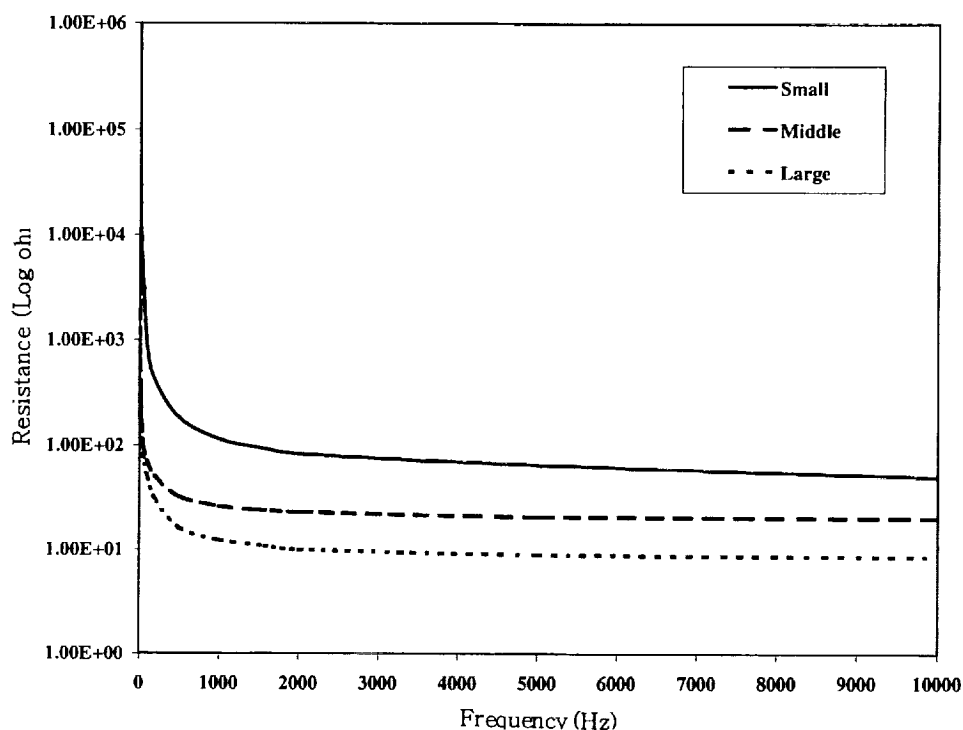


Figure 19. Resistor values of three different sizes of PZTs.

Experimental confirmation of a selected PZT model

We verified and analyzed the best choice of two commonly used models of PZT. However, we still need to confirm the selected circuit model and check the assumptions that the impedance of a capacitor behaves like an open circuit at low frequencies and like a short circuit at high frequencies. To do this task, an extra resistor (1000 ohm) is connected in series or in parallel with the PZT (middle size) as shown in Figure 17(b) and 17(c). Also, the corresponding circuit models can be seen in Figure 17.

Figure 20 shows impedance plots of the PZT only, PZT connected in series with an extra resistor, and PZT connected in parallel with an extra resistor. In series connection, the impedance is open at the low frequencies and asymptotes to an extra resistor value (1000 ohm) plus final resistance (20 ohm) for a middle size of PZT at the high frequencies. By considering an impedance equation for series connection, we can easily understand the impedance plots.

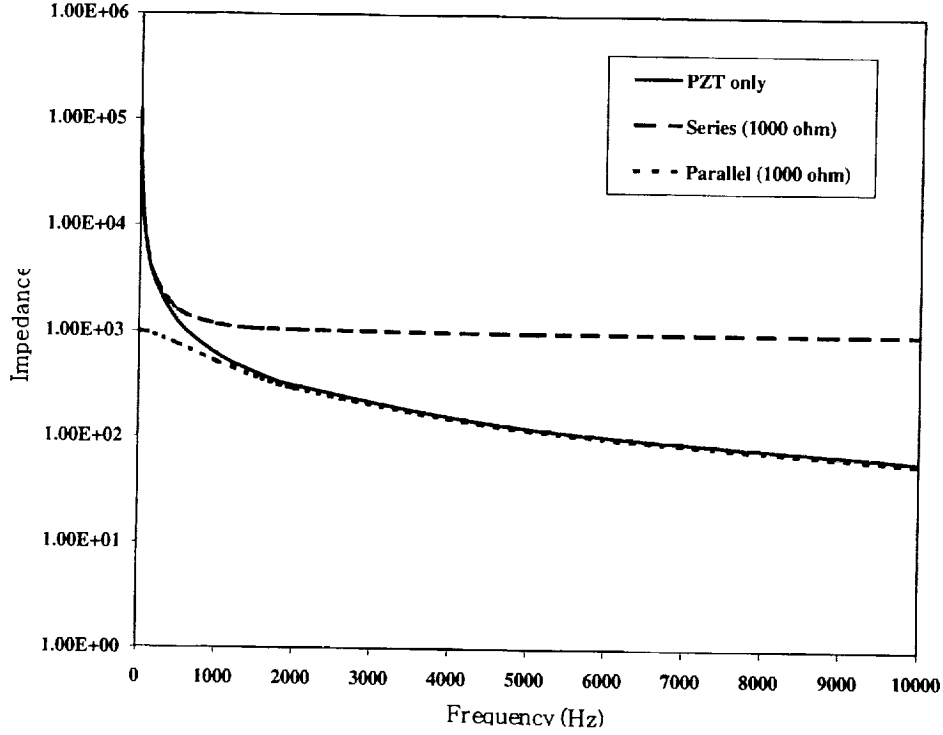


Figure 20. Impedances of the PZT only, PZT connected in series, PZT connected in parallel.

$$\begin{aligned}
 Z_{series}(j\omega) &= R_f + R_{ex} - \frac{j}{\omega C} \\
 &= \sqrt{R_f + R_{ex} + (1/\omega C)^2} \angle \arctan\left(\frac{-1/\omega C}{R_f + R_{ex}}\right) \\
 &= \frac{\sqrt{(\omega C)^2 (R_f + R_{ex})^2 + 1}}{\omega C} \angle -\arctan\left(\frac{1}{\omega C (R_f + R_{ex})}\right)
 \end{aligned} \tag{20}$$

In the parallel case, the impedance starts exactly at an extra resistor value (1000 ohm) at low frequencies and asymptotes to $\frac{R_f R_{ex}}{R_f + R_{ex}}$.

Figure 21 illustrates the resistance values of three cases. The resistor values of PZT connected in series with an extra resistor shift exactly 1000 ohm (an extra resistor value) up from the resistance values of PZT only, through the entire frequency range. In parallel connection with an extra resistor case, the behavior of resistance is same as that of impedance case.

One more thing we should check is phase angles for three different cases. As shown in Figure 22, the phase angle of PZT starts from -90 degree. This agrees well with the phase angle of a capacitor. However, the phase angle of PZT increases with increasing

frequency. This results in the PZT to be lost the fidelity of a capacitor. This is the reason why the shunt circuit in vibration control applications may not suppress the vibration amplitude in high frequency ranges. A negative capacitance shunt might solve this problem. Another point about shunt circuits is that the PZT material behaves inherently like a capacitor, resistance, and inductor at the electric resonant frequency as shown in Figure 13. We can use these electric components for a resonant shunt and match the mechanical resonance with an electric resonant frequency as changing the size and the thickness of PZT. The phase angle contour of a series connection with an extra resistor as shown in Figure 22 can be plotted using the phase angle equation (20).

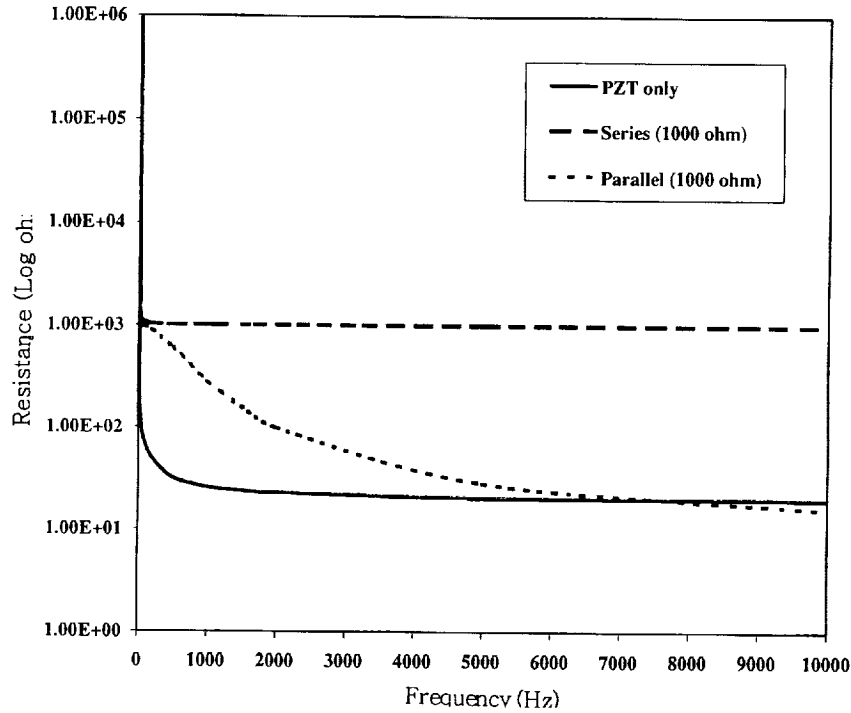


Figure 21. Resistances of the PZT only, PZT connected in series, PZT connected in parallel.

Summary

An analytical model of the electric impedance of piezoelectric material has been presented. The theoretical analysis was compared with the experimental measurements using an Impedance Analyzer to verify the reliability of the analytical models. Two models of a piezoceramic material have been considered and compared through a series of experiments. The correct choice of a circuit model of PZT was chosen. To confirm the selected PZT circuit model and to validate assumptions made, a second experiment was performed consisting of connecting an extra resistor to the selected model. In the view of these results, the model connected in series between a capacitor and a voltage source with a resistor, properly represents the characteristic behavior of PZT material over a broad frequency range.

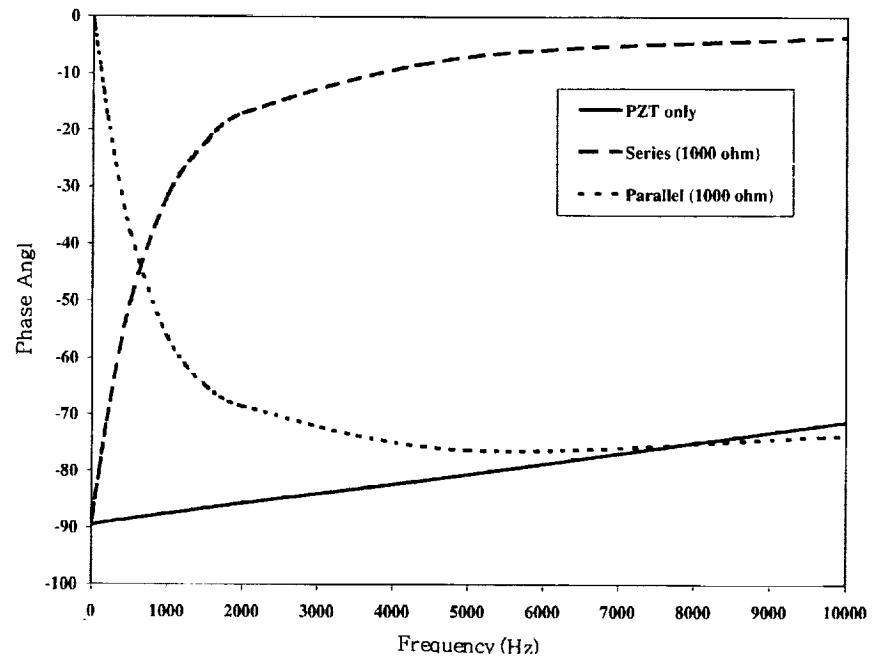


Figure 22. Phase angles of the PZT only, PZT connected in series, PZT connected in parallel.

IV. Mathematical Modeling of Bending Actuators

Modeling of beam type Unimorph and Bimorph actuators is presented in this section. The discussion presented herein stems from the work of (Bailey and Hubbard, 1985), (Crawley and de Luis, 1987), (Crawley and Anderson, 1990), and (Chaudhry and Rogers, 1994). While other researchers have performed similar research in this area, these authors were the principle scientists in developing the technology used today in the analysis of simple piezoceramic actuators such as the Unimorph and Bimorph. The models developed for the analysis of these actuators started simple and progressively became more complicated as the limitations of the models were shown and the need for increased accuracy became apparent. The first models developed were the Pin-Force and Enhanced Pin-Force models. These models, while rendering reasonable good static results for actuators within certain thickness (or stiffness) ratios, are generally not suitable for detailed analysis. However, examination of these models is helpful in developing an understanding of the mechanics of piezoceramic actuation. A more detailed and accurate model that will be presented in this section is the Euler-Bernoulli model. This model gives good results for a much wider range of actuator thickness ratios. Finally, energy and variational method approaches are employed to derive the governing equations.

For the purpose of illustrating the analysis methodology employed in the various modeling methods, several example problems will be solved using the Pin-Force, Enhanced Pin-Force, Euler-Bernoulli beam models as well as the variational method. Unless otherwise stated explicitly in the model, the beam is assumed to be long and slender in accordance with the primary assumptions introduced by the Euler beam model. It is emphasized that the primary differences between the models lie in the treatment of the actuator stiffness and the resulting interactions with the substrate. A Unimorph and Bimorph geometric configuration are considered in this analysis. The Unimorph beam actuator is shown in Figure 4.1. Other configurations are also considered in this study.

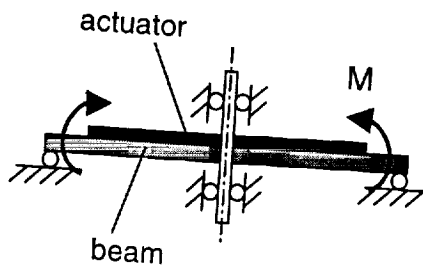


Figure 4.1. Unimorph actuator with roller boundary at the ends and guided at the center.

Piezoceramic Actuators

Piezoceramic actuators come in many geometric and material configurations. Among the most common configurations are the Unimorph and Bimorph. While the most popular geometric shape of these actuators is a slender beam, plates of various geometric shapes have been developed for specific applications. The Unimorph configuration utilizes a single piezoceramic element laminated to a substrate to produce transverse deflection through bending of the structure due to the induced in-plane strain by excitation of the piezoceramic. The Bimorph configuration uses two piezoceramic elements laminated either together or to a substrate to produce transverse deflection through bending of the structure due to the opposing induced in-plane strain by excitation of the two piezoceramic actuators. Nominally, steel substrates are used in both configurations although brass and aluminum have been successful alternatives.

The two configurations and the orientation of the piezoceramic elements are shown in Figure 4.1.

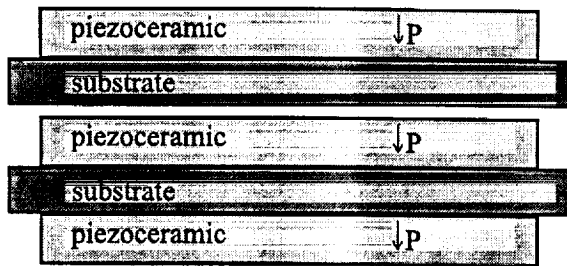


Figure 4.1. Unimorph and Bimorph piezoceramic actuators.

The piezoceramic stack actuator is also very popular but its use is limited due to many design and material constraints. The stack actuator uses a distinctly different actuation mode to produce displacement when compared to the Unimorph or Bimorph. The stack actuator utilizes through the thickness induced strain to create displacement in the direction of the stack. Other piezoceramic actuators utilize induced shear deformations to produce deflections of a structure. Figure 4.2 shows the piezoelectric actuation modes used by Unimorph or Bimorph actuators, stack actuators and shear type actuators. Table 4.1 lists the relative comparisons of common actor types in terms of displacement produced, force generated, energy transfer efficiency and natural frequency.

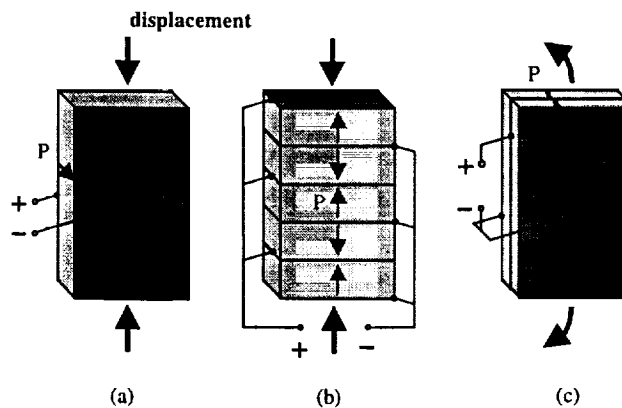


Figure 4.2 Displacement generation modes for different actuation modes.

	Displacement Generated	Force Generated	Electro-mechanical Energy Transfer Efficiency	Resonant Frequency
Single Layer	Low	Medium	Medium	Medium
Stack	Medium	High	High	High
Bimorph / Unimorph	High	Low	Low	Low

Table 1.1. Comparison of different piezoelectric actuator types (Lee et al., 1997).

Bimorphs and Unimorphs can be obtained commercially in several different material orientations. Because of the extreme versatility and popularity of these beam type actuators,

detailed description of the actuation methods and material orientations are presented in this section. It should be noted that induced strain actuators such as the Unimorph and Bimorph rely on the d_{31} type or in-plane induced strain. Figures 4.3, 4.4 and 4.5 show different configurations of induced strain actuators.

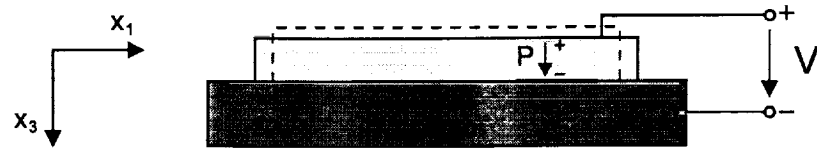


Figure 4.3: Unimorph: actuation of the unsymmetric structure.

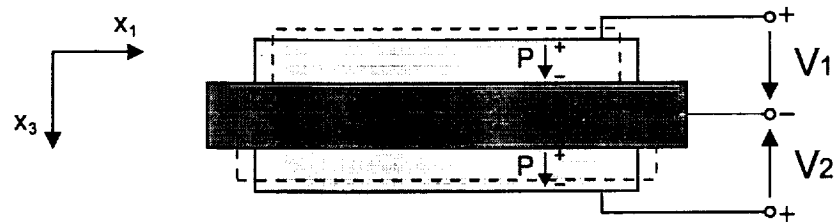


Figure 4.4: Bimorph: actuation of the symmetric structure.

Figure 4.4 shows an electrical parallel connection for Bimorphs. This connection is the most popular because it is simple to use. Two power supplies may be used to realize the full allowable voltage fields in the piezoceramic (the allowable fields are typically not symmetric about 0). Alternately, one supply may be used with inputs limited by the more severe field limitation on the piezoceramics (typically the piezoceramic with the field opposing the poling direction).

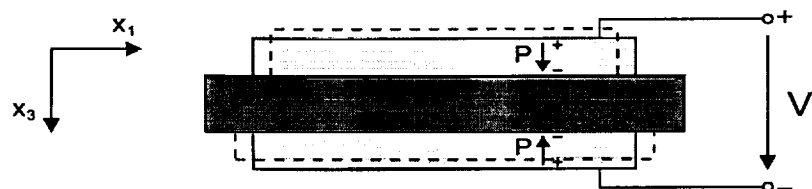


Figure 4.5. Common Bimorph actuator.

Mathematical modeling of Unimorph and Bimorph beam type actuators

Modeling of beam type Unimorph and Bimorph actuators is presented in this section. The discussion presented herein stems from the work of Bailey and Hubbard (85), Crawley and de Luis (87), Crawley and Anderson (90), and Chaudhry and Rogers (94a, 94b) as well as work initiated by the authors. While other researchers have performed similar research in this area, these authors were the principle scientists in developing the technology used today in the analysis of simple piezoceramic actuators such as the Unimorph and Bimorph. The models developed for the analysis of these actuators started simple and progressively became more complicated as the limitations of the models were shown and the need for increased accuracy became apparent. The first models developed were the Pin-Force and Enhanced Pin-Force models. These models, while rendering reasonable good static results for actuators within certain thickness (or stiffness) ratios, are generally not suitable for detailed analysis. However, examination of these models is helpful in developing an understanding of the mechanics of

piezoceramic actuation. A more detailed and accurate model that will be presented in this section is the Euler-Bernoulli model. This model gives good results for a much wider range of actuator thickness ratios. Finally, energy and variational method approaches are employed to derive the governing equations.

For the purpose of illustrating the analysis methodology employed in the various modeling methods, several example problems will be solved using the Pin-Force, Enhanced Pin-Force, Euler-Bernoulli beam models as well as the variational method. Unless otherwise stated explicitly in the model, the beam is assumed to be long and slender in accordance with the primary assumptions introduced by the Euler beam model. It is emphasized that the primary differences between the models lie in the treatment of the actuator stiffness and the resulting transfer interactions with the substrate. A Unimorph and Bimorph geometric configuration considered in this analysis is shown in Figure 4.6. Other configurations are also considered in this document.

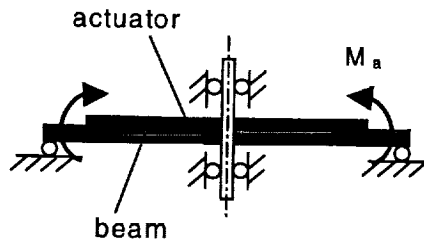


Figure 4.6. Unimorph actuator with roller boundary at the ends and guided at the center.

In general, the total strain in an piezoelectric actuator is defined by:

$$\epsilon_{total} = \epsilon_{mech} + \Lambda \quad \text{where} \quad \Lambda = d_{ij} E_i \quad (4.1)$$

ϵ_{mech} denotes the mechanical strain in the actuator and Λ is the free induced strain, which is the product of the piezoelectric constant d_{ij} and the applied electric field E in the direction of the poling axis. The free induced strain is analogous to free thermal strain as it is a principle strain. This strain causes a moment that acts on the beam resulting in bending. It is comparable to a temperature change on a bimetallic thermostat.

The Pin-Force-Model

The Pin-Force actuation model of Unimorph and Bimorph structures describes the mechanical interaction between the piezoceramic and substrate elements as the interaction between two separate but pin-connected structures. The pin connections exist at the extreme ends of the piezoceramic elements and implies the assumption of perfect bonding between the piezoceramic and substrate and that the adhesive layer is infinitely stiff. Figure 4.3 shows the separation of the elements for modeling purposes (Chaudhry and Rogers, 1994). In reality, the assumption of perfect bonding is never completely realized. This assumption becomes increasingly inaccurate as the bonding layer thickness increases and the bonding material stiffness decreases. Further, this model forces the shear stress in the piezoceramic to be concentrated at a very small region near the ends (near the pins). The normal strain divided by λ is shown over the actuator length in Figure 4.2. These models requires strain continuity at the actuator-substrate interface which in this case is at the pins. The parameter Γ indicates the effectiveness of the shear transfer (Crawley and de Luis, 1987).

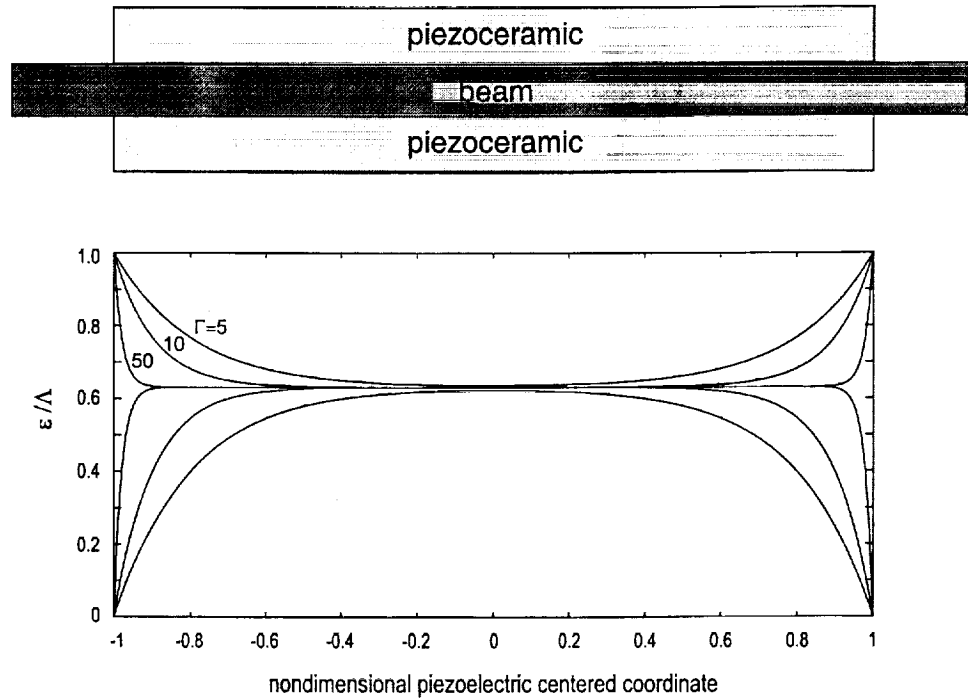


Figure 4.2. Shear strain distribution approach perfect bonding.

In the pin-force model, the strain in the substrate is considered to follow traditional Euler-Bernoulli beam theory wherein the variation is linear through the thickness. However, the strain in the piezoceramic is assumed to be constant through the thickness. The treatment of the bending stiffness of the piezoceramic actuators results in limitations and inaccuracies. The pin-force method ignores the bending stiffness of the piezoceramic patches completely which results in severe inaccuracies when the stiffness ratio of the substrate to actuator becomes larger than approximately 5. It should be noted that this model gives reasonable results for configurations wherein the bending stiffness of the substrate is significantly larger than the bending stiffness of the actuator. While this may be the case for some induced strain actuators used in vibration and structural control applications, it is rarely the case for Unimorph and Bimorph actuators.

The pin-force model is presented here in detail in order to predict the response of Unimorphs and Bimorphs based on this theory. The beam and actuators are considered as separate elastic bodies with the strain states as indicated in Figure 4.3.

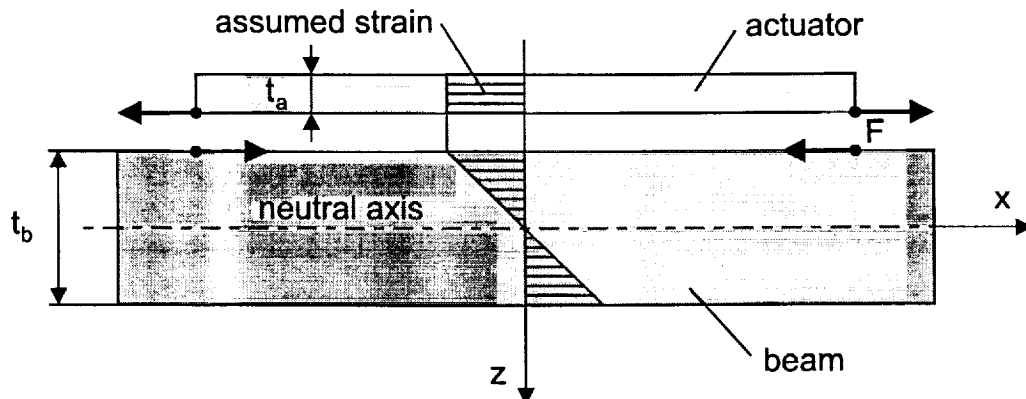


Figure 4.3. Pin-force model strain state for an Unimorph actuator in pure bending.

The total strain in the Unimorph piezoceramic actuator can be written as:

$$\varepsilon_a = \frac{\sigma_a}{E_a} + \Lambda, \text{ where } \Lambda = d_{31} E_3, \sigma_a = \frac{F}{A_a} \text{ and } A_a = b t_a. \quad (4.2)$$

It should be noted that the strain is composed of two parts: an axial stretching term $\frac{\sigma_a}{E_a}$ and an induced strain Λ . By substitution, the strain ε_a can be written as:

$$\varepsilon_a = \frac{F}{E_a b t_a} + \Lambda. \quad (4.3)$$

The strain in a bending beam is written as:

$$\varepsilon_b = -\frac{t_b}{2} \kappa, \text{ where } \kappa \text{ is the curvature of the beam.} \quad (4.4)$$

At the interface between the actuator and the beam, strain continuity is required thus yielding:

$$-\frac{t_b}{2} \kappa = \frac{F}{E_a b t_a} + \Lambda. \quad (4.5)$$

The beam moment equation can be written as:

$$M = F \frac{t_b}{2} = (EI)_b \kappa. \quad (4.6)$$

Upon solving for the curvature in Equation 4.5, substitution into 4.6 and solving, the force acting at the pins connecting the actuator and the substrate can be written as:

$$F = -\frac{E_b b t_b}{3 + \Psi} \Lambda, \text{ where } \Psi = \frac{E_b t_b}{E_a t_a}. \quad (4.7)$$

Substituting the force F back into Equation 4.7 yields the moment acting on the beam as:

$$M_{Unimorph} = -\frac{E_b b t_b^2}{2(3 + \Psi)} \Lambda \quad (4.8)$$

In the case of a Bimorph, the beam moment equation is written as:

$$M_{Bimorph} = F t_b = (EI)_b \kappa. \quad (4.9)$$

The neutral axis for the Bimorph and Unimorph are exactly at the neutral axes of the substrate because the bending stiffness of the piezoceramic is neglected in this model. Following the derivation procedure presented in Equations 3.2 through 4.8, the moment acting on the Bimorph is derived as:

$$M_{Bimorph} = -\frac{E_b b t_b^2}{6 + \Psi} \Lambda. \quad (4.10)$$

Given the moment acting on the beam, the deflection and slope of the beam can be determined using classical beam theory solutions.

It should be noted again that the limitations of this model are significant when considering a structure and actuation method that induces bending. The model completely ignores the bending of the actuator(s) and assumes that all of the force produced by the actuator results in bending of the substrate. In reality, this never occurs as the actuators must move with the structure to which they are bonded. The pin-force model predicts results that are reasonable only in the

cases of extremely thin actuators mounted to relatively stiff structures, and in Bimorph (symmetric) structures wherein the excitation is completely in-phase and the structure experiences only in-plane deformations. The latter case does not result in any transverse deflection and again is limited to structures that are relatively stiff compared to the actuators. Figure 4.4 depicts the mechanics of the pin-force model bending.

Pin-Force model

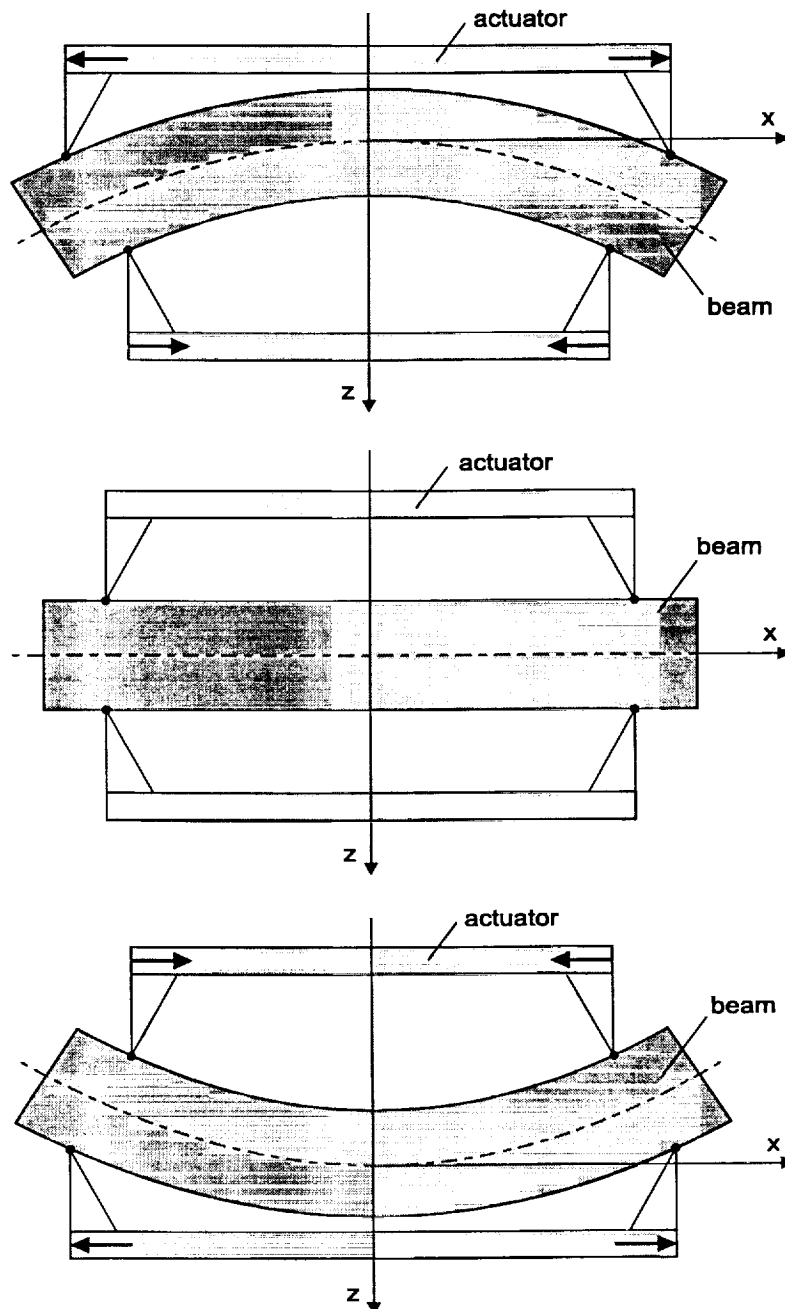


Figure 4.4. Pin-Force model of induced strain bending.

Enhanced Pin-Force-Model

The Enhanced Pin-force model is an improvement over the Pin-Force model because an attempt to account for the bending stiffness of the actuator(s) is made. However, the piezoceramic actuators are assumed to bend around their own neutral axes which is assumed to be at their geometric center. In essence, this assumption treats the piezoceramic actuators and the substrate as separate structures only pinned together at the piezoceramic edges. The strain in the piezoceramic is assumed to be composed of two parts: a constant term and a linearly varying term. The constant term is assumed to contribute to the bending moment applied to the substrate, and the linearly varying term is assumed to contribute only to the bending of the piezoceramic. Continuity of strain is assumed at the piezoceramic-substrate interface. Also this assumption has severe inaccuracies when the stiffness ratio of the substrate to the actuator becomes larger than approximately 2.0. The strain state for a Unimorph considered under the assumptions of the Enhanced Pin-Force method is shown in Figure 4.5.

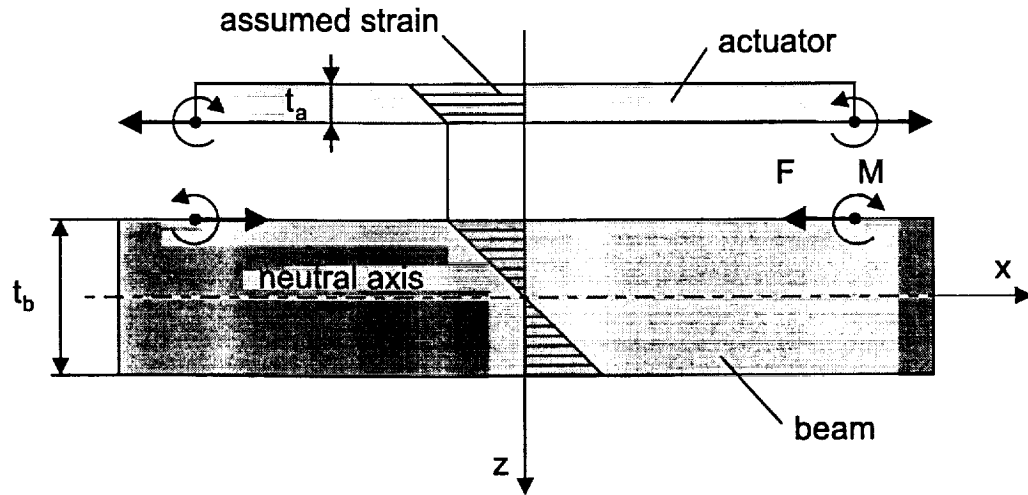


Figure 4.5. Enhanced Pin-Force model assumed strain state.

Determination of the governing equations follows the form presented for the Pin-Force model in section 3.1. The strain in the piezoceramic actuator at the piezoceramic-substrate interface is written as:

$$\epsilon_a = \frac{\sigma_a}{E_a} + \Lambda, \text{ where } \Lambda = d_{31} E_3, \quad \sigma_a = \frac{F}{A_a} \text{ and } A_a = b t_a. \quad (4.11)$$

It should be noted that the strain given in Equation 4.11 is a simplification to reality, and is a limitation in the model. The moment acting on the substrate that induces bending in the substrate only is written as:

$$M = F \frac{t_b}{2} - M_a = (EI)_b \kappa, \quad \text{where } M_a = (EI)_a \kappa. \quad (4.12)$$

The moment applied to the beam as given in Equation 4.12 is the moment calculated in the Pin-Force model less the moment(s) applied to the piezoceramic to induce the bending of that member(s). The major assumption implied by this is that the bending moment applied to the piezoceramics can be represented with a combination of the curvature of the beam κ and the

bending stiffness of the piezoceramics about their centroidal axis. In reality, the curvature of the actuators can not be the same as the beam curvature because the actuators do not bend about their own centroidal axis. This is a limitation of the model but is an attempt to account for the actuator bending stiffness within the assumptions made.

Substituting Equations 4.11 into 4.12 and solving for F leads to:

$$F = -\frac{E_a b t_a (\Psi T^2 + 1)}{T^2 \left(3 + \Psi + \frac{1}{T^2}\right)} \Lambda, \quad \text{where } \Psi = \frac{E_b t_b}{E_a t_a}, \text{ and } T = \frac{t_b}{t_a}. \quad (4.13)$$

Substituting the force F back into Equation 4.12, and solving for the moment acting on the beam leads to:

$$M_{Unimorph} = -\frac{E_a b t_a^2 (\Psi T^2 + 1)}{2 T \left(3 + \Psi + \frac{1}{T^2}\right)} \Lambda. \quad (4.14)$$

Following the derivation method presented in Equations 4.11 through 4.14, the moment acting on the Bimorph is calculated as:

$$M_{Bimorph} = -\frac{E_a b t_a^2 (\Psi T^2 + 2)}{T \left(6 + \Psi + \frac{2}{T^2}\right)} \Lambda. \quad (4.15)$$

Figure 4.6 depicts the mechanics of the Enhanced Pin-Force model actuation modes. Equations 4.14 and 4.15 are used with classical beam theory solutions as shown in the examples section.

Euler-Bernoulli Model

The Euler-Bernoulli model is the classic beam theory approach to modeling the induced-strain actuation of the piezoceramic actuator(s). This model is not limited by the same shortcomings as the Pin-Force and Enhanced Pin-Force models. The Euler-Bernoulli model predicts the correct curvature of substrate and actuator over the entire contact area between actuator and substrate. The actuator is considered to be a layer of the beam, and perfect bonding between piezoceramic and substrate is assumed. The bending axis of the composite beam is the true neutral axis about which both, substrate and actuator(s) bend. Due to the distinct differences between symmetric and anti-symmetric cases (Unimorph and Bimorph), both sets of governing equations are derived in this section.

Symmetric Model - Bimorph

The conventional derivation as detailed by (Chaudhry and Rogers, 1994) is shown in this section. The actuators and substrate are considered as composite bodies with a continuous strain state as shown in Figure 4.7. Due to the symmetry, the neutral axis of the actuator and substrate system is at the geometric center of the substrate.

Enhanced Pin-Force model

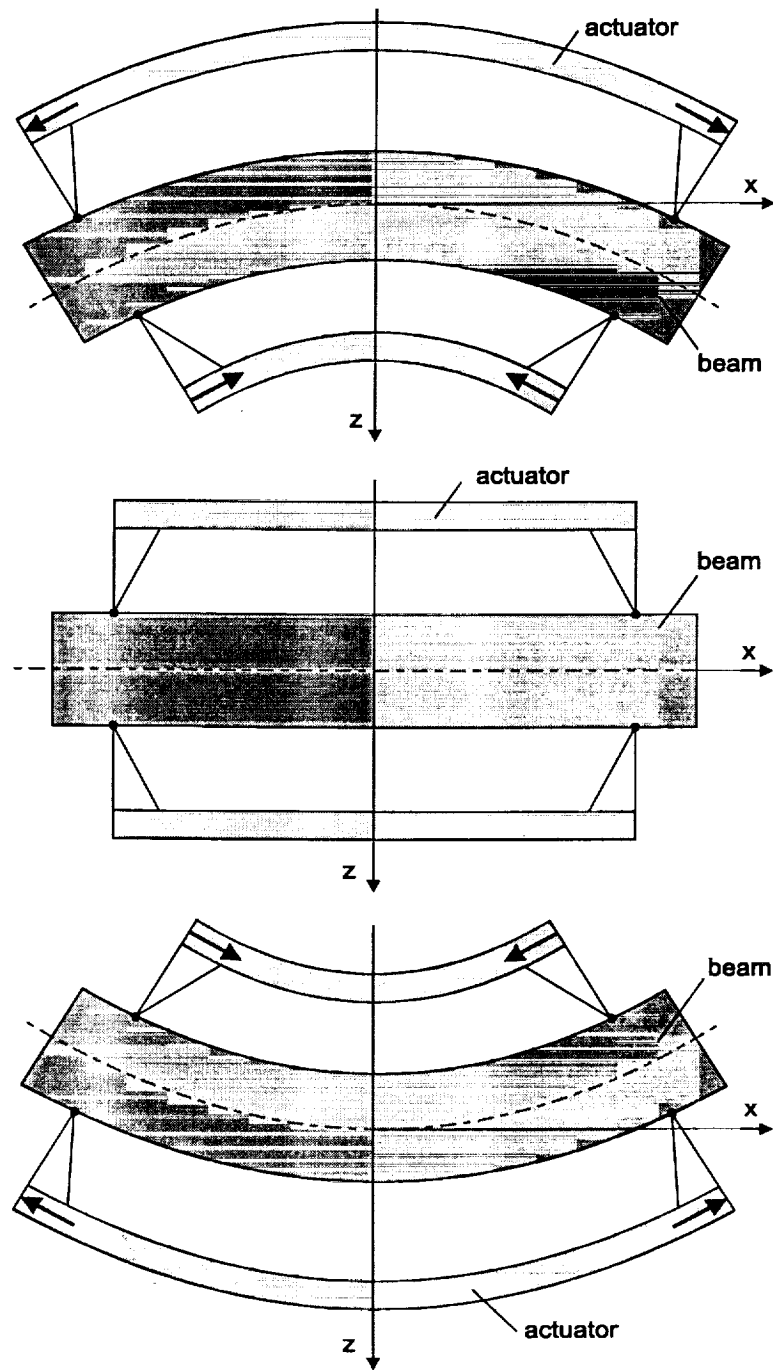


Figure IV.1. Enhanced Pin-Force model actuation modes.

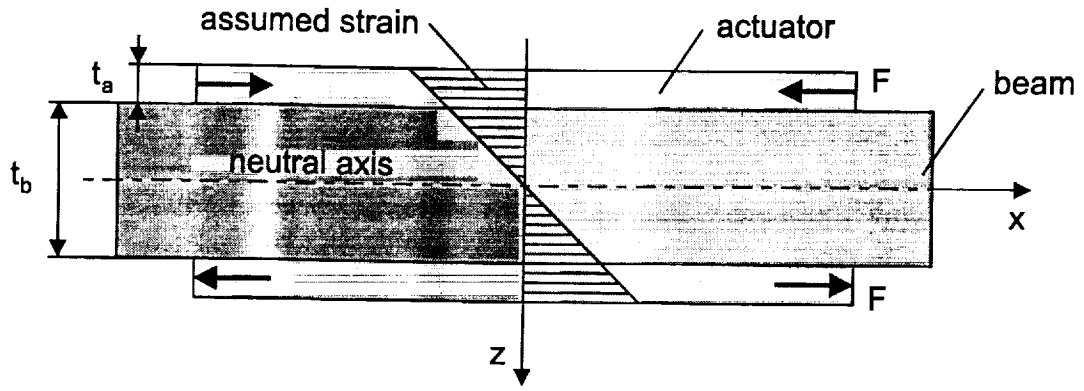


Figure 4.7. Symmetrically bonded actuators – Bimorph.

To determine the bending moments acting on the piezoceramic actuators and the substrate, the stress is integrated over the thickness. The integration margins are abbreviated with a_i , where $a_1 = t_a + \frac{t_b}{2}$, $a_2 = \frac{t_b}{2}$, $a_3 = -\frac{t_b}{2}$ and $a_4 = -\left(\frac{t_b}{2} + t_a\right)$. The bending moment on the lower actuator is determined by:

$$M_a = \int_{a_2}^{a_1} z \sigma_a b dz, \text{ where } \sigma_a = E_a (\varepsilon_a - \Lambda) = -E_a (z \kappa + \Lambda). \quad (4.16)$$

Because of symmetry of the actuators, the total acting moment is twice the quantity calculated in Equation 4.16. Substituting the appropriate values, the governing integral for the moment on the actuators takes the form:

$$M_a = -2 E_a b \int_{a_2}^{a_1} (\kappa z^2 + \Lambda z) dz. \quad (4.17)$$

Examination of Equation 4.17 reveals that the moment M_a is composed of two distinct parts. The first is a bending term arising from the curvature induced into the actuators. The second term relates the induced strain actuation. The terms can be kept separate through the integration resulting in:

$$M_a = -E_a b \frac{2}{3} (a_1^3 - a_2^3) \kappa - E_a b (a_1^2 - a_2^2) \Lambda. \quad (4.18)$$

It should be noted that M_a is the moment in the piezoceramic part of the structure. It is composed of an active induce-strain part and a bending part. This term is not the actuation moment.

Integration of the stress over the beam thickness results in the moment acting on the beam. This takes the form of:

$$M_b = \int_{a_3}^{a_2} z E_b \varepsilon_b b dz = -E_b b \frac{1}{3} (a_2^3 - a_3^3) \kappa, \text{ where } \varepsilon_b = -z \kappa. \quad (4.19)$$

Because there must be a balance of the moment between the piezoceramic and the beam, we equate the right hand sides of Equations 4.18 and 4.19 to yield:

$$E_a b (a_1^2 - a_2^2) \Lambda = -b \frac{1}{3} (2 E_a (a_1^3 - a_2^3) - E_b (a_2^3 - a_3^3)) \kappa. \quad (4.20)$$

Alternatively, Equation 4.20 can be written as:

$$M = -((EI)_a + (EI)_b) \kappa, \quad (4.21)$$

where M is the actuation moment acting on the beam. Classical beam solutions can be applied with Equation 4.21 to determine the deflection and slope along the length of the beam. Sample problems are solved and presented in Section 4.4.

Euler-Bernoulli model

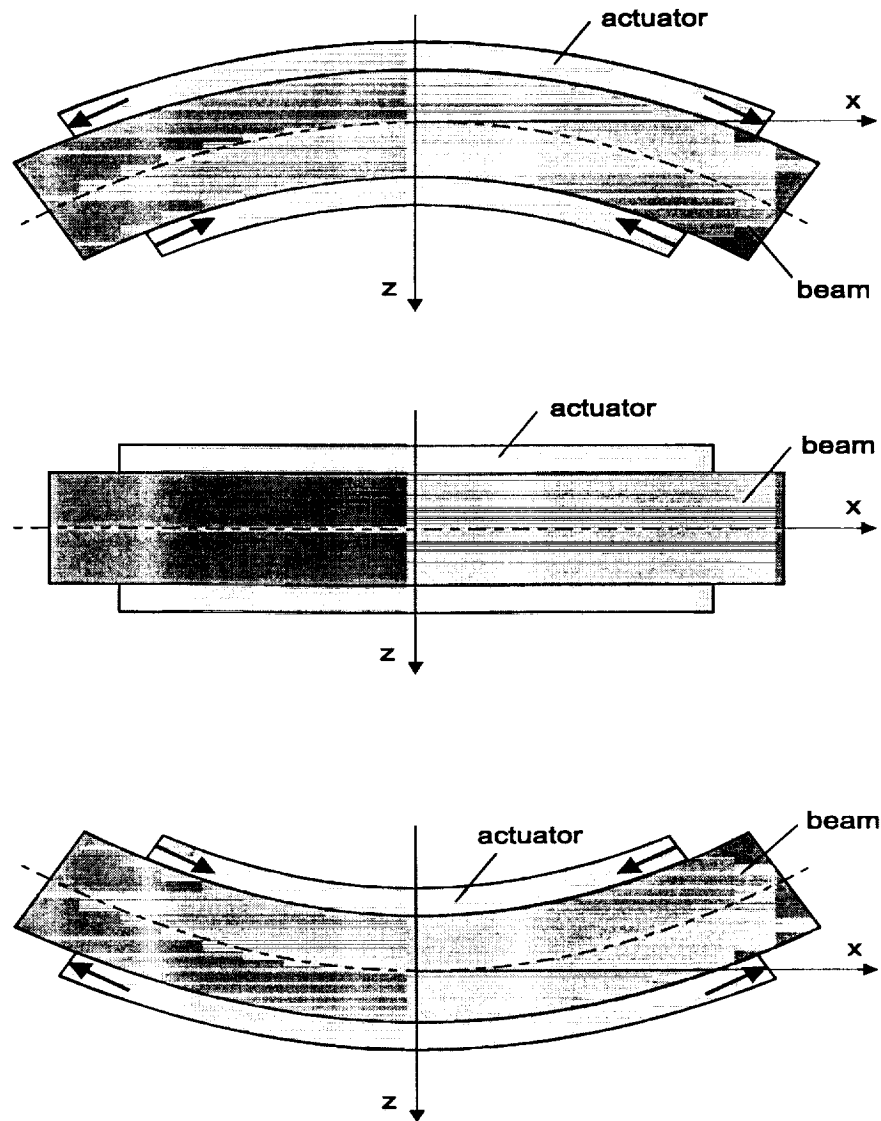


Figure IV.2. Euler-Bernoulli model actuation modes.

Unsymmetric Model - Unimorph

An unsymmetric structure such as a Unimorph is slightly more complicated as the symmetry simplifications utilized in the Bimorph model no longer apply. The assumed strain state for the Unimorph geometry is shown in Figure 4.9.

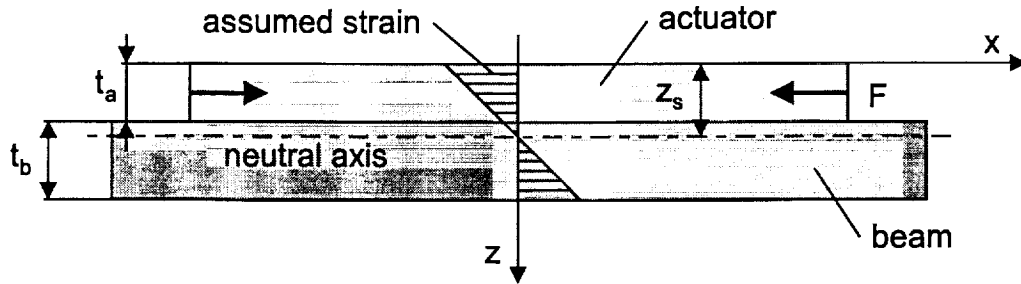


Figure 4.9. Unimorph geometry and assumed strain state.

Due to the unsymmetric configuration, the neutral axis lies at some distance from the geometric center axis. This can be treated in different manners as demonstrated by (Chaudhry and Rogers, 1994). The approach taken in this work is the calculation of the true neutral axis and subsequently bending about that axis. The neutral axis is calculated as detailed in most solid mechanics texts and shown in Figure 4.10.

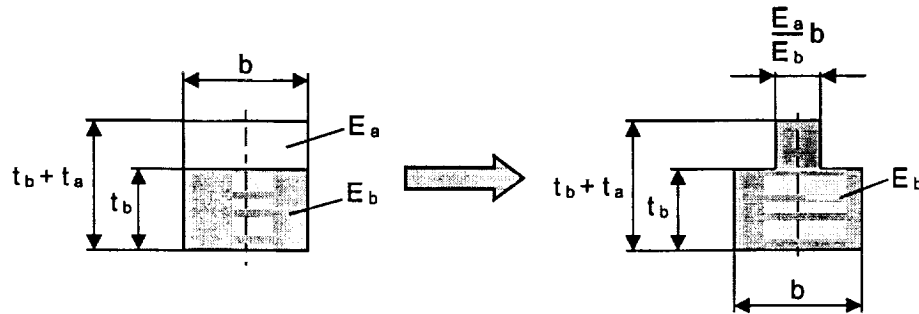


Figure 4.10. Modulus weighted calculation of the neutral axis.

In accordance with the modulus-weighted properties for composite sections as detailed by (Pilkey, 1994, p.38 or Shames, 1975, p.194), the calculation of the distance to the neutral axis from the piezoceramic surface (at $z = 0$) can be written as:

$$z_s = \frac{\sum_{i=1}^n z_i \frac{E_i}{E_r} A_i}{\sum_{i=1}^n \frac{E_i}{E_r} A_i} = \frac{\frac{t_a}{2} \frac{E_a}{E_b} + \left(\frac{t_a + t_b}{2} \right) t_b}{t_a \frac{E_a}{E_b} + t_b}, \quad (4.22)$$

where A_i are the areas, E_i the moduli of elasticity, z_i the distance to the center of each area. The beam modulus is chosen as the reference modulus E_r which leads to the new actuator width b_a .

Accounting for the proper limits of integration, the bending moment in the piezoceramic can be calculated by integration of the stress over the cross-section. The correct limits of integration

are: $a_1 = t_a + t_b - z_s$, $a_2 = t_a - z_s$ and $a_3 = -z_s$. The moment in the piezoceramic can be written as:

$$M_a = \int_{a_3}^{a_2} z \sigma_a b_a dz, \quad \text{where } \sigma_a = E_b \varepsilon_a = -E_b (z\kappa + \Lambda) \text{ and } b_a = \frac{E_a}{E_b} b. \quad (4.23)$$

Upon substitution, the moment becomes:

$$M_a = -E_a b \int_{a_3}^{a_2} (\kappa z^2 + \Lambda z) dz. \quad (4.24)$$

Evaluation of the integral leads to the moment M_a , which may be partitioned into an acting and a stiffness part as shown in Equation 4.25.

$$M_a = -E_a b \frac{1}{3} (a_2^3 - a_3^3) \kappa - E_a b \frac{1}{2} (a_2^2 - a_3^2) \Lambda. \quad (4.25)$$

Integration of the stress over the beam cross section yields the moment acting on the beam as:

$$M_b = \int_{a_2}^{a_1} z E_b \varepsilon_b b dz, \quad \text{where } \varepsilon_b = -z\kappa. \quad (4.26)$$

Upon substitution and integration, the bending moment in the beam becomes:

$$M_b = -E_b b \frac{1}{3} (a_1^3 - a_2^3) \kappa. \quad (4.27)$$

To maintain a balance of moments, the moments in the piezoceramic and beam are equated thereby yielding:

$$E_a b \frac{1}{2} (a_2^2 - a_3^2) \Lambda = -b \frac{1}{3} (E_a (a_2^3 - a_3^3) - E_b (a_1^3 - a_2^3)) \kappa \quad (4.28)$$

Using the definition of the moments and inertia, the governing equation can be deduced from Equation 4.28 as:

$$M = -((EI)_a + (EI)_b) \kappa \quad (4.28)$$

It should be noted that the acting moment M arises from the piezoceramic moment equation 4.24. Equation 4.28 can be used with classical beam equation solutions to predict the state of structure as a function of applied field.

Euler-Bernoulli model

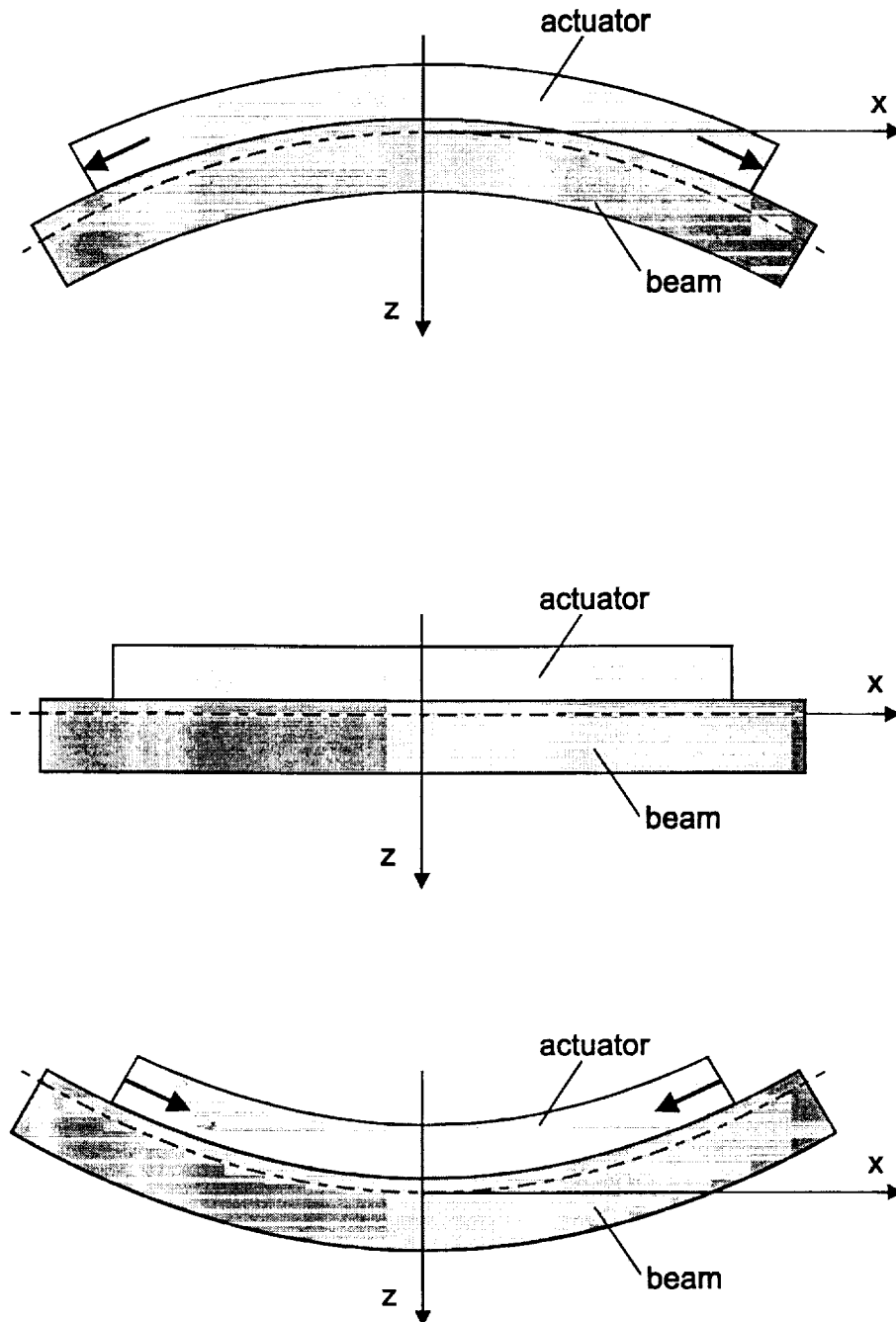


Figure IV.3. Euler-Bernoulli model mode of an Unimorph.

Multilayer Actuator - Energy Based Derivation of the Governing Equations

The governing equations of any beam structure can readily be derived from energy principles. The energy formulation is presented in this section for multilayer beam structures. It is assumed in the derivation that any of the n total layers can be active. Figure 4.12 shows a

bimorph beam actuator, but is presented here to show notations of directions. In the derivation, any of the layers could be active.

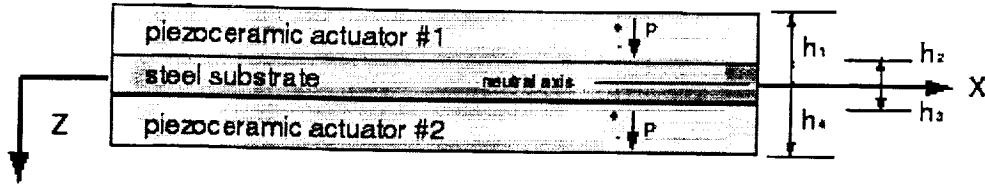


Figure 4.12. Beam definitions for the energy formulation.

Assuming moderate strains in a linear elastic Hookean material ($\sigma = Y \epsilon$, where Y is the Young's modulus) with properties that are constant along the length of the beam, the strain in any layer of the beam structure can be written as:

$$\epsilon = \frac{du}{dx} - z \frac{d^2w}{dx^2} - d_{31} E_3, \quad (4.30)$$

where d_{31} is the piezoelectric constant, E_3 is the electric field in that layer, u is the displacement in the x direction, and w is the displacement in the z direction. Note that the electric field E_3 is positive in the direction of the poling axis. The total potential energy of the structure is found as the integral over the volume of one-half the product of the stress and strain as:

$$\Pi = \int_{\text{volume}} \frac{1}{2} \sigma \epsilon dV = \int_{\text{volume}} \frac{1}{2} Y \epsilon^2 dV. \quad (4.31)$$

The governing equation for the deflection is obtained by minimization of the total potential energy. This is determined in this case by setting the first variation of the total potential energy to zero. Due to the composite nature of the beam, the integration through the thickness must be separated into distinct integrals. The first variation of the total potential energy takes on the form:

$$\delta \Pi = \int_{\text{volume}} Y \epsilon \delta \epsilon dV = 0 \quad (4.32)$$

Upon substitution of the strains in the materials, the integral takes on the form:

$$\begin{aligned} \delta \Pi &= \int_0^L \sum_{i=1}^n \int_{h_i}^{h_{i+1}} \int_{-b/2}^{b/2} dw (Y \epsilon \delta \epsilon) dz dx \\ &= b \int_0^L \sum_{i=1}^n \int_{h_i}^{h_{i+1}} \left\{ Y_i \left(\frac{du}{dx} - z \frac{d^2w}{dx^2} - d_{31,i} E_{3,i} \right) \delta \left(\frac{du}{dx} - z \frac{d^2w}{dx^2} - d_{31,i} E_{3,i} \right) \right\} dz dx \end{aligned} \quad (4.33)$$

where b is the width of the beam, Y_i is the Young and the subscript i denotes the i^{th} layer. Noting that the variation $\delta (E_{3,i} d_{31})$ is zero along the length of the beam, the integral reduces to:

$$\delta \Pi = b \int_0^L \sum_{i=1}^n \int_{h_i}^{h_{i+1}} \left\{ Y_i \left(\frac{du}{dx} - z \frac{d^2w}{dx^2} - d_{31,i} E_{3,i} \right) \delta \left(\frac{du}{dx} - z \frac{d^2w}{dx^2} \right) \right\} dz dx. \quad (4.34)$$

Integration of this equation is best accomplished one term at a time to facilitate an understanding of the origin of each term in the resulting governing equations and boundary

conditions. To aid in the presentation of the results from each of the integrals, the following definitions from composite material analysis methods is presented:

$$\begin{aligned} A_{11} &= \sum_{k=1}^n \left[\int_{h_k}^{h_{k+1}} Y_k dz \right] \\ B_{11} &= \sum_{k=1}^n \left[\int_{h_k}^{h_{k+1}} Y_k z dz \right] \\ D_{11} &= \sum_{k=1}^n \left[\int_{h_k}^{h_{k+1}} Y_k z^2 dz \right]. \end{aligned} \quad (4.35)$$

Additionally, the following two actuation terms are defined:

$$\begin{aligned} A_{11}^* &= \sum_{k=1}^n \left[\int_{h_k}^{h_{k+1}} Y_k d_{31,i} E_{3,i} dz \right] \\ B_{11}^* &= \sum_{k=1}^n \left[\int_{h_k}^{h_{k+1}} Y_k d_{31,i} E_{3,i} z dz \right]. \end{aligned} \quad (4.36)$$

Using the definitions given in equations 4.35 and 4.36, the first of the integrals from equation 4.34 can be written as:

$$\begin{aligned} \delta \Pi_1 &= b \int_0^L \sum_{i=1}^n \int_{h_i}^{h_{i+1}} \left\{ Y_i \left(\frac{du}{dx} \right) \delta \left(\frac{du}{dx} \right) \right\} dz dx \\ &= b A_{11} \int_0^L \frac{du}{dx} \delta \left(\frac{du}{dx} \right) dx \\ &= b A_{11} \frac{du}{dx} \delta u \Big|_0^L - b A_{11} \int_0^L \frac{d^2 u}{dx^2} \delta u dx \end{aligned} \quad (4.37)$$

Integration of the second integral term of equation 4.34 results in:

$$\begin{aligned} \delta \Pi_2 &= b \int_0^L \sum_{i=1}^n \int_{h_i}^{h_{i+1}} \left\{ -Y_i z \left(\frac{d^2 w}{dx^2} \right) \delta \left(\frac{du}{dx} \right) \right\} dz dx \\ &= -b B_{11} \int_0^L \frac{d^2 w}{dx^2} \delta \left(\frac{du}{dx} \right) dx \\ &= -b B_{11} \frac{d^2 w}{dx^2} \delta u \Big|_0^L + b B_{11} \int_0^L \frac{d^3 w}{dx^3} \delta u dx \end{aligned} \quad (4.38)$$

Integration of the third term takes the form of:

$$\begin{aligned}
\delta \Pi_3 &= b \int_0^L \sum_{i=1}^n \int_{h_i}^{h_{i+1}} \left\{ -Y_i d_{31,i} E_{3,i} \delta \left(\frac{du}{dx} \right) \right\} dz dx \\
&= -b A_{11}^* \int_0^L \delta \left(\frac{du}{dx} \right) dx \\
&= -b A_{11}^* \delta u \Big|_0^L
\end{aligned} \tag{4.39}$$

It is interesting to note that the third integral, equation 4.39, results in a boundary term only. Further, this boundary term includes all to the actuation that induces in-plane stretching of the beam. The fourth integral term in equation 4.34 results in:

$$\begin{aligned}
\delta \Pi_4 &= b \int_0^L \sum_{i=1}^n \int_{h_i}^{h_{i+1}} \left\{ -Y_i z \left(\frac{du}{dx} \right) \delta \left(\frac{d^2 w}{dx^2} \right) \right\} dz dx \\
&= -b B_{11} \int_0^L \frac{du}{dx} \delta \left(\frac{d^2 w}{dx^2} \right) dx \\
&= -b B_{11} \frac{du}{dx} \delta \left(\frac{dw}{dx} \right) \Big|_0^L + b B_{11} \frac{d^2 u}{dx^2} \delta w \Big|_0^L - b B_{11} \int_0^L \frac{d^3 u}{dx^3} \delta w dx
\end{aligned} \tag{4.40}$$

The fifth integral term in equation 4.34 results in:

$$\begin{aligned}
\delta \Pi_5 &= b \int_0^L \sum_{i=1}^n \int_{h_i}^{h_{i+1}} \left\{ Y_i z^2 \left(\frac{d^2 w}{dx^2} \right) \delta \left(\frac{d^2 w}{dx^2} \right) \right\} dz dx \\
&= b D_{11} \int_0^L \frac{d^2 w}{dx^2} \delta \left(\frac{d^2 w}{dx^2} \right) dx \\
&= b D_{11} \frac{d^2 w}{dx^2} \delta \left(\frac{dw}{dx} \right) \Big|_0^L - b D_{11} \frac{d^3 w}{dx^3} \delta w \Big|_0^L + b D_{11} \int_0^L \frac{d^4 w}{dx^4} \delta w dx
\end{aligned} \tag{4.41}$$

The final integral term from equation 4.34 results another boundary term similar to the term in equation 4.39. This term takes the form:

$$\begin{aligned}
\delta \Pi_6 &= b \int_0^L \sum_{i=1}^n \int_{h_i}^{h_{i+1}} \left\{ Y_i d_{31,i} E_{3,i} z \delta \left(\frac{d^2 w}{dx^2} \right) \right\} dz dx \\
&= b B_{11}^* \int_0^L \delta \left(\frac{d^2 w}{dx^2} \right) dx \\
&= b B_{11}^* \delta \left(\frac{dw}{dx} \right) \Big|_0^L
\end{aligned} \tag{4.42}$$

Gathering the equations together into one yields the governing equations and boundary conditions. To that end, the summation of the six integrals is given as:

$$\begin{aligned}
\delta \Pi = & b \int_0^L \left(B_{11} \frac{d^3 w}{dx^3} - A_{11} \frac{d^2 u}{dx^2} \right) \delta u \, dx \\
& + b \int_0^L \left(D_{11} \frac{d^4 w}{dx^4} - B_{11} \frac{d^3 u}{dx^3} \right) \delta w \, dx \\
& + b \left(A_{11} \frac{du}{dx} - B_{11} \frac{d^2 w}{dx^2} + - A_{11}^* \right) \delta u \Big|_0^L \\
& + b \left(D_{11} \frac{d^2 w}{dx^2} - b B_{11} \frac{du}{dx} + B_{11}^* \right) \delta \left(\frac{dw}{dx} \right) \Big|_0^L \\
& + b \left(B_{11} \frac{d^2 u}{dx^2} - D_{11} \frac{d^3 w}{dx^3} \right) \delta w \Big|_0^L = 0
\end{aligned} \tag{4.43}$$

The governing equations are extracted from the integrals in Equation 4.43 and take the form:

$$\begin{aligned}
u: \quad B_{11} \frac{d^3 w}{dx^3} - A_{11} \frac{d^2 u}{dx^2} &= 0 \\
w: \quad D_{11} \frac{d^4 w}{dx^4} - B_{11} \frac{d^3 u}{dx^3} &= 0.
\end{aligned} \tag{4.44}$$

The boundary conditions at each end are likewise extracted from equation 4.43:

$$\begin{aligned}
A_{11} \frac{du}{dx} - B_{11} \frac{d^2 w}{dx^2} + - A_{11}^* &= 0 & \text{- or -} & \quad u = 0 \\
D_{11} \frac{d^2 w}{dx^2} - b B_{11} \frac{du}{dx} + B_{11}^* &= 0, & \text{- or -} & \quad \frac{dw}{dx} = 0 \\
B_{11} \frac{d^2 u}{dx^2} - D_{11} \frac{d^3 w}{dx^3} &= 0, & \text{- or -} & \quad w = 0
\end{aligned} \tag{4.45}$$

It is noted that the boundary conditions naturally result from the variational process. In essence, the mathematics completely determines the appropriate boundary conditions. While the boundary conditions for this simple beam are easy to discern, once moderate strain levels are allowed the boundary conditions are not readily discernable. Further, coupling between the in-plane stretching and the transverse deflection may exist depending on the geometry. Symmetry geometry structures yield the B_{11} term zero identically and the coupling is completely eliminated. However, the in-plane stretch and transverse deflection of non-symmetric structures are coupled at both the governing equation level and the boundary condition level. It should be noted that in this formulation, the moment and slope are complimentary variables, as well as the shear and the displacement. This is consistent with traditional beam theory as set forth in most mechanics texts.

The solution to the governing equations is readily achieved even for coupled cases. To arrive at a solution, the governing equation on u is differentiated once and inserted into the governing equation on w . The solution on w retains the general form as derived in most undergraduate mechanics of materials texts. Using this result, the general form of the solution on u can be found. The solutions on u and w are:

$$\begin{aligned}
w(x) &= c_1 x^3 + c_2 x^2 + c_3 x + c_4 \\
u(x) &= k_1 x + k_2 \frac{3 B_{11} c_1}{A_{11}} x^2.
\end{aligned}
\tag{4.46}$$

The final form of the u and w displacement equations can be arrived at only after specification of the boundary conditions. Common among boundary conditions is the simply supported – roller type boundary. Assuming both ends to be thus supported yields:

$$\begin{aligned}
w(x) &= \frac{A_{11}^* B_{11} - B_{11}^* A_{11}}{2 (B_{11}^2 - A_{11} D_{11})} \{L x - x^2\} \\
u(x) &= \frac{B_{11}^* B_{11} - A_{11}^* D_{11}}{(B_{11}^2 - A_{11} D_{11})} x.
\end{aligned}
\tag{4.47}$$

Example Section

Sample problems based on the theories presented in this chapter are presented here to illustrate the methods employed on real problems. The energy method in Section 4.4 presents an elegant method to describe and solve multilayer beam problems. Section 4.5.1 presents the solution of a Bimorph under excitation and mechanical load. Section 4.5.2 presents the solution methods for the Pin-Force, Enhanced Pin-Force and Euler-Bernoulli models. Several geometrical configurations are presented.

Energy Method

To illustrate the solution method encountered with the energy method, a simply supported and a cantilevered Bimorph actuator are addressed.

Simply Supported Bimorph

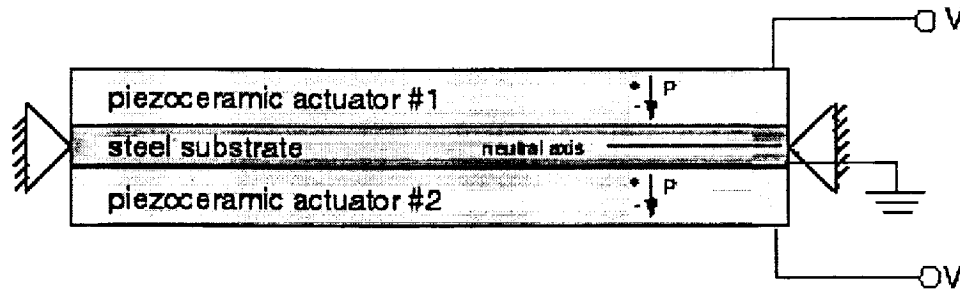


Figure 4.13. Simply supported Bimorph.

The Bimorph's dimensions and material constants are:

$L = 3$ inch, $t_{a,1} = t_{a,2} = 0.010$ inch, $t_b = 0.005$ inch, $Y_a = 10.15$ Msi, $Y_b = 30.46$ Msi, $E_{3,1} = 30$ kV/inch, and $d_{31} = 1.063 (10)^{-8}$ inch/volt.

Assuming small deflections, the governing equation and the boundary conditions for the Bimorph are:

$$\frac{d^2}{dx^2} \left(D_{11} \frac{d^2 w}{dx^2} \right) = 0
\tag{4.48}$$

$$D_{11} \frac{d^2 w}{dx^2} - Y_a t_a (t_a + t_b) d_{31} E_{3,1} = 0 \text{ at } x = 0, L \quad (4.49)$$

$$w = 0 \text{ at } x = 0, L.$$

The governing equation is integrated three times to get the displacement equation form:

$$w(x) = A_1 + A_2 x + A_3 x^2 + A_4 x^3 \quad (4.50)$$

Application of the boundary conditions results in the determination of the constants and the final form of the displacement equation:

$$w(x) = \frac{Y_a t_a (t_a + t_b) d_{31} E_{3,1}}{2 D_{11}} (x^2 - Lx) \quad (4.51)$$

Using the definition of D_{11} as:

$$D_{11} = \sum_{k=1}^n \left[\int_{h_k}^{h_{k+1}} Y_k z^2 dz \right], \quad (4.52)$$

the stiffness constant is calculated to be: 13.4277 lb inch.

Substituting the material constant values into the equation results in:

$$w(x) = 0.05424 x - 0.01808 x^2 \quad (4.53)$$

The displacement along the length can be calculated and plotted as:

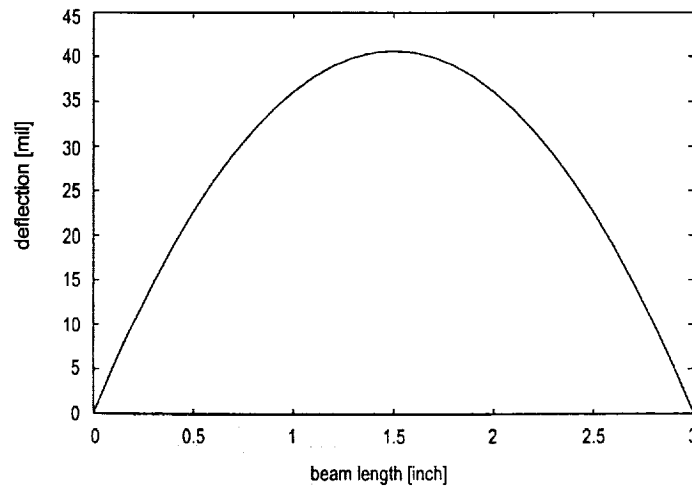


Figure 4.14. Displacement curve of the simply supported Bimorph.

Cantilever Bimorph with an End Load

The configuration shown in Figure 4.15 is solved in this example.

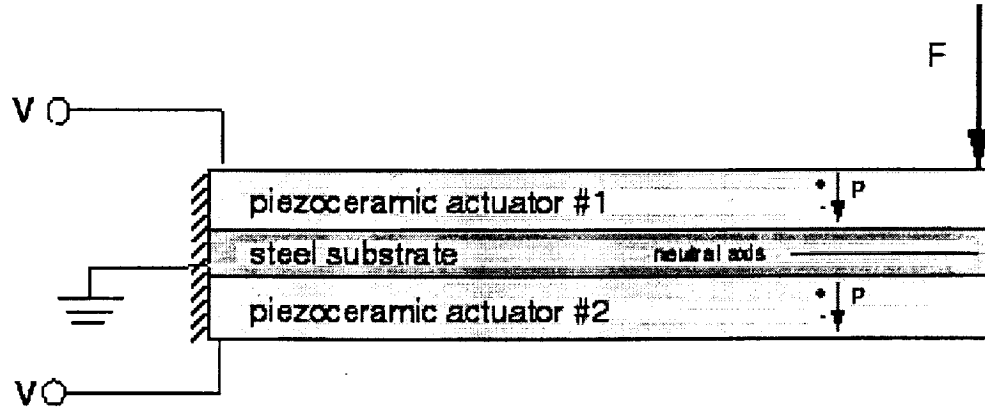


Figure 4.15. Cantilever Bimorph with an end load.

$L = 3$ inch, $t_{a,1} = t_{a,2} = 0.010$ inch, $t_b = 0.005$ inch, $E_a = 10.15$ Msi, $E_b = 30.46$ Msi, $E_{3,1} = 30$ kV/inch, $d_{31} = 1.063 (10)^{-8}$ inch/volt and $F = 0.25$ lbf.

The variational approach as presented needs one additional term to properly account for the end load. The potential energy for the load is:

$$\Pi_{load} = - F w|_{x=L} \quad (4.46)$$

The variation that must be added to the formulation presented in Equation (Error! Reference source not found.) is:

$$\delta \Pi_{load} = - F \delta w|_{x=L} \quad (4.47)$$

The total variation is now:

$$\begin{aligned} \delta \Pi = & b \left(D_{11} \frac{d^2 w}{dx^2} - E_a t_a (t_a + t_b) d_{31} E_{3,1} \right) \delta \left(\frac{dw}{dx} \right)_{x=0}^L \\ & - b \frac{d}{dx} \left(D_{11} \frac{d^2 w}{dx^2} \right) \delta w|_{x=0}^L \\ & + b \int_0^L \left\{ \frac{d^2}{dx^2} \left(D_{11} \frac{d^2 w}{dx^2} \right) \delta w \right\} dx - F \delta w|_{x=L} = 0 \end{aligned} \quad (4.48)$$

The governing equation for the Bimorph is:

$$\frac{d^2}{dx^2} \left(D_{11} \frac{d^2 w}{dx^2} \right) = 0. \quad (4.49)$$

The boundary conditions are:

$$w = \frac{dw}{dx} = 0 \text{ at } x = 0$$

$$D_{11} \frac{d^2 w}{dx^2} - E_a t_a (t_a + t_b) d_{31} E_{3,1} = 0 \text{ at } x = L \quad (4.50)$$

$$\frac{d}{dx} \left(D_{11} \frac{d^2 w}{dx^2} \right) + F = 0 \text{ at } x = L.$$

The governing equation is integrated three times to get the displacement equation form:

$$w(x) = A_1 + A_2 x + A_3 x^2 + A_4 x^3 \quad (4.51)$$

Application of the boundary conditions results in the determination of the constants and the final form of the displacement equation as:

$$w(x) = \frac{E_a t_a (t_a + t_b) d_{31} E_{3,1} + F L}{2 D_{11}} x^2 - \frac{F}{6 D_{11}} x^3 \quad (4.52)$$

The displacement as a function of the beam length is plotted for the conditions and material constants specified above.

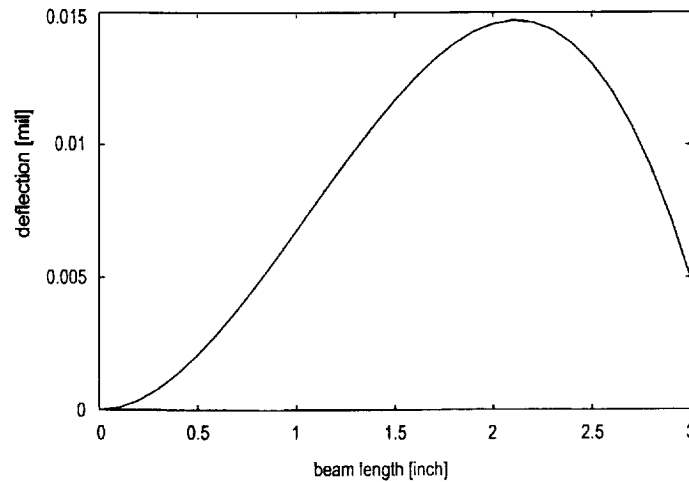


Figure 4.16. Displacement curve of the Cantilever Bimorph with an end load.

Classical Beam Theory

In this section, the Pin-Force, Enhanced Pin-Force and Euler-Bernoulli models are used with the classical beam theory solutions to present results for several geometric configurations. The geometric and material parameters shown below are used for all cases.

Geometry and Material Parameters

Unless otherwise specified, the following parameters are used in the calculations:

$l = 26.035$; length of the beam in [mm]

$b = 25.4$; beam-width (actuator-width) in [mm]

actuator-part:

$E_3 = 30000./0.0254$; electric field [V/m]

$d_{31} = -270.00e-12$; piezoelectric constant [m/V = C/N]

$t_a = 0.3048$; actuator-thickness in [mm] if one actuator is attached

$t_a = 0.1524$; actuator-thickness in [mm] if two actuators are attached
 $E_a = 70000$; Young's modulus of the piezoceramic in [N/mm²]
 $l_a = l$; actuator length for case 1
 actuator length in case 2:
 $a = 24.13$ [mm]
 actuator area in case 3:
 $b_1 \leq x \leq b_2$;
 $b_1 = 1.905$; [mm]
 $b_2 = 21.2725$; [mm]
 beam-part:
 $t_b = 0.1778$; thickness of the beam in [mm]
 $E_b = 210000$; Young's modulus of steel in [N/mm²]

Case 1

Case 1: Piezoceramic covering the whole beam length, as shown in Figure IV.4.

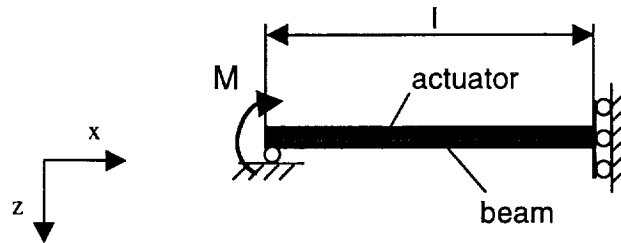


Figure IV.4. Piezoceramic over the whole beam length.

The stiffness of beam and piezoceramic is:

$$EI = (EI)_a + (EI)_b. \quad (4.53)$$

Assuming small deflections, the curvature κ is equal to w'' thereby yielding:

$$-EI w'' = M. \quad (4.54)$$

Integration over the length yields the governing equation for deflection:

$$-EI w = \frac{1}{2} M x^2 + C_1 x + C_2. \quad (4.55)$$

The boundary conditions, $w(x=0)=0$, and $w'(x=l)=0$, allow determination of the coefficients C_1 and C_2 . The final form of the deflection equation is:

$$w = \frac{M}{2EI} (2lx - x^2). \quad (4.56)$$

Table 4.1 shows the acting moment, the stiffness of the structure and the deflection at $(x=l)$ for the Pin-Force, Enhanced Pin-Force and Euler-Bernoulli bending models. It should be noted again that the moment M and the stiffness EI vary significantly with the models and the enforced assumptions. These effects on the predicted displacement from Equation 4.56 are significant. These comparisons are included to show the extreme over-prediction of the resulting deflection by the simplified Pin-Force and Enhanced Pin-Force models.

	Model:	Pin-Force	Enhanced Pin-Force	Euler Bernoulli
acting moment	M [Nmm]	- 5.66	- 9.37	- 26.54
bending stiffness	E [Nmm ²]	2498.43	6694.04	26774.2
deflection	w (l) [mm]	0.77	0.47	0.33

Table 4.1. Result overview of Case 1.

Case 2

Case 2: Piezoceramic covering the right side of the beam, as shown in Figure 4.18.

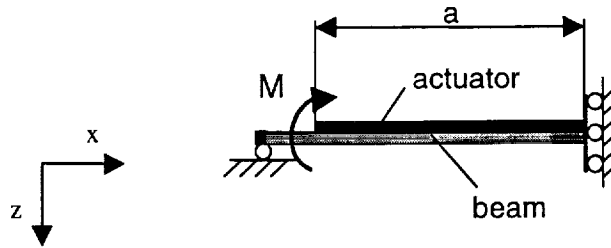


Figure 4.18. Piezoceramic located on the right side of the beam.

To solve this problem, the two distinctly different regions of the structure must be addressed with separate governing equations.

Section 1: $0 \leq x \leq (l-a)$

Denoting the section of the structure containing only the beam as section 1 (denote with subscript 1) the stiffness governing equation is:

$$-(EI)_1 w_1'' = 0. \quad (4.57)$$

One integration yields the slope w_1' :

$$-(EI)_1 w_1' = C_1, \quad (4.58)$$

and a second integration yields the deflection w_1 :

$$-(EI)_1 w_1 = C_1 x + C_2. \quad (4.59)$$

Section 2: $(l-a) \leq x \leq l$

Denoting the section of the structure containing the beam and the piezoceramic as section 2 (denote with subscript 2), the governing equation is:

$$-(EI)_2 w_2'' = M. \quad (4.60)$$

One integration yields the slope w_2' :

$$-(EI)_2 w_2' = Mx + C_3, \quad (4.61)$$

A second integration yields the deflection w_2 :

$$-(EI)_2 w_2 = \frac{1}{2} Mx^2 + C_3 x + C_4. \quad (4.62)$$

The boundary conditions $w_1(x=0)=0$, and $w_2'(x=l)=0$ are used to determine the coefficients C_2 and C_3 . To determine the coefficients C_1 and C_4 continuity and matching conditions are required. The conditions are $w_1(x=l-a)=w_2(x=l-a)$, and $w_1'(x=l-a)=w_2'(x=l-a)$. Because our interest is on the maximum deflection, which occurs at $x=l$, only the results for w_2 and w_2' are shown below. The slope w_2' is determined as:

$$w_2' = \frac{M}{(EI)_2} (l-x), \quad (4.63)$$

and the deflection w_2 is found to be:

$$w_2 = \frac{M}{2(EI)_2} (2lx - x^2 - (l-a)^2). \quad (4.64)$$

Table 4.2 shows the deflection results at $x=l$ as predicted by Equation (4.64) for the Pin-Force, Enhanced Pin-Force and Euler-Bernoulli models.

Model:	Pin-Force	Enhanced Pin-Force	Euler Bernoulli
deflection w_2 [mm]	0.76	0.47	0.33

Table 4.2. Results overview Case 2.

It should be noted that the quantities calculated for M and EI in example 1 are identical to the M and $(EI)_2$ used in case 2 on a model-by-model basis. Again note that M and EI are very specific to the model and the enforced assumptions.

Case 3

Case 3: Piezoceramic located at the center of the beam as shown in Figure 4.19.

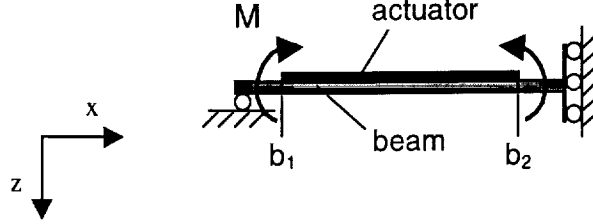


Figure 4.19. Piezoceramic located at the center of the beam.

The solution to this configuration is arrived at following the pattern of example case 2. The structure must be partitioned into three parts according to the stiffness changes along the length.

Section 1: $0 \leq x \leq b_1$

Denoting the beam only section on the left end (at $x = 0$) as section 1, the governing equation take the form:

$$-(EI)_1 w_1'' = 0. \quad (4.65)$$

Integration over the length yields the governing equation for deflection

$$-(EI)_1 w_1' = C_1, \quad (4.66)$$

and a second integration yields the displacement w_1 :

$$-(EI)_1 w_1 = C_1 x + C_2. \quad (4.67)$$

Section 2: $b_1 \leq x \leq b_2$

Denoting the section the beam covered with piezoceramics as section 2, the governing equations take the form:

$$-(EI)_2 w_2'' = M. \quad (4.68)$$

Integration over the length yields the displacement w_2 :

$$-(EI)_2 w_2 = \frac{1}{2} M x^2 + C_3 x + C_4. \quad (4.69)$$

Section 3: $b_2 \leq x \leq l$

The remaining beam section to the extreme right end is denoted as section 3 and the governing equation is:

$$(EI)_3 w_3'' = M - M = 0. \quad (4.70)$$

Integration yields the displacement w_3 :

$$-(EI)_3 w_3 = C_5 x + C_6. \quad (4.71)$$

The boundary conditions $w_1(x=0)=0$, and $w_3'(x=l)=0$ are used to determine the constants C_2 and C_5 . To determine the coefficients C_1 , C_3 , C_4 and C_6 , the continuity conditions between the three sections are required. The conditions are $w_1(x=b_1)=w_2(x=b_1)$, $w_2(x=b_2)=w_3(x=b_2)$, $w_1'(x=b_1)=w_2'(x=b_1)$, and $w_2'(x=b_2)=w_3'(x=b_2)$. Because the interest is on the maximum deflection, which occurs at $x=l$, only w_3 and w_3' are presented here. The slope in section 3 is:

$$w_3' = \text{const.} = 0 \quad (4.72)$$

and the deflection curve

$$w_3 = \text{const.} = \frac{M}{2(EI)_2} (b_2^2 - b_1^2). \quad (4.73)$$

Table 4.3 shows the deflection results at $x=l$ as predicted by Equation 4.73 for the for the Pin-Force, Enhanced Pin-Force and Euler-Bernoulli models. The acting moment M and stiffness EI_2 used in this example are the same as those used in example case 1.

It should be noted again that the assumptions made in modeling force significant changes to the moment M and stiffness EI .

Model	Pin-Force	Enhanced Pin-Force	Euler Bernoulli
deflection w_3 [mm]	0.51	0.31	0.22

Table 4.3: Results overview Case 3.

Predicted Results

A thorough examination of the theories examined in this document in terms of the predicted response of a variety of geometric configurations is presented in this section. A comparison of the Pin-Force, Enhanced Pin-Force and Euler-Bernoulli models, using the geometry and material parameters listed in Section 4.5.2, has been completed and is included in this section. Also the effects of piezoceramic to substrate thickness are investigated and the results are presented. Additionally a comparison between the Bimorph and Unimorph beam actuator based on the Euler-Bernoulli theory is shown. Finally the performance of an Unimorph beam is compared with a finite element model.

Comparison of Pin-Force, Enhanced Pin-Force and Euler-Bernoulli Models

In order to visualize the effects of the assumptions made in the Pin-Force, Enhanced Pin-Force and Euler-Bernoulli model development on the output performance, plots showing the performance characteristics of a Unimorph and a Bimorph beam are presented in this section.

Figure 4.20 shows two Unimorph geometrical configurations discussed in Case 1 of section 4.5.2. Because of symmetry only half of the beam actuator is modeled. At the left end of the Unimorph, the moment M which is induced by the strain in the piezoceramic acts on the structure. The right end of the structure shown in Figure 4.20 (a) indicates the center of the beam actuator, and is a guided boundary. Figure 4.20 (b) is a figure of one-half of a Unimorph

that is „blocked“ at the center. To calculate the blocking force of the actuator, the deflection and slope at the center are forced to be zero identically. This is modeled by a clamped center shown in Figure 4.20 (b). Bimorph structures with the same boundary conditions have been examined and are compared to the Unimorph structures in Figure 4.21.

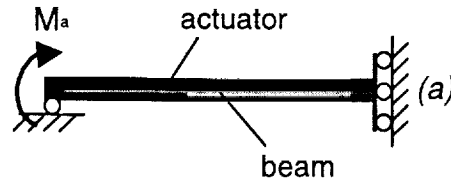
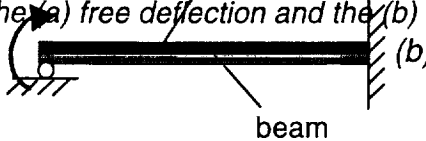
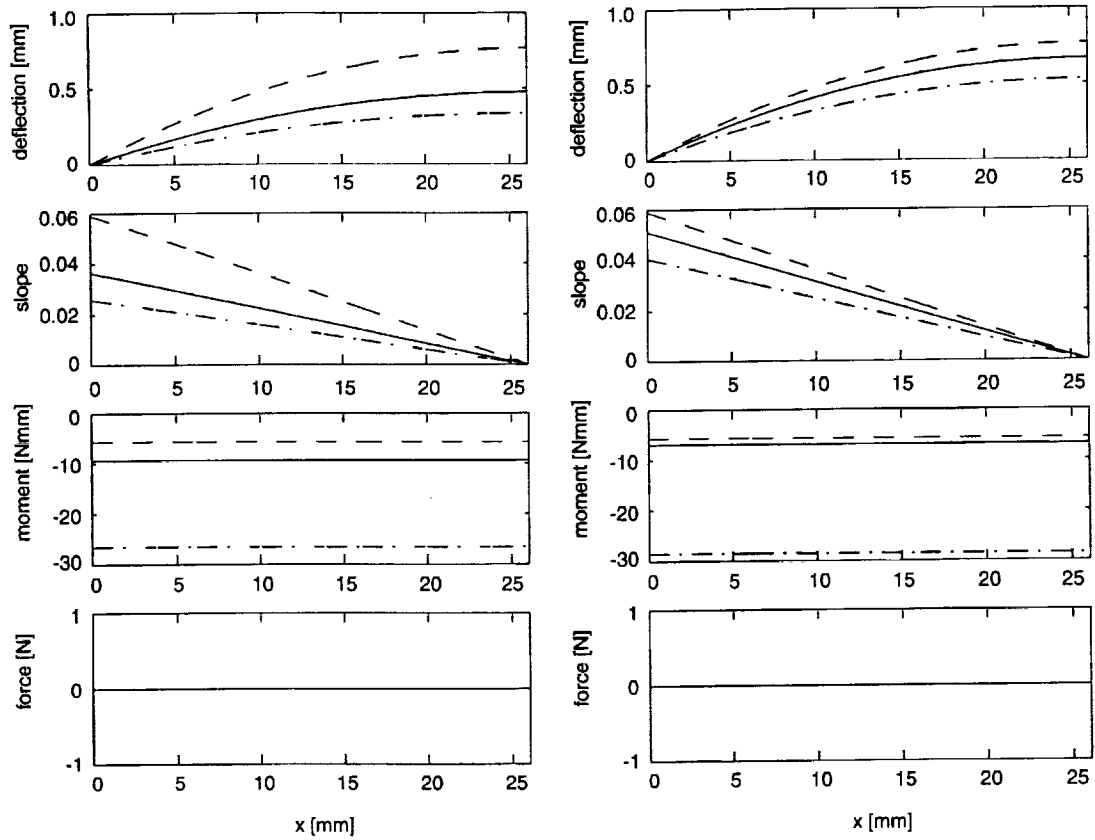


Figure 4.20. Boundary conditions on a Unimorph beam used to determine the (a) free deflection and the (b) blocking force.



Deflection, slope, moment and force over the beam length for the Unimorph (a) and Bimorph (b) are presented in Figure 4.21. These plots are based on the boundary conditions shown in Figure 4.20. To make the comparison between the Unimorph and Bimorph realistic, the total volume of piezoceramic material is constant. An electric field of 30 V/mil was applied to both the Unimorph and Bimorph structures.

- dash line Pin-Force Model,
- solid line Enhanced Pin-Force Model,
- dash-dot line Euler-Bernoulli Model.

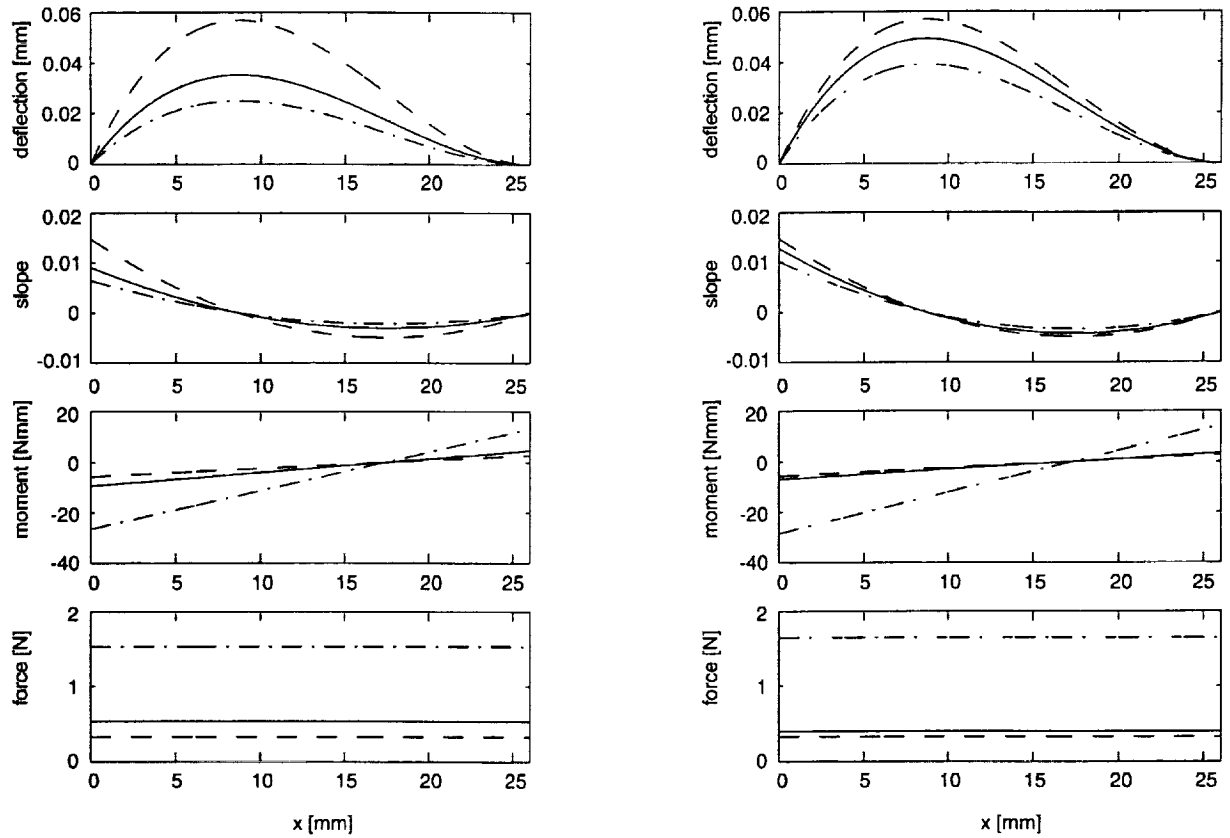


(a) Unimorph (b) Bimorph

Figure 4.21. Bending characteristics to determine the deflection.

The Pin-Force model predicts the highest deflection because of the low stiffness (resulting from the assumptions made in the model). The stiffness value does not change between models as the bending stiffness of the piezoceramics is neglected. The Euler-Bernoulli model predicts the lowest deflection due to the treatment of the bending stiffness of the piezoceramics in the model derivation. The Enhanced Pin-Force model shows that it is a good improvement of the Pin-Force model but still over-predicts the displacement field when compared to the Euler-Bernoulli model.

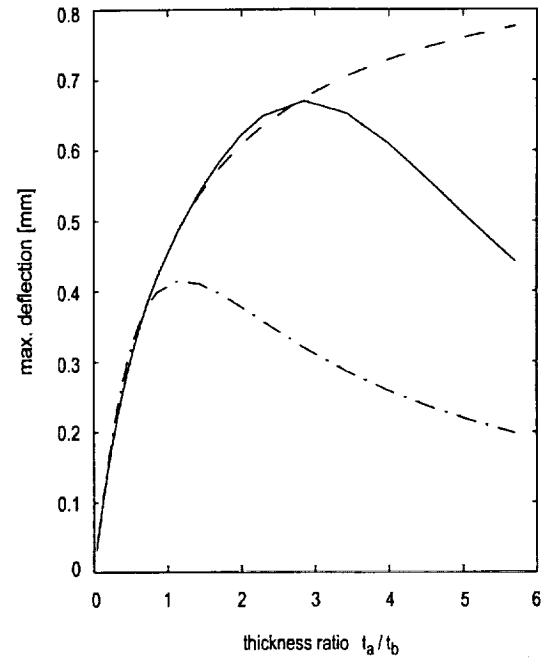
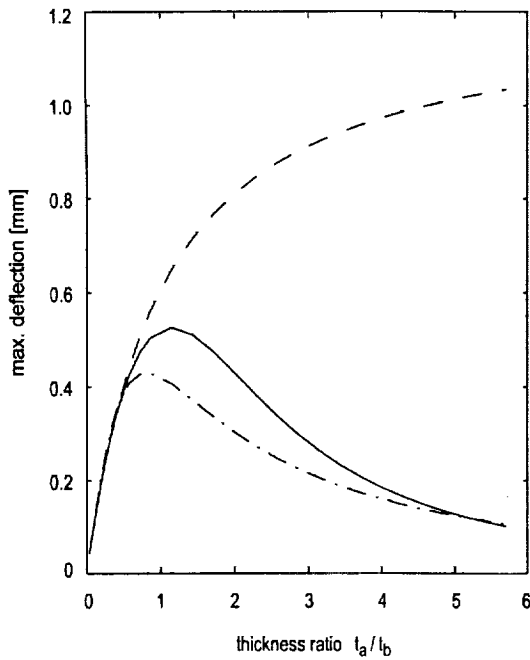
The blocking force comparison of the actuators is given in Figures 4.22 (a) and (b). The boundary conditions used in developing these plots is that shown in Figure 4.20 (b). The Euler-Bernoulli model predicts a blocking force three times larger Pin-Force models.



(a) Unimorph (b) Bimorph

Figure 4.22. Bending characteristics to determine the blocking force.

The results presented in Figures 4.21 and 4.22 are for a specific geometric configuration. The results presented in Figure 4.23 are based on a substrate thickness of 7 mil and a variable piezoceramic thickness in an effort to examine the effects of the thickness ratio on the output performance. The boundary conditions are exactly those presented in Figure 4.20 (a). The effective electric field applied to the Bimorph piezoceramic was reduced to a more realistic value as a 30 V/mil field will depole the ceramic with the poling axis opposite the applied field. is changed to a lower value. The fields used on the Bimorph ceramics were 15 and 30 V/mil, with the lesser field being applied to the ceramic with poling axis opposite the applied field. However, this field is still higher than recommended by most manufacturers.

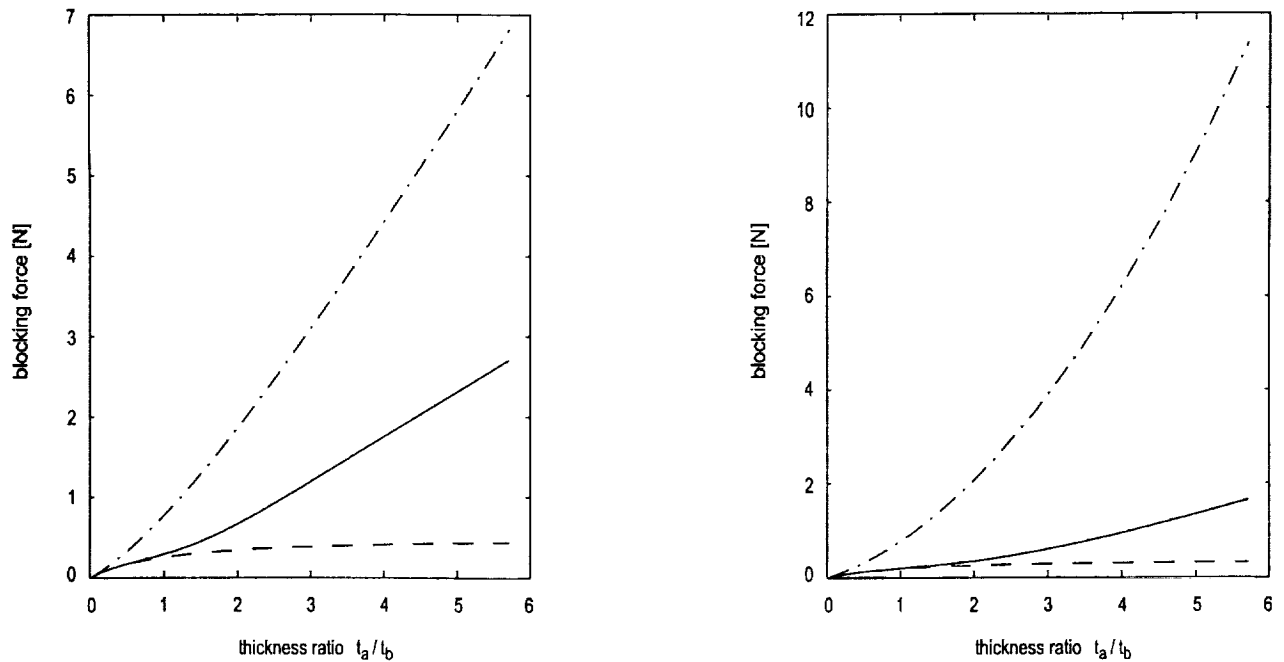


(a) Unimorph, field = 30 V/mil (b) Bimorph, effective field = 22.5 V/mil
(30 V/mil on one ceramic, 15 V/mil on the other)

Figure 4.23. Deflection vs. thickness ratio to find the optimum thickness ratio.

Comparison of the predicted deflections reveals that the Euler-Bernoulli and Enhanced Pin-Force models do show an "optimum" thickness ratio for the given materials. The Pin-Force model however does not predict an optimum because the bending stiffness of the piezoceramic is neglected in the model. The optimum thickness ratios for the Unimorph according to the Enhanced Pin-Force and Euler-Bernoulli models respectively are 1.14 and 0.86. The ratios for the Bimorph are 2.86 and 1.14 respectively. It should be noted that the Pin-Force model gives reasonable results up to a thickness ratio of approximately 0.7.

Figure 4.24 contains a comparison of the predicted blocking force as a function of the thickness ratios. The results are consistent with the assumptions made in the model derivations.



(a) Unimorph, effective field = 30 V/mil (b) Bimorph, effective field = 22.5 V/mil
(30 V/mil on one ceramic, 15 V/mil on the other)

Figure 4.24. Effect of the thickness ratio on the blocking force.

Tables 4.4 and 4.5 contain the results for the acting moment, maximum deflection and blocking force as predicted by the Pin-Force, Enhanced Pin-Force and Euler-Bernoulli models. The applied electric field for both Unimorph and Bimorph configurations was 30 V/mil. The values given in the tables for the blocking force are twice the force shown in the plots because to the symmetry used to develop the plots.

piezoceramic configuration		Pin-Force	Enh. Pin-Force	Euler-Bernoulli
	acting moment [Nmm]	- 5.6604	- 6.9602	- 28.5328
over the whole beam length	max. deflection [mm]	0.7678	0.665	0.5279
	blocking force [N]	- 0.6522	- 0.802	- 3.2878
on the right beam side	max. deflection [mm]	0.7637	0.6614	0.525
	blocking force [N]	- 0.6488	- 0.7978	- 3.2702
at the beam center	max. deflection [mm]	0.5085	0.4404	0.3496
	blocking force [N]	- 0.432	- 0.5312	- 2.1774

Table 4.4. Bimorph model results.

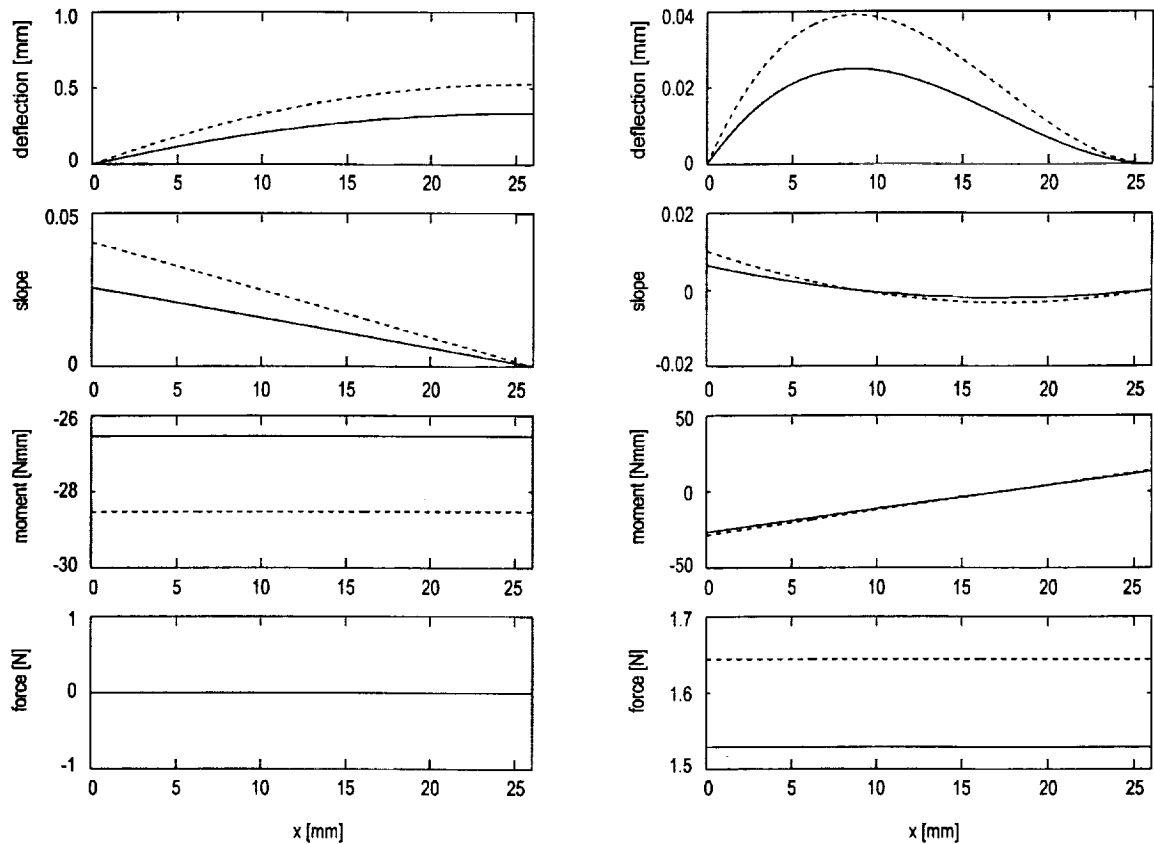
piezoceramic configuration		Pin-Force	Enh. Pin-Force	Euler-Bernoulli
over the whole beam length	acting moment [Nmm]	-5.6604	-9.3692	-26.5375
	max. deflection [mm]	0.7678	0.4743	0.3359
	blocking force [N]	-0.6522	-1.0796	-3.058
on the right beam side	max. deflection [mm]	0.7637	0.4718	0.3341
	blocking force [N]	-0.6488	-1.0738	-3.0416
at the beam center	max. deflection [mm]	0.5085	0.3141	0.2225
	blocking force [N]	-0.432	-0.715	-2.0252

Table 4.5. Unimorph model results.

Comparison of the Unimorph and Bimorph Structures

Often it is unclear whether a Bimorph or Unimorph structure will yield better force or deflection performance. In an effort to answer the question of superior performance, the Unimorph and Bimorph are compared via the Euler-Bernoulli model. Figure 4.25 contains the performance characteristics of a Bimorph (dotted line) and a Unimorph (solid line) for a free deflection condition and a blocked force condition. The geometry of the Unimorph and Bimorph structures used in this presentation are given in Section 4.5.2. The beam thickness is the same for both the Unimorph and the Bimorph. Also, the total volume of the piezoceramic is the same between the two structures. An electric field of 30 V/mil was applied to both the Unimorph and Bimorph. This field is not realistic for the Bimorph as one ceramic is always excited against the poling direction and will depole at this excitation level.

The plots in Figure 4.25 reveal that for the selected geometry, the Bimorph's performance exceeds that of the Unimorph in both deflection and blocking force. The only obstacle is however, constructing a Bimorph that will withstand this level of excitation. In the figure, the Bimorph is denoted with the dotted line and the Unimorph with the solid line.



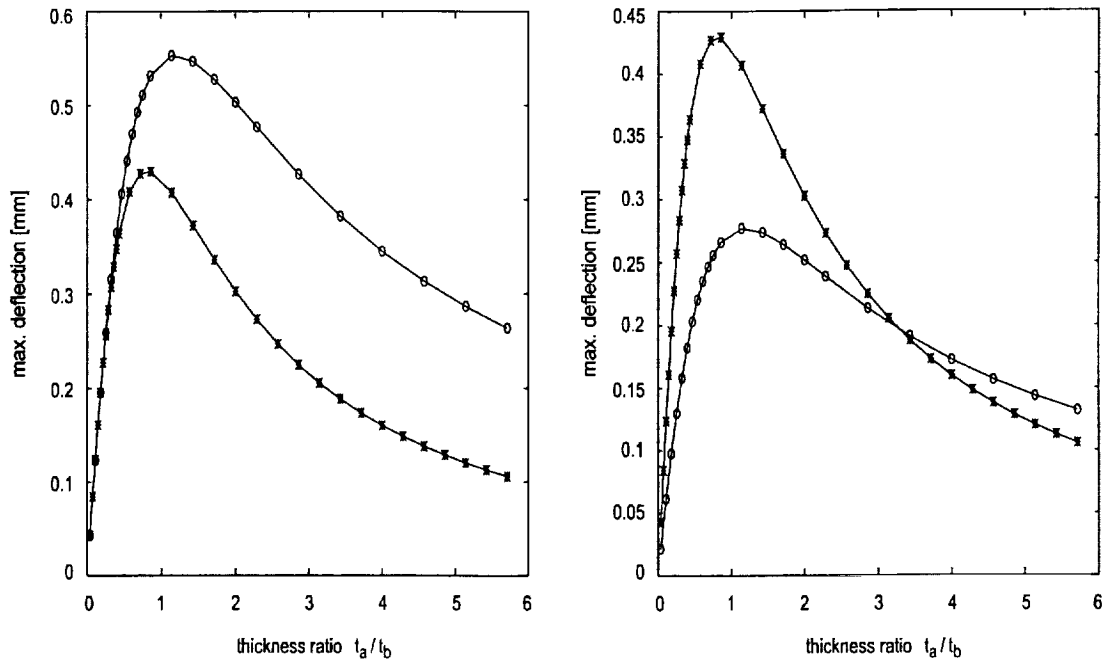
(a) Deflection (b) Blocking force

Figure 4.25. Bimorph - Unimorph comparison for the Euler-Bernoulli model. The Bimorph is denoted with the dotted line and the Unimorph with the solid line.

In order to learn more about the performance of the Bimorph and Unimorph as the piezoceramic to substrate thickness ratio is changed, numerous piezoceramic thickness values were analyzed with a common substrate thickness. Other geometry and material parameters as specified in Section 4.5.2 were used. Figure 4.26 (a) shows the deflection performance for a Bimorph (-o- line) and a Unimorph (-x- line) as a function of the thickness ratio for an applied electric field of 30 V/mil. Note again that this field is unrealistic for the Bimorph. The results show that the predicted deflection of the Bimorph exceeds the Unimorph deflection for all thickness ratios.

In an attempt to make a more realistic comparison, the excitation field applied to the Bimorph was reduced to 15 V/mil. This field is sufficiently high to depole some materials but is more realistic. The resulting deflection versus thickness ratio curves are given in Figure 4.26 (b). Note that the Unimorph curve is unchanged from Figure 4.26 (a). Also note that the Unimorph's predicted performance exceeds the Bimorph's performance for thickness ratios below 3.2.

- -o- Bimorph model,
- -x- Unimorph model.



(a) Unimorph: 30 V/mil, Bimorph: 30 V/mil (b) Unimorph: 30 V/mil, Bimorph: 15 V/mil

Figure 4.26. Deflection vs. thickness ratio to compare Unimorph and Bimorph. The Bimorph is denoted with the dotted line and the Unimorph with the solid line.

If two power supplies can be used to drive a Bimorph to enable the piezoceramics to individually be driven to their respective limits, the performance of the device can be increased somewhat. Using a field of 30 V/mil on one ceramic and a field of 15 V/mil on the other (in a direction opposite the poling axis), the performance differences between the Bimorph and the Unimorph decrease. Figure 4.27 shows the predicted deflection of these devices as a function of the thickness ratio.

FEM-Comparison

The comparison between a finite element model for composite beams and the analytical calculation was done for several cases of a bending beam (see Table **Error! Reference source not found.**). The FE-Model is 2 dimensional and has 32 square elements. Each element has 20 nodes (40 DOF) and the LaGrange shape function (C^0 continuity) is used. The material constants for this comparison are:

$$\begin{aligned}
 E_3 &= 15000/0.0254 \quad [\text{V/m}] \\
 d_{31} &= -270.00\text{e-}12 \quad [\text{m/V}] \\
 E_a &= 70000 \quad [\text{N/mm}^2] \\
 t_a &= 1.0 \quad [\text{mm}] \\
 E_b &= 210000 \quad [\text{N/mm}^2] \\
 t_b &= 1.5 \quad [\text{mm}] \\
 b &= 25.4 \quad [\text{mm}] \\
 l &= 100 \quad [\text{mm}] \\
 F &= -20 \quad [\text{N}]
 \end{aligned}$$

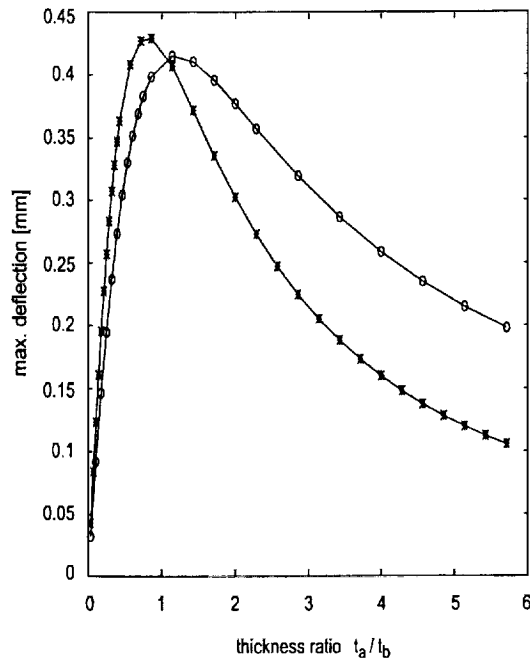


Figure 4.27. —x— Unimorph: 30 V/mil,
—o— Bimorph: + 30 V/mil, -15 V/mil.

The deflections at the center of the beam as predicted by the finite element model and the Euler Bernoulli model are reported in Table 4.6 for a bare steel beam, a Unimorph and a Bimorph. The finite element model correlates very well with the Euler-Bernoulli model.

	FEM	Euler- Bernoulli	notes
e 1 cas	0.27856 mm	0.2771 mm	steel beam, transverse force in the beam center
e 2 cas	0.106421 mm	0.1063 mm	Unimorph beam, transverse force in the center, $\Delta V = 0$ (no excitation)
e 3 cas	0.09239 mm	0.0924 mm	Transverse deflection induced by applied strain (applied Δ Voltage)
e 4 cas	0.36962 mm	0.3697 mm	maximum induced displacement, Figure 4 (a)

Table 4.6. Comparison between FEM and Euler-Bernoulli models.

V. Design of a MIMO Plate Control Testbed

Introduction

Intelligent structures are characterized by sensors and actuators which can be networked through a control system to produce robust control which can withstand or adapt to variations in controlled plant responses, environmental disturbances, and control system failures. Since there are typically a large number of inputs and outputs, it is beneficial and desirable to have compact sensors and actuators which are simple to use and do not greatly affect the open-loop response of a structure. Recent studies have shown piezoelectric materials are effective compact actuators and sensors.

We will discuss the design of a MIMO (multi-input/multi-output) plate control testbed. A simply-supported plate was chosen as the testbed structure for medium complexity and well defined behavior. This structure can be used as a development and standard comparison site for Active Vibration Control (AVC) and Active Structural Acoustic Control (ASAC).

The sixteen piezoelectric sensors and five piezoelectric actuators, chosen for both their size and effectiveness, are arranged on the plate to control the first five vibration modes. At present the controller software is limited to a sample speeds of ~2000Hz. For the simply supported testbed this limits control to the first five modes (less than 200Hz). The sensors have been configured to measure plate positions necessitating the design of signal conditioning amplifiers due to the sensors low voltage output and high impedance ($80M\Omega$) within the operating frequency range. The term *position* refers to plate positions in general, while specific types of positions will be expressly stated, e.g. modal positions. The resulting sixteen channel custom design implements a band-pass filter to eliminate low frequency variations and high frequency noise using a two stage operational amplifier (op-amp) configuration.

Modeling

The method used to characterize the piezo/structure interaction follows the method outlined in Hagood et al. (1990). The model they developed adapts well to multi-dimensional structures.

They arrived at two equations which describe the electromechanical interaction of the piezoelectric/structure system.

$$M\ddot{r} + K\dot{r} = B_f f + \Theta v \quad (\text{Actuator Equation})$$

$$\Theta^T r + C_p v = B_q q \quad (\text{Sensor Equation})$$

where M , C , K are mass damping and stiffness matrices respectively, Θ is the electromechanical coupling matrix, C_p is the piezoelectric capacitance matrix, B_f , B_q are the mechanical and electrical forcing matrices and r , v , q , f are the generalized coordinate, piezoelectric voltage, piezoelectric charge and applied point forces respectively.

We assume we have an ideal simply supported plate, with mode shapes given by the following wave equation:

$$\Psi_{ri}(x, y) = \sin(k_{xi}x) \sin(k_{yi}y)$$

$$k_{xi} = \frac{m_i\pi}{a} \quad (a \text{ is the plate length in meters - x direction})$$

$$k_{yi} = \frac{n_i\pi}{b} \quad (b \text{ is the plate length in meters - y direction})$$

The first five modes are ordered as follows:

The actuators and sensors used on the MIMO plate testbed are small compared to modal wave lengths for the first five modes. The actuators are (30.48×25.40) mm and the sensors are (25.40×27.94) mm.

Assuming a Bernoulli-Euler model, it has been shown that the effectiveness of the piezoelectrics should increase as the wave number increases.

It is important to realize that a piezoelectric is more effective on the higher modes. The response of a piezoelectric to the lower modes could be improved by covering more area of the plate, but while this will help the response to the lower modes it introduces spatial aliasing.

In order to maximize a piezoelectric's effectiveness for a particular mode, given the piezoelectric size, the center location of the piezoelectric should be chosen such that

$$x_0 = \frac{\pi}{2k_x} = \frac{\lambda_x}{4}$$

$$y_0 = \frac{\pi}{2k_y} = \frac{\lambda_y}{4}$$

that is, placed on an antinode for the mode. The actuators were placed in the antinodes of the first five modes.

We can consider each piezoelectric to act electrically independent. That is, the charge/voltage combination on a given piezoelectric is a direct function of the modal position only and not of charge/voltage combinations on other piezoelectrics. This might not necessarily be the case for a complicated electrode arrangement where electrodes on the top and bottom of a piezoelectric may overlap.

At this point expressions for the control system electronics can be included. The electronics couples dynamically through the piezoelectric voltage and charge, v and q . Hagood et al. (1990) discuss, in general terms, how to incorporate electronics into a state-space representation of the piezosystem. Much effort was used in the design of the MIMO plate control testbed to insure that the sensor and actuator electronics would be simple to model and integrate well with the piezostructure.

Piezo-electronics design

Various actuator power amplification methods for the actuators were considered, among them high voltage analog amplifiers and pulse-width modulation. The voltage amplification scheme chosen uses low gain amplifiers ($\sim 2.5V/V$) in series with a transformer (24:1) to deliver the relatively high voltages (up to 150V) to the actuators. This avenue was chosen over more elegant and expensive methods because its dynamics could be easily modeled and included in the mathematical models required to generate control laws. In addition, the amplifier-transformer pairs could be constructed with relative ease and short lead time. Low-pass smoothing filters (200Hz cutoff) were added to reduce the high frequency content of the zero-order-held control signal coming from the computer and are also included in the system models.

Let's exam in detail now what the methods are for regulating voltage-driven actuators and measuring sensor voltage correlated to modal positions.

Actuator Amplifiers and Smoothing Filters

The actuator equation shows that, for voltage-driven actuators, the force input is proportional to the patch voltage and that the current does not influence modal forces. Current will flow to or from a patch depending upon the modal velocities. The flow of current either with or against the forcing voltage is analogous to deflections either with or against a point force resulting in energy flow to or from the structure.

Piezoelectric actuators typically require large voltages and relatively small currents. Several techniques for providing a control voltage were considered, among them: High voltage analog amplifiers, pulse width modulated amplifiers. Due primarily to the high cost of voltage, amplifiers were eliminated. It was unknown how pulse width modulated amplifiers would affect a piezostructure and were also disregarded. The voltage amplification scheme chosen for the MIMO testbed is a power amplifier in series with an audio transformer (see figure 1). Audio transformers were chosen since they have flat frequency responses over a large bandwidth (2-20,000 Hz). The power amplifier is needed since most D/A boards do not provide sufficient power. The transformer steps up the control voltage as necessary. Admittedly, the current on the patch side of the transformer is low but this is satisfactory since piezoelectrics are low power actuators. The fact that the transformers do not transfer DC voltages is of little

concern since we are dealing with harmonic and narrowband sinusoidal disturbances.

The effective amplifier gain is the voltage amplifier gain multiplied by the turns ratio of the transformer.

$$V_{out} = aKV_{in}$$

The transformer selected has a turns ratio $a \approx 24:1$ and the voltage amplifier has a gain of $K \approx 2.5V/V$.

To reduce the effect of the staircased nature of the control signal output from the D/A board on higher modes of the plate, the control signal is filtered using a single pole passive low pass filter (see figure 1) with transfer function

$$\frac{V_{out}}{V_{in}} = \frac{1}{sRC + 1}$$

The smoothing filter pole was selected at 200 Hz. At present, the controller software runs at approximately 2000 Hz, allowing control of structural frequencies one decade below, at 200 Hz. The smoothing filter pole sufficiently attenuates the high frequency components of the staircased control signal.

Burst random testing of the smoothing filter-amplifier-transformer combination was performed. A curve fit of the data resulted in a transfer function

$$\frac{V_{out}}{V_{in}} = 0.514 \frac{(s/18.9 + 1)}{(s/38 + 1)(s/1260 + 1)}$$

Figure 2 shows the curve fit versus the measured data.

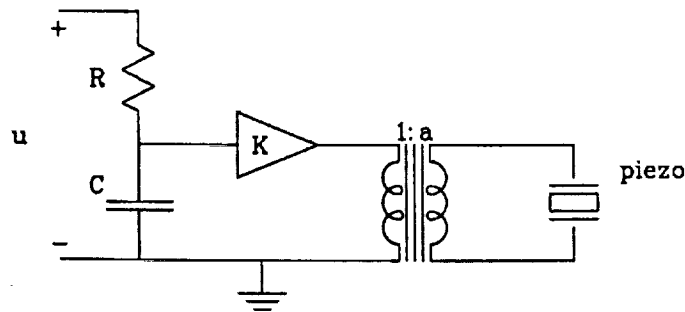


Figure 1: Filter-Amplifier-Transformer Diagram

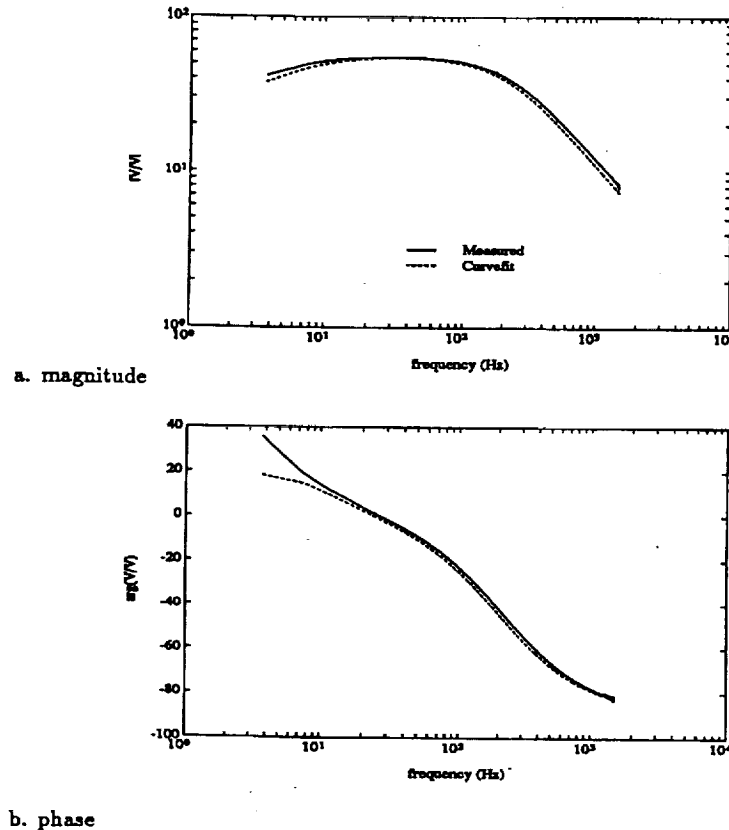


Figure 2: Curvefit and Experimental FRF's for Filter-Amplifier-Transformers

Sensor Design

It is possible to impose appropriate boundary conditions to piezoelectric sensors such that the voltage is a linear transformation of modal positions. This can be achieved by imposing an open circuit across the sensor patch electrodes. This forces the current, thus the charge, flowing from a patch to be zero.

In a practical sense it is difficult to impose real open circuits and still be able to measure the voltage of interest. Large impedances placed across electrodes can cause impedance mismatches with voltage measuring equipment and load the piezoelectric changing the quantity to be measured. Also conventional A/D boards do not measure the typically small voltages output by PVDF which fill only a few bits of information on the A/D board. Therefore it is desirable to amplify the signal.

Imposing the boundary condition and amplifying is possible using operational amplifiers (op-amps) by connecting the piezoelectric to a non-inverting amplifier (see figure 3). The infinite input impedance and zero input bias current of ideal op-amps satisfies the open-circuit boundary condition. In reality op-amps have finite input impedance and allow current to flow into the inputs of the op-amp. It is necessary to choose an op-amp with sufficiently large input impedance such that

the cutoff frequency ($1/(2\pi RC_p)$) for the resulting high-pass filter is as low as required. The gain of the non-inverting amplifier is selected as needed.

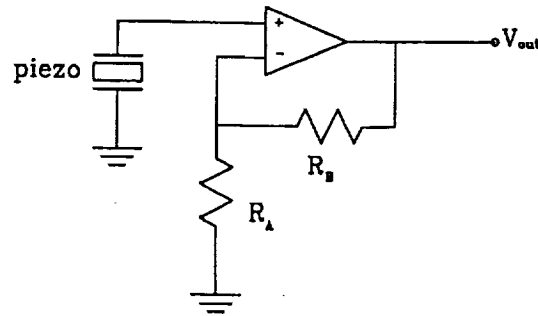


Figure 3: Non-inverting Amplifier Schematic

The PVDF sensors used on the plate test bed have small capacitances (2.5pF) with correspondingly large impedances over the frequency range of interest (40-250 Hz). This required the use of high input impedance JFET op-amps (Burr Brown OPA 602) to keep the cutoff frequency sufficiently low. Also the low bias currents provided by junction field-effect transistor (JFET) op-amps are a benefit. The non-inverting amplifier was designed to have a gain of 11V/V.

Experimentation showed that a low pass filter would also be required to eliminate high frequency noise. A single pole active low-pass filter was designed to have a cutoff at 40 Hz. The sensitivity of the PVDF sensors to very low frequency vibration necessitated the use of a high-pass filter in the signal conditioning amp. This was added as a second stage and follows a Sallen-Key design, see figure 4. The second stage was designed with a gain of 1.8V/V, making the overall amplifier gain 20V/V. The final sensor signal conditioning amplifier design is shown in figure 5. A frequency response of a sensor signal conditioning amplifier is shown in figure 6. The spikes in the frequency response of the signal conditioning amplifier are a result of noise at 60 Hz harmonics.

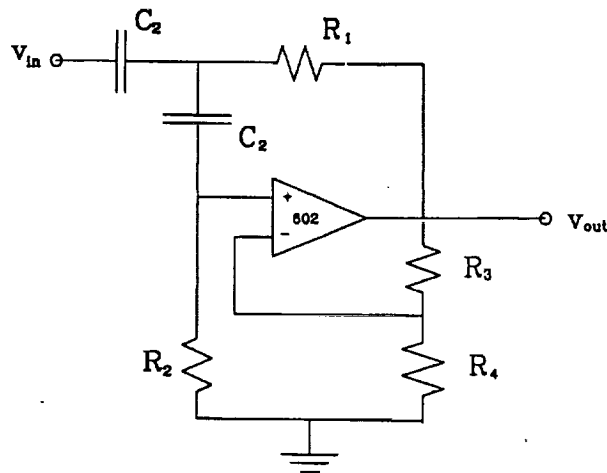


Figure 4: Sallen-Key High pass Filter Schematic

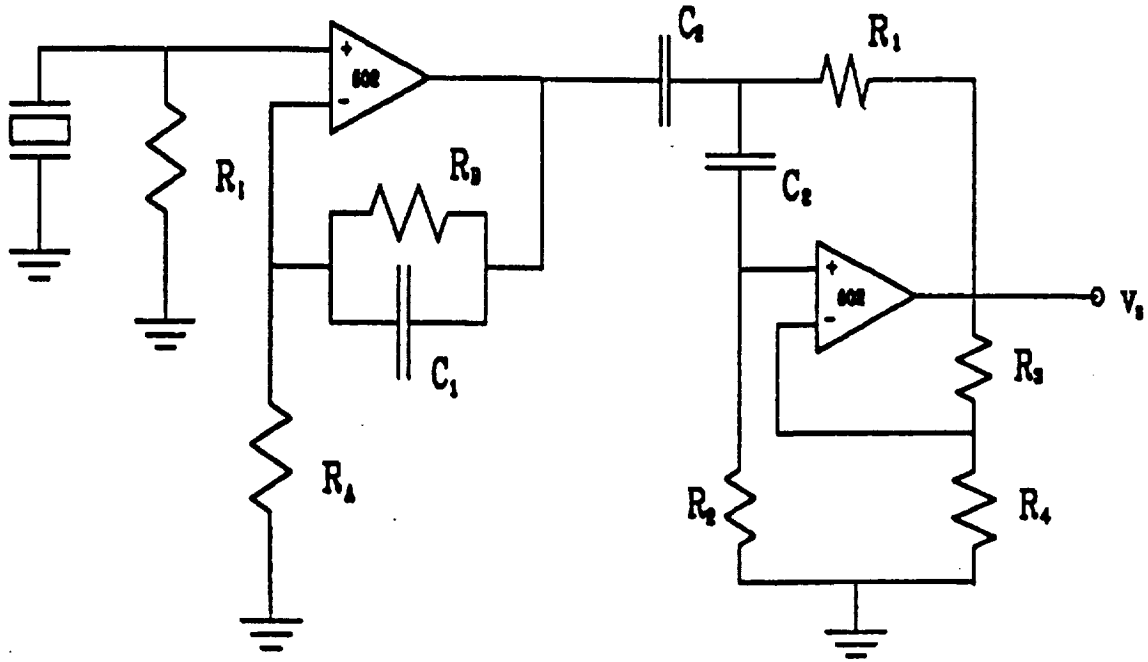
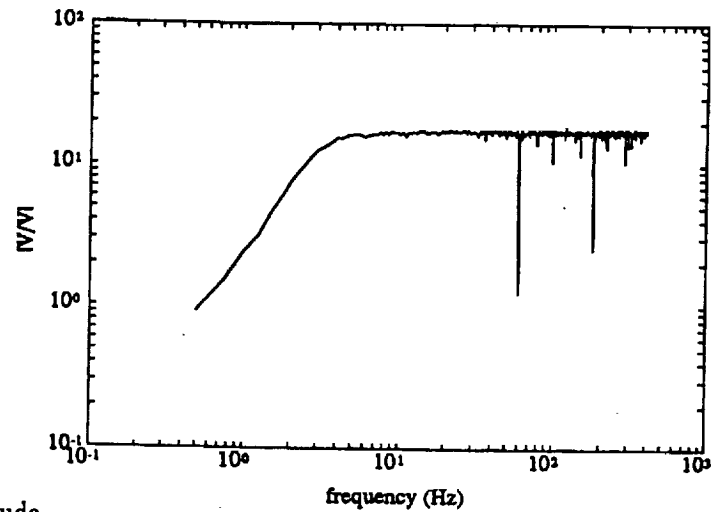


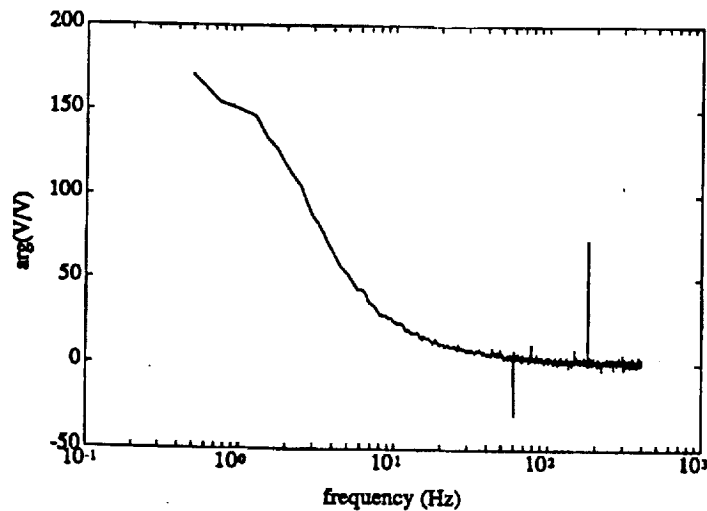
Figure 5: Signal Conditioning Amplifier Schematic

Table 1: Signal Conditioning Amplifier Component Values

R_A	1.00 k Ω
R_B	10.00 k Ω
R_I	22.00 M Ω (1-8)
	10.00 M Ω (9-16)
C_1	0.41 nF
C_2	0.57 μ F
R_1	100.00 k Ω
R_2	100.00 k Ω
R_3	220.00 k Ω
R_4	390.00 k Ω



a. magnitude



b. phase

Figure 6: FRF for Sensor Signal Conditioning Amp, Channel 5

Summary

The testbed constructed is an extension of a SIMO (single-input/multi-output) plate control testbed developed in the Smart Structures Lab at Virginia Polytechnic Institute and State University (Rubenstein 1991). While the SIMO plate used proven technology in shakers and accelerometers, the new MIMO testbed implements piezotechnology, taking advantage of piezoelectrics' compact size and weight.

An analytical model which represents the electromechanical interaction between the structure, piezoelectrics and electronics is developed (Hagood 1990) and used in the design of amplifiers for both piezoactuators and piezosensor signals.

A single pole passive smoothing filter was used to reduce the effect of the zero-order-held control signal. The smoothing filter was used in conjunction with

a voltage amplifier and transformer to provide the relatively high voltages required by piezo-electric actuators. Measured dynamics of the filter-amplifier-transformer (FAT) combinations was curvefit and the resulting transfer function can be used in the design of control laws for the plate. While the FAT's are simple to build, low frequency dynamics should be modeled. The low frequency pole and zero are thought to represent the transformer dynamics. Other amplification schemes, such as pulse width modulation, may only require modeling of designed smoothing filter and could draw less power, both benefits which may be necessary in large scale applications of this technology.

Sixteen PVDF sensors were conditioned to measure plate position. This required the design of high impedance signal conditioning amplifiers. It is also possible to measure plate velocities using current-to-voltage (I-V) amplifiers. The PVDF sensors used on the MIMO plate deliver small currents (less than 1 μA) which requires high gain I-V amplifiers which may be more subject to various sources of noise.

PZT sensors deliver ~25 times the voltage and ~250 times the current as PVDF sensors of similar area. Both of these properties indicate that PZT is a better transducer than PVDF. Recent studies have investigated the use of piezoelectric sensor/actuators which use a single piezoelectric element to provide measurement and control. There are also indications that sensor/actuators could be used effectively in system identification schemes to provide drive point responses.

VI. Electronics Design for Piezoelectric Systems

The purpose of this section is to introduce the engineer to aspects of electronics design which give piezoelectric actuators desirable properties. The first two topics show how to develop collocated actuator-sensor elements by exploiting the coupled electrical-mechanical fields within the piezoelectric material. The third topic explains how to tune power conditioning circuits to reduce the current requirements of piezoelectric materials. The final topic explains how to use piezoelectric elements as the active element in passive damping circuits.

A Self-Sensing Piezoelectric Actuator for Collocated Control

Introduction

The use of intelligent structures promises to allow space structures to better meet the two opposing design goals of minimizing weight and maximizing stability. Typically an intelligent structure will possess sensors to monitor the structure, actuators which are capable of changing the state of the structure, and some form of feedback control logic.

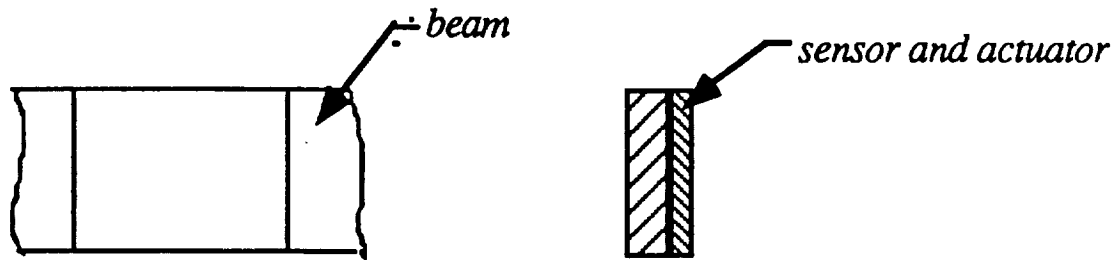
Recently, piezoelectric actuators have successfully controlled a variety of active structures. The primary advantage of piezoelectric actuators for these applications is that they convert electric potential to mechanical displacement in an efficient and direct manner. If the piezoelectric material is properly attached to a structure, the strain in the piezoelectric will create a strain in the structure. Such an actuator is lightweight, and will have a large bandwidth (in contrast to other actuators such as an electric motor whose usable bandwidth is affected by actuator dynamics such as motor inertia and inductance). Another advantage of piezoelectric actuators is the ability to produce static displacement (shape control). An example of shape control would be a smart wing which is capable of changing its geometry under certain flight conditions. A piezoelectric sensor is created by measuring the voltage produced across a piezoelectric material as it strains. Such a piezoelectric sensor will also be lightweight, simple, efficient, and have a large bandwidth.

We will describe a technique to combine into a single element the piezoelectric actuator and the piezoelectric sensor. Such an element can be called a self-sensing actuator and would have many applications. Combined with a power amplifier and feedback control algorithm the self-sensing actuator would form a complete control unit. The control unit (self-sensing actuator, power amplifier and control algorithm) could be applied directly to a structure, creating an *active structure* capable of reducing vibration or controlling the shape of the structure. The control unit could also form a building block in an intelligent structure. In an *intelligent structure* many such control units could be distributed throughout the structure, and coordinated by a centralized computer.

One of the primary motivations for using a collocated sensor/actuator is the stability of the controlled structure. It can be shown that in the absence of sensor and actuator dynamics, a structure controlled with a simple collocated negative velocity feedback law will be globally stable for all modes of the structure. This is in contrast to non-collocated velocity feedback laws which in general will not be stable for all modes of a structure.

Presentation of the Self-Sensing Actuator

The collocated control method developed here uses a single piezoelectric material and a single electrode area for both sensing and actuation (figure 1). One advantage of this scheme is that it is a true collocated sensor. The strain in the sensor must be the same as the strain in the actuator because they are the same device. Another more important feature is the method is completely general. It can be applied to any structures such as beams, trusses, or shafts using any shape piezoelectric actuator (such as rings, stacks and plates).



Self - Sensing Actuator Collocated Sensor and Actuator

Figure 1. Schematic showing a generic arrangement of structure and sensor/actuator.

The self-sensing piezoelectric actuator operation is based on the linear system principle that if two signals are added into a linear system and one of the signals is known, the second input can be determined. In this case, the two signals are the voltage from the controller and the voltage produced by piezoelectric material as it strains.

Implementation of Piezoelectric Actuators and Sensors

Techniques for implementing a simple strain sensor and rate of strain sensor are shown in this section. From these simple building blocks a technique is developed for implementing the self-sensing piezoelectric actuator. The technique can be applied to many structures including plates, shafts, and trusses.

Piezoelectric Strain Sensor

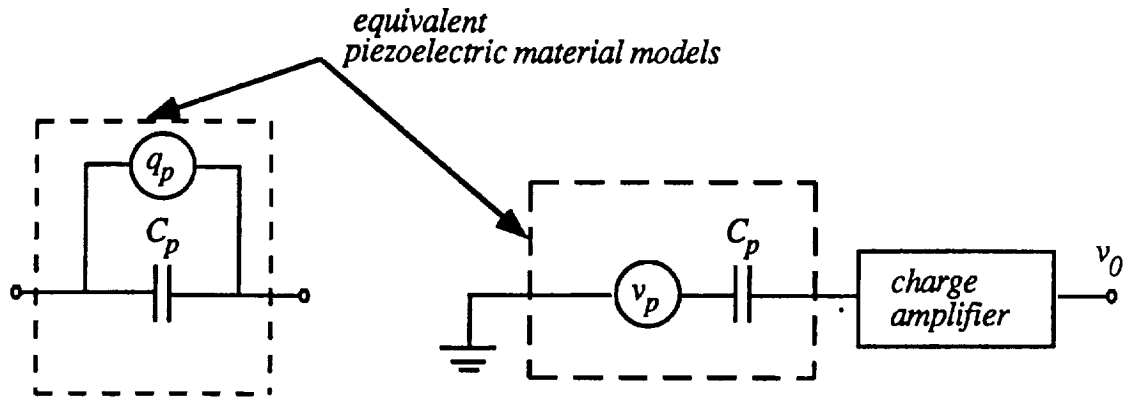
The piezoelectric material can be modeled as a charge generator in parallel with a capacitor (C_p). The capacitor accounts for the dielectric properties of the piezoelectric material and the charge generator accounts for piezoelectric (and pyroelectric, if significant) properties. The equivalent circuit of a parallel charge generator and capacitor is a voltage generator in series with a capacitor. A strain sensor can be made by connecting the piezoelectric material to a high impedance measuring device such as a charge generator (figure 2). In the figure, the output voltage v_o is equal to the voltage produced by the strain of the piezoelectric v_p . For a piezoelectric material bonded to a beam between points x_1 and x_2 as shown in figure 3, it can be shown that the voltage produced by the piezoelectric is:

$$v_o = K_s (y'(x_2) - y'(x_1))$$

$$v_o = v_p$$

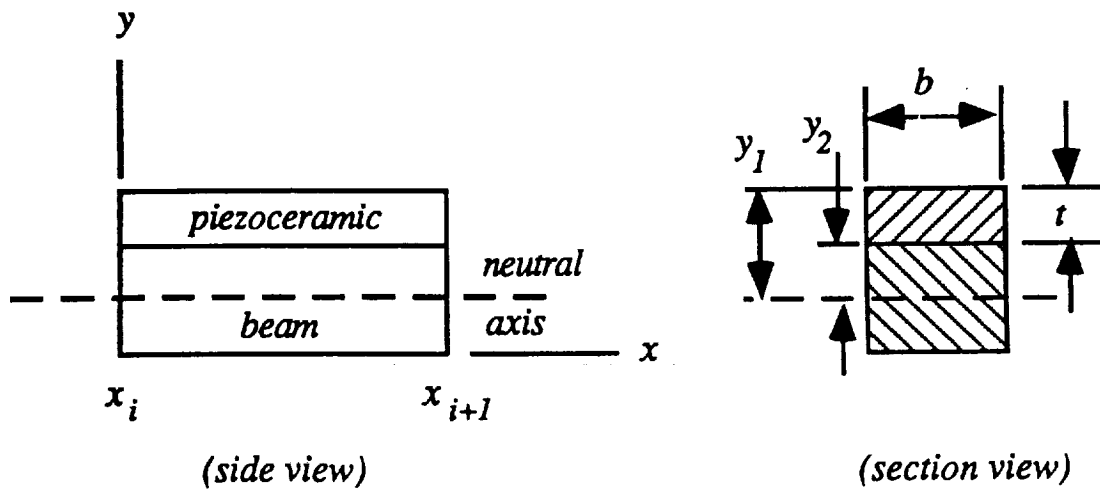
where K_s is the sensor constant of the piezoelectric element and y' is the slope of the beam.

The piezoelectric strain sensor is best suited to dynamic and quasi-static conditions. Small DC offsets to the charge amplifier and pyroelectric effects will create drift in the charge amplifier during static conditions. For static conditions the charge amplifier will tend to drift due to small DC offsets to the charge amplifier and pyroelectric effects. For static conditions it is better to use the familiar resistance strain gauge.



Equivalent Piezoelectric Models and Circuit For Measuring Strain

Figure 2. Equivalent Electrical Circuits for Piezoelectric Sensors



Piezoceramic Element Bonded to a Beam

Figure 3. Cross sectional and side system view

Piezoelectric Rate of Strain Sensor

A piezoelectric rate of strain sensor can be formed by adding resistor in series with the material (figure 4). The transfer function in the Laplace Domain for this circuit can be shown to be:

$$V_0 = \frac{RC_p s}{1 + RC_p s} V_p$$

For frequencies less than $1/RC_p$ the transfer function will behave like a pure differentiator. Thus for frequencies less than $1/RC_p$ the output will be equivalent to the time rate of strain:

$$v_0 = \frac{d}{dt}(v_p)$$

$$v_0 = K_s \frac{d}{dt}(y'(x_2) - y'(x_1))$$

where K_s is the sensor constant

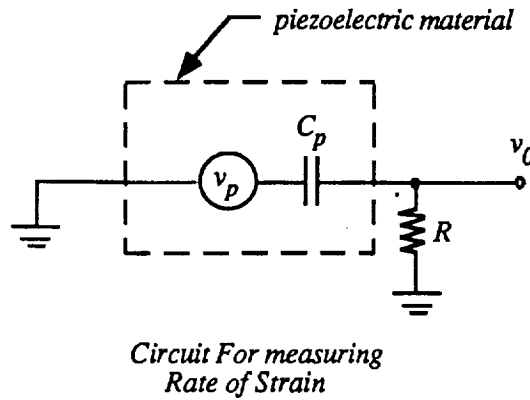


Figure 4

Self-Sensing Actuator

In the previous two sections it was shown how to implement a piezoelectric sensor. In this section the implementation of a combined piezoelectric sensor and actuator will be shown. The combined sensor actuator is based on the linear system principle that if two signals are added into a linear system, and the output and one of the inputs is known, the second input can be determined. The self-sensing actuator can be thought of as having two added inputs signals. One input voltage is from the controller and the other input voltage is due to the strain of the material (piezoelectric effect). By subtracting from the output voltage the effects due to the control voltage v_c , only the voltage due to the strain of the material remains in the output signal. Two methods of achieving this goal have been developed. One method produces a rate strain signal and the second method produces a strain signal. The choice of which method to use will depend upon the signal required for the control law.

Rate of Strain Sensing with the Self-Sensing Actuator

Sensor Dynamics

Rate of strain sensing is accomplished by putting an equivalent RC circuit in parallel to the RC circuit formed by the series resistor and piezoelectric material (see figure 5). The circuit output will be the sensor voltage v_s and the inputs will be the control voltage v_c and the piezoelectric voltage v_p . The transfer function for this circuit in the Laplace domain can be shown to be:

$$V_s = V_1 - V_2 = \frac{R_1 C_p s}{1 + R_1 C_p s} V_p + \left[\frac{R_1 C_p s}{1 + R_1 C_p s} - \frac{R_2 C_2 s}{1 + R_2 C_2 s} \right] V_c \quad (1)$$

If the two RC time constants are equivalent ($R_1 C_p = R_2 C_2$) then the circuit output equation becomes the same as the simple rate of strain sensor:

$$V_s = \frac{R_1 C_p s}{1 + R_1 C_p s} V_p \quad (2)$$

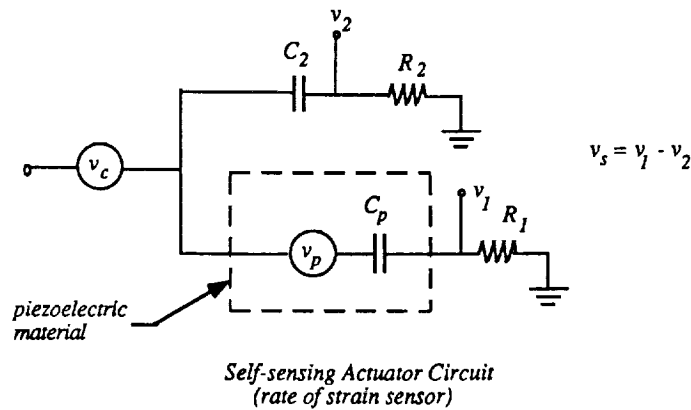


Figure 5

Actuator Dynamics

When using the material as an actuator the effect of the resistor in the circuit must be taken into account. The actuation voltage is no longer simply the control voltage. The moment generated by the piezoceramic is proportional to the voltage applied across it, which in figure 5 is $v_c - v_1$:

$$V_c - V_1 = \frac{1}{1 + R_1 C_p s} V_c - \frac{R_1 C_p s}{1 + R_1 C_p s} V_p \quad (3)$$

The last term in the above equation is the same as the sensor signal $V_1 - V_2$ in equation (2). Moving the last term to the left hand side of the equation results in an equation representing the actuator dynamics:

$$V_a = (V_c - V_1) + (V_1 - V_2) = V_c - V_2 = \frac{1}{1 + R_1 C_p s} V_c \quad (4)$$

Thus the actuator behaves like a low pass filter. For frequencies less than $1/R_1 C_p$ the actuator voltage will be equivalent to the control voltage. For frequencies above $1/R_1 C_p$ the control signal will be attenuated.

Strain-Sensing with the Self-Sensing Actuator

Sensor Dynamics

The self-sensing strain sensor operates on the same linear principle as the self-sensing rate of strain sensor. In the rate of strain sensor a resistor is added in series to create a differentiator. In the strain sensor a capacitor is added in series to create an AC voltage divider (see figure 6). The voltage follower circuit is required to create a high input impedance measuring device (about 80M ohms for the experimental circuit) and the resistor R is required to prevent drift of the output voltage. Again, the two inputs to the system are the control voltage and the piezoelectric voltage; the output will be the sensor voltage. For this circuit the transfer function can be found to be:

$$V_s = V_1 - V_2 = \frac{RC_p s}{1 + R(C_p + C_2)s} V_p + \left[\frac{RC_p s}{1 + R(C_p + C_2)s} - \frac{RC_3 s}{1 + R(C_3 + C_4)s} \right] V_c \quad (5)$$

When the two circuit have equivalent transfer functions, the term multiplying the control voltage will drop out of equation (5). The sensor transfer function equation then becomes:

$$V_s = V_1 - V_2 = \frac{RC_p s}{1 + R(C_p + C_2)s} V_p \quad (6)$$

For frequencies greater than $1/R(C_p + C_2)$ it simplifies to a frequency independent (does not involve s) equation:

$$V_s = V_1 - V_2 = \frac{C_p}{C_p + C_2} V_p \quad (7)$$

Thus for frequencies greater than $1/R(C_p+C_2)$ the sensor circuit behaves like an AC voltage divider. The resistor R is chosen so that the frequencies of interest are greater than $1/R(C_p+C_2)$. Therefore the circuit is best used for dynamic applications. For static applications (frequencies less than $1/R(C_p+C_2)$) the sensor dynamics as defined by the equation (6) will come into effect.

Actuator Dynamics

The actuation voltage that the piezoelectric actuator sees will be the difference in voltage across the piezoelectric material, which in the diagram is $v_c - v_1$. For a controller input v_c and a piezoelectric voltage v_p the actuation voltage for frequencies greater than $1/R(C_p+C_2)$ can be shown to be:

$$V_a = V_c - V_1 = \left[1 - \frac{C_p}{C_p + C_2} \right] V_c - \frac{C_p}{C_p + C_2} V_p \quad (8)$$

The capacitor C_2 is chosen to be much larger than the capacitance of the material C_p which will cause the term multiplying V_c to be roughly 1 and the term multiplying V_p to be roughly zero. For such an approximation the actuator will be equal to the control voltage: $V_a = V_c$ (approximately).

As with the simple strain sensor, the self-sensing actuator strain sensor is best suited to dynamic and quasistatic measurements. The resistor R should be chosen to achieve an appropriate time constant $R/(C_p+C_2)$. When operated at frequencies less than $1/R(C_p+C_2)$ the voltage follower will tend to drift and frequency dependent sensor dynamics are introduced.

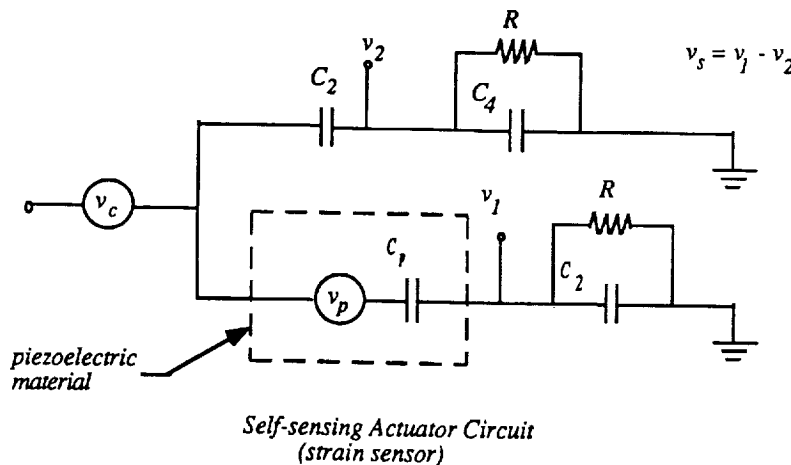


Figure 6

Experimental Results

The self-sensing actuator with rate sensing was implemented in the control of a cantilever aluminum beam. Using rate feedback the damping ratio of the beam's first mode was increased from .003 to .05 and the 5 percent settling time was reduced from 35.4 to 2.12.

Summary

Equations developed for a separate piezoelectric sensor and actuator were extended to a self-sensing piezoelectric actuator. The self-sensing actuator uses linear systems theory to simultaneously account for both the sensor and actuator dynamics of the piezoelectric material. Dynamic equations were developed for a self-sensing actuator that produced a strain signal as well as a self-sensing actuator that produced a rate of strain signal.

Design of Sensor/actuators

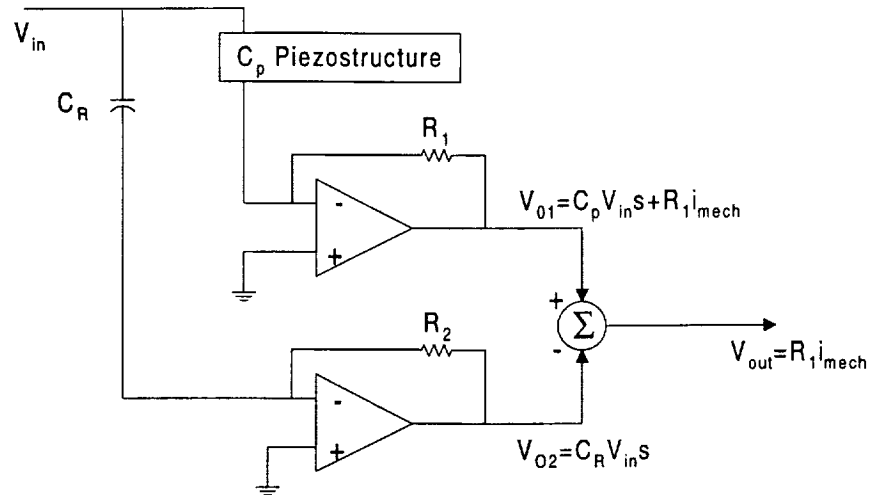
Introduction

Piezoelectric smart structures have received a considerable amount of attention in recent years because of their versatility and adaptability in difficult-to-model applications such as space trusses. Indeed, for modal analysis and rate feedback control applications, a collocated input/output response is generally desired. But when a piezoelectric material is used as both as sensor and actuator simultaneously, the sensor response consists of a direct charge term as a result of applying the actuator voltage across the piezoelectric capacitance in addition to the mechanically induced charge. Therefore, in order to isolate the mechanically induced charge from the dominant capacitance-induced charge, some sort of compensation has to be used.

Definition: A Sensor/actuator refers to a piezoelectric element used as a sensor and actuator simultaneously.

Strain rate analog compensation

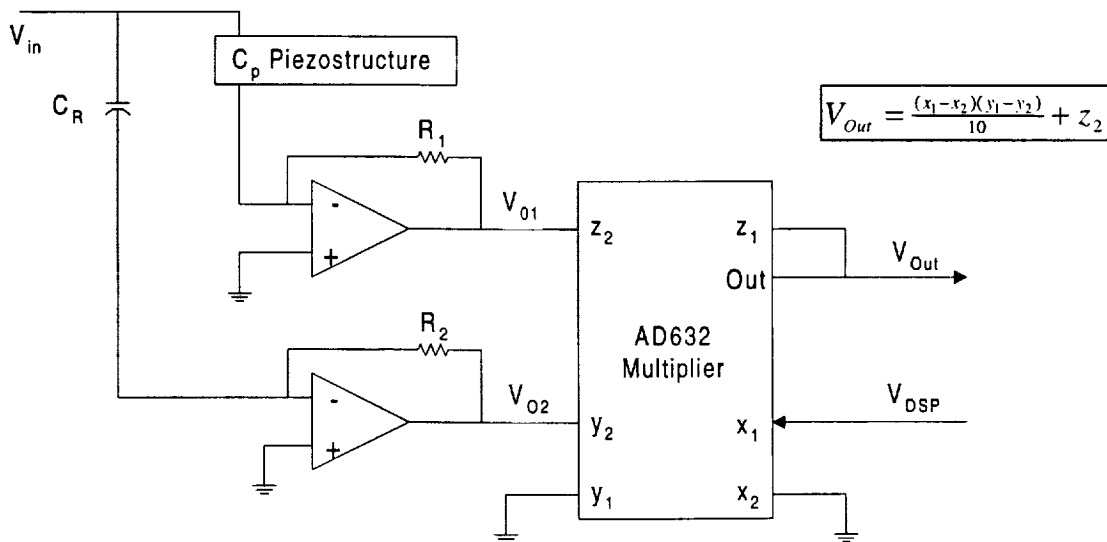
A method for compensation of the electrical term in a strain rate configuration, where strain rate is proportional to current consists in matching the electrical part of the collocated response of a parallel circuit containing a reference capacitor that is equal to the piezoelectric capacitance. Then, subtracting the output of the reference circuit from the piezoelectric circuit response, the electrical part is canceled, leaving only the mechanical response of the structure. A simple circuit diagram of the strain rate compensation scheme is shown below:



Unfortunately, day to day changes in capacitance values are significant enough to require continual readjustment of the circuit.

Hybrid Digital/Analog compensation

A circuit designed by Vipperman and Clark uses an analog multiplier with a digital, single-weight FIR filter implemented with a DSP chip to scale the reference circuit output for effective cancellation of the electrical part of the sensor response. A circuit diagram of the hybrid system appears below.



When the output of the reference circuit is properly scaled by an adaptive least mean squares (LMS) algorithm, the electrical feedthrough component is canceled leaving mechanical strain rate information only in V_{Out} .

It can be shown that the LMS weight update equation yields an expression for the adaptive compensating signal V_{DSP} as the weight update as shown below.

$$V_{DSP} \approx w(k) + \mu 2V_{Out}(k) \frac{V_{O2}(k)}{10}$$

It would be too long to explain how to use perfectly this circuit. A good knowledge of digital signal processing is required. Anyway, we will see later that we can build a circuit without any DSP chip which works much better than this one.

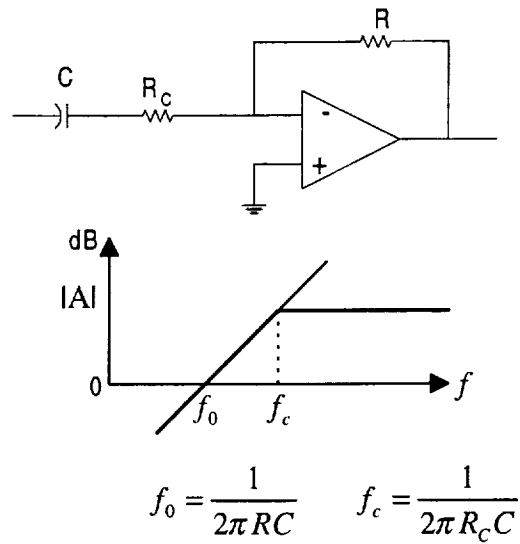
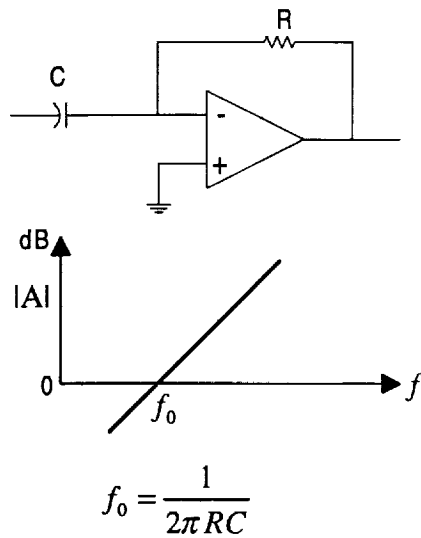
Limitations:

The circuitry described above relies heavily on the reference capacitor being similar to the piezoelectric capacitance in the primary leg of the circuit. The reason for this is the relative phase between the two circuits. Should the phase response not match the perfectly (to within 1 degree at every frequency), the system will be unable to cancel out the electrical feedthrough response of the Sensoriactuator.

Improved Differentiator Circuitry

Using op-amps in a pure differentiating realization amplifies high frequency noise, tends easily toward saturation, and is undesirable from a closed loop stability standpoint.

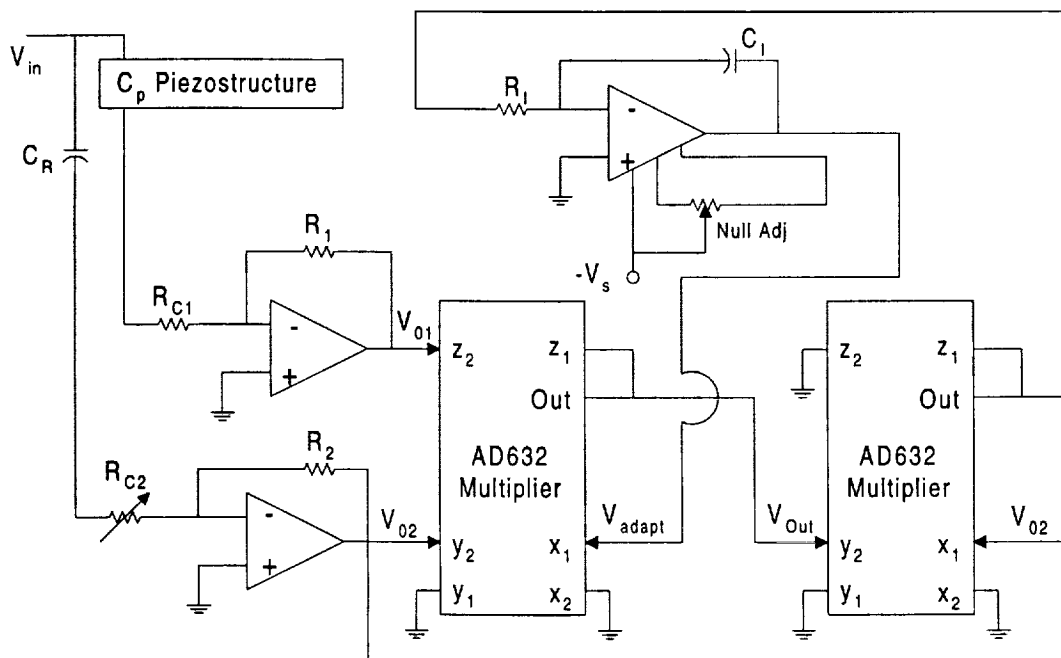
It is common practise to alleviate the troubles associated with differentiating op-amps by adding a resistor to form a high-pass filter which acts like a differentiator in a user prescribed bandwidth, as shown below:



By adjusting R_c , the pole f_c moves slightly, which results in a small shift in phase in the frequency range of interest. Now, rather than relying on the exact matching of the piezoelectric capacitance with a reference capacitor, it is possible to get good phase matching with a tuning potentiometer.

Single-Weight Analog Compensator

Using the improved differentiator in the same type of configuration that was presented by Vipperman and Clark, and a single-weight analog realization of the LMS algorithm, a new



compensation scheme is realized. This new compensator isn't plagued with the same problems of phase mismatch as the former, since the high-pass filter arrangement allows for tuning of the corner frequency, which amounts to tuning the relative phase of the two legs of the compensating circuitry. This means that it isn't as important to match a reference capacitor as with the pure differentiating scheme proposed previously. Additionally, a DSP is no longer required to adaptively compensate the feedthrough capacitance, because an analog LMS is constructed for that task. A full circuit diagram appears below.

Tuning the Compensator:

The circuit shows the use of two potentiometers. The first of these is used to tune the corner frequency of the reference circuit relative to the piezoelectric circuit (this replaces the process of matching a reference capacitor). The second potentiometer is used to adjust the null offset on the LMS integrator.

The manual tuning procedure for the reference circuit corner frequency consists of taking frequency response measurements of both legs of the compensator, comparing the relative phase response within the frequency range of interest (0-800Hz), adjusting the input potentiometer (changing the corner frequency), and repeating the frequency response measurement and comparison until the relative phase between the two legs is as close to 180° as can practically be achieved.

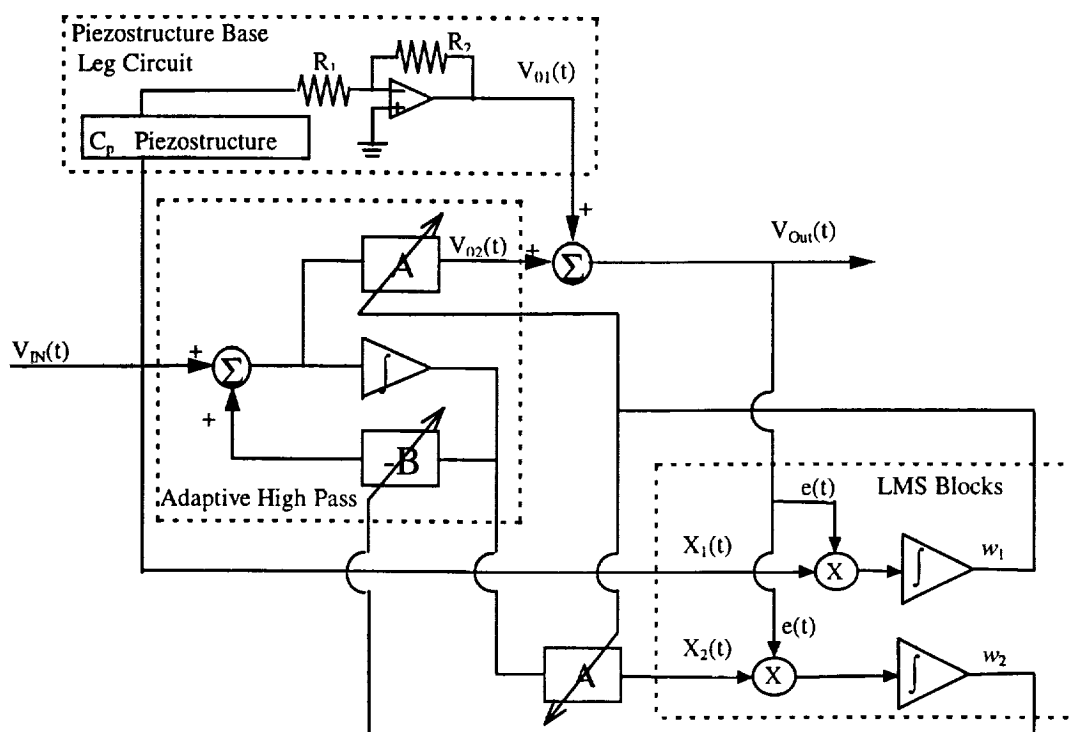
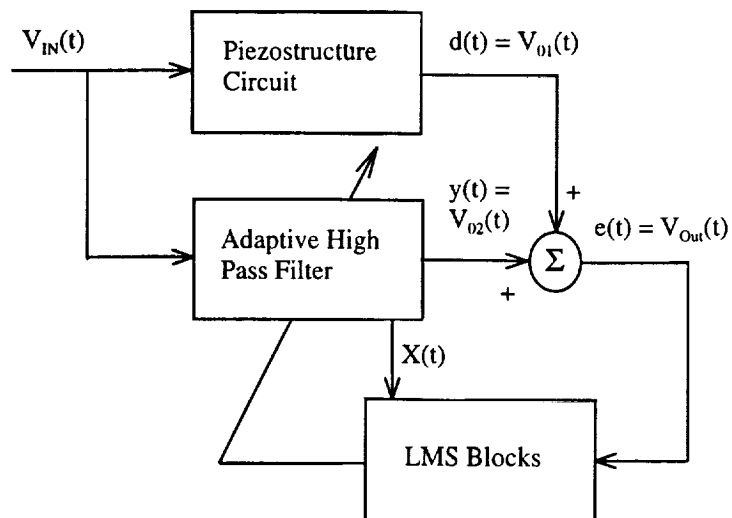
Once the corner frequency has been set as described above, the way to set the null adjust is to simply change it until the output response magnitude is minimized.

Once this tuning is complete, successive adjustments will be performed adaptively by the LMS compensator, thereby making this a seemingly more self-sustaining technique. However, as C_p changes, so does the corner frequency of the feedthrough dynamic response. This affects the relative phase between the piezoelectric and reference legs which results in less accurate compensation. Clearly, what is needed is a means of adapting the corner frequency automatically.

Two-weight Analog Compensator

Despite the apparent advantages of the analog adaptive approach described above, there are drawbacks that manifest themselves. For example, the nature of the tuning procedure makes the system less robust and more difficult to predict theoretically. Additionally, the first-order dynamics are sensitive to changes in C_p which compromises the integrity of the approach. A two-weight adaptive system, where the corner frequency adaptively changes was sought to add reliability in that it would be more hands-off for the user.

Block diagrams of this adaptive realization appear below. The second one contains more detailed information of the various components.



A full circuit diagram appears below:

This procedure should be repeated (or at least verified) at the beginning of each usage of the circuit. This circuit works very well for small excitation voltages where the PZT is operating in a linear range.

Experiments and results

Experiments were run to demonstrate and compare the performance of each circuit realization. The adaptation of the two-weight circuit was accurate assuming the excitation voltage was as high as allowable, minimizing the harmful effects of DC offsets in the circuit, which cause the adaptive weights to converge improperly. The sensitivity of the circuit offset error was observed both by changing the input voltage level, and by introducing intentional offsets into the system and is probably the biggest problem with the design. The user must be cognizant of this condition and take care to minimize unwanted DC offsets especially from the analog LMS integrators.

The two-weight filter adaptation was found to be very robust with regards to both gradual and abrupt changes in piezoelectric capacitance. The system underwent a one second transient adaptation after which it converged once again to the desired solution, leaving only the mechanical strain rate response in the output. The single-weight circuit was unable to successfully adapt to any variations in the piezoelectric capacitance because of its comparatively inflexible design which excluded variability in the first-order corner frequency of the reference leg. The capability of the two-weight compensator to adaptively change the corner frequency of its high-pass filter is a clear advantage for Sensoriactuator performance.

Summary

The experiments clearly demonstrate the advantages of the two-weight circuit over the other techniques. However, several aspects of the design showed to be less than optimal.

Also, this circuit was designed expressly for the purpose of experimental system identification. Collocated strain response is ideal for closed loop applications too, but the problem with using this circuit for such an application is that the piezoelectric wafer is used as a capacitive circuit element and the voltages applied to it will be applied also to a breadboard full of solid state electronic components which are unable to handle the high voltages (100+ Volts) required for structural control.

Power Factor Correction

INTRODUCTION

In an electrical system, the power consumed is defined by the product of the voltage, current and the ratio of real to apparent power. The ratio of the real to apparent power is defined as the power factor (PF). When the supplied voltage and current are in phase, the power factor is unity. The primary reason for wanting a PF close to unity in most industrial applications is the increase in the electrical capacity of the distribution system (lower current requirements). Most electric utilities assess a penalty for a low PF. This penalty may result in a significant portion of the user's electric bill. For small facilities with low power requirements, a poor PF may result in penalties of thousands of dollars per year. Unlike purely resistive loads, inductive loads (such as motors, transformers, and industrial furnaces) require reactive or magnetizing currents.

The reactive current provides only the electromagnetic field for operating the device, it does not perform work or result in useful power being delivered to the load. Excess currents (in the form of reactive currents) increase resistive losses in power lines, transformers, etc. and degrade the electrical efficiency of a distribution system.

Because most facilities have lagging PF's (inductive loads produce a lagging PF and capacitive loads produce a leading PF), capacitors or synchronous motors are usually placed in parallel with the load to correct the PF. These capacitors operate at nearly zero PF and have a negligible internal resistance. Because there are no resistive losses within the capacitors, the addition of the capacitors does not increase the power consumption.

The practical significance of power factor correction for piezoelectric actuators is found in resonant inductor-capacitor (LC) circuits. The electrical properties of a piezoceramic actuator are similar to a capacitor. The PF of a PZT actuator is approximately zero and is leading. To correct the PF to unity, the PZT load requires the addition of a lagging PF. Therefore, the PF of the PZT can be corrected with the addition of an appropriate inductor within a small but useful frequency range.

A description of ideal and realistic resonant circuits is presented next. A solution of the inductance required to correct the PZT actuator PF to unity is also given.

THEORETICAL DEVELOPMENT

To understand the properties of the parallel resonant circuit, it is best to investigate the transfer function of V_o/V_i for the circuit in Figure 1(a). The impedance of the parallel combination of the inductor and capacitor can be shown to be,

$$Z_p = \frac{-j\omega L}{\omega^2 LC - 1} \quad (1)$$

The transfer function of the output voltage to the input voltage is then easily determined to be,

$$\frac{V_o}{V_i} = \frac{-j\omega L}{-j\omega L + \omega^2 RLC - R} \quad (2)$$

where the resonant frequency is given by,

$$\omega_r = \sqrt{\frac{1}{LC}} \quad (3)$$

At the resonant frequency, the denominator of Equation (1) reduces to zero and the impedance of the parallel combination reaches infinity. Therefore a voltage can be applied across the ideal LC combination with no current consumption. At resonance, the reactive phase between the current and voltage is zero (PF = 1).

The transfer function of the ideal series resonant circuit, shown in figure 1(b), is

$$\frac{V_o}{V_i} = \frac{j(\omega L - \frac{1}{\omega C})}{R + j(\omega L - \frac{1}{\omega C})} \quad (4)$$

When the series LC combination reaches resonance, the numerator of Equation (4) approaches zero. The imaginary components cancel and thus the voltage and current are in phase (PF = 1). The transfer function of the capacitor voltage to the input voltage at resonance is given by

$$\frac{V_c}{V_i} = \frac{Z_c}{R} \quad (\text{with } Z_c = \frac{1}{jC\omega})$$

The transfer function in Equation (5) indicates that the voltage across the capacitor can achieve much higher values than the input voltage. The amount of voltage increase is dependent on the value of the resistor chosen and thus the magnitude of this transfer function can theoretically reach infinity at resonance.

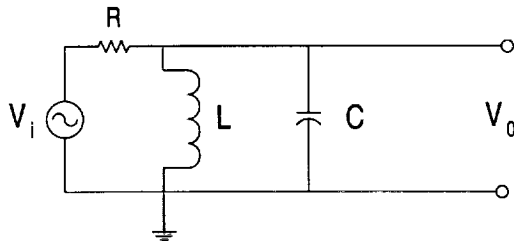
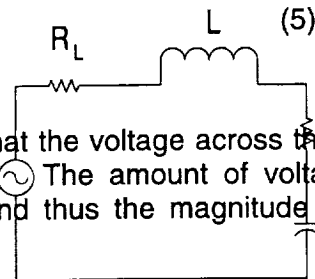


Figure 1(a): Ideal resonant circuit
Parallel resonance

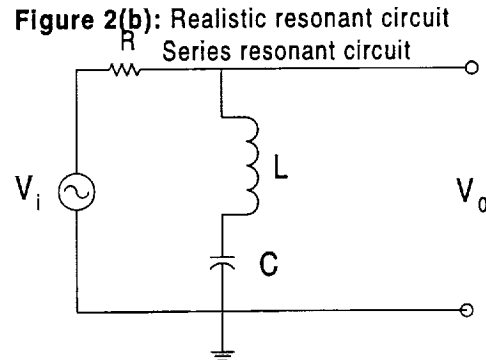


Figure 1(b): Ideal resonant circuit
Series resonance

Because electrically the PZT actuator behaves similar to a capacitor, the benefits of the LC resonance can be applied. PZT actuators and all inductors have some internal resistance that is not negligible. This internal resistance must be incorporated for an accurate model. The circuits used to model the behavior of the realistic resonant circuits are

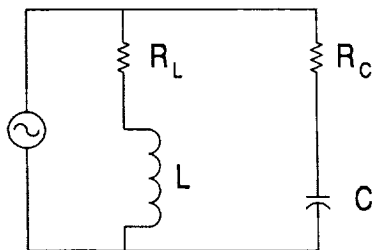


Figure 2(a): Realistic resonant circuit
Parallel resonant circuit

shown in figure 2. The model treats the PZT actuators as pure electrical elements and does not consider the electromechanical coupling effects. When determining the inductor that is required to cause electrical resonance at a particular frequency, several things must be known: the operating frequency, the PZT electrical properties, and the internal resistance of the inductor being considered. Because the internal resistance of the inductor can not be known exactly before choosing the specific inductor, a value must be assumed.

To solve the appropriate inductor, the power factor of the LC combination must be driven to unity. For both the series and parallel circuits, the imaginary component of impedance is driven to a zero at a particular frequency. This leads to two different solutions for the correcting inductance. For the parallel case, the correcting inductance is given by,

$$L = \frac{R_c^2 C}{2} + \frac{1}{2\omega^2 C} \pm \frac{1}{2} \sqrt{\left(R_c^2 C + \frac{1}{\omega^2 C}\right)^2 - 4\left(\frac{R_L^2}{\omega^2}\right)} \quad (6)$$

For the series case, the correcting inductance is given by,

$$L = \frac{1}{\omega^2 C} \quad (7)$$

Parallel resonant circuits are best suited for amplifiers that are current limited, while series resonant circuits are best suited for amplifiers that are voltage limited. Series resonant circuits also protect the amplifier from current spikes and flyback voltages, and also provide inherent filtering of high frequency noise.

IN PRACTICE

It is necessary to verify the properties of the LC resonant circuits described in the theoretical development. For the parallel LC circuit, it is necessary to show that near the electrical resonant frequency, the current needed to provide a given amount of actuation is reduced by using the parallel resonant circuit. For the series LC circuit, it is necessary to show that near the electrical resonant frequency, the PZT actuation is increased for a given input voltage by using the series resonant circuit.

In order to measure the PZT actuator power, voltage and current measurements are

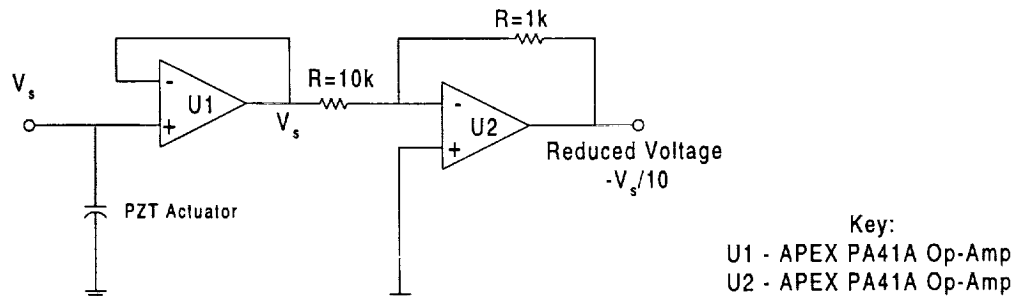


Figure 4: Voltage reducer circuit

required and the appropriate electronic circuits are developed. The circuits are shown in Figures 4 and 5. By using the ratio of the voltage with respect to current in a load, it is possible to obtain a measure of the impedance of the load. Several sine dwell tests are performed on the PZT actuator and the inductor at various voltage levels. From these tests,

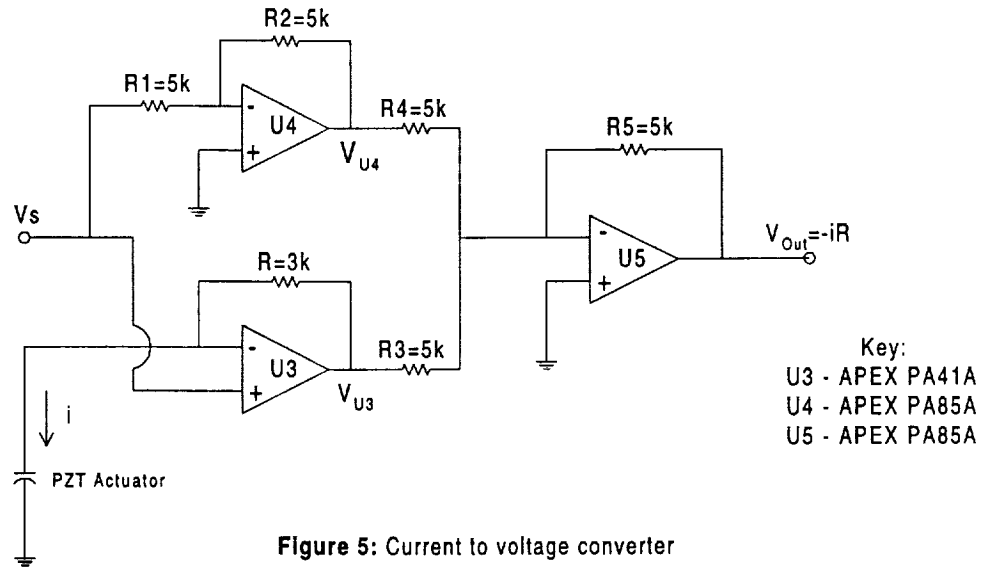


Figure 5: Current to voltage converter

a complex impedance is obtained and the inductance (L), PZT capacitance(C), and the internal resistances (R_L and R_C) can be extracted.

EXAMPLE WITH RESULTS

The length of a cantilevered beam in aluminum is 33.97 cm, the width is 4.0 cm, and the thickness is 0.3 cm. Two piezoceramic patches are used to actuate the structure and are mounted on either side of the beam, 4.47 cm from the root. A single patch is 3.65 cm long, 1.9 cm wide, and 0.0305 cm thick. An accelerometer is positioned at the tip of the beam to measure the vibration amplitude.

Implementing the parallel LC resonant circuit reduced the actuator current consumption by 75%, while implementing the series LC resonant circuit produced a 300% increase in voltage applied to the actuator compared to the case when no inductor was used. In both cases, the power factor has been corrected and the PZT apparent power has been reduced by 12dB for a given amount of actuation.

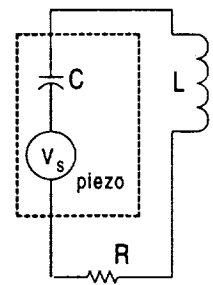
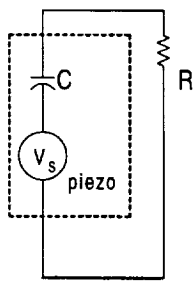
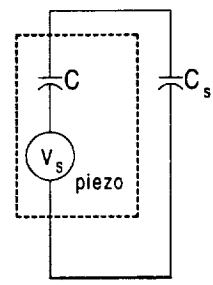
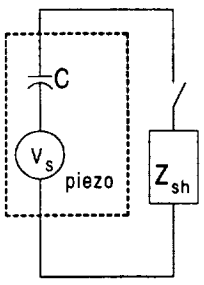
Shunted Piezoelectric Materials

Introduction

If a piezoelectric element is attached to a structure, it is strained as the structure deforms and converts a portion of the energy associated with vibration into electrical energy. The piezoelectric element (which behaves electrically as a capacitor) can be connected to a network of electrical elements (a "shunt" network). This network may be configured to accomplish vibration control by modifying the dynamics of the electrical system. It is made possible by the relatively strong electromechanical coupling exhibited by modern piezoelectric materials.

Four basic kinds of shunt circuits are typically used: inductive, resistive, capacitive and switched. Each of these kinds of shunts results in a characteristically different electrical dynamic behavior.

The figure shown below outlines the main areas of research activity in shunted piezoelectrics over the past decade.

INDUCTIVE	RESISTIVE	CAPACITIVE	SWITCHED
 <p>Resonant (damped) absorber</p>	 <p>Frequency dependent damping</p>	 <p>Frequency dependent stiffness</p>	 <p>Controlled energy transfer</p>
Tuning strategies Passive vs synthetic inductors Single vs multimode Active (slow) tuning Circuits topology Effects of : structural damping nonlinearities RL-shunted CLD Hybrid active-passive Power efficiency	Peak damping Frequency dependence tuning distribution Modal strain energy Effects of : electrode size local stiffening damped composites particulate fiber-reinforced	Adjust stiffness of part of mechanical vibration absorber Active (slow) tuning	Active (fast) shunting rectifier resistance inductance rate

Inductive (Resonant) Shunting

Inductive shunting results in a resonant LC circuit, the behavior of which is analogous to that of a mechanical absorber (tuned mass damper).

We can consider that the effect of inductive shunting is to cancel the inherent capacitive reactance of the piezoelectric elements, but we can also interpret the operation of a resonant shunted piezoelectric (RSP) in terms of an analogy with a passive mechanical vibration absorber (PVA) or tuned mass damper (TMD), in which a relatively small second-order system (in this case, an electrical one) is appended to the dynamics of a larger system. In this case, the system (or device) electromechanical coupling coefficient plays a role similar to that of the mass ratio in conventional absorber design, in that small coupling requires very accurate tuning for good performance. In addition, the shunting system operates to counter strain energy, not kinetic energy.

If we add a resistance (damping) to the shunt network (now RLC), we have a damped vibration absorber. It is interesting to add a resistance because the addition of damping makes system performance less sensitive to changes in the response frequency of concern. We can focus on the case of an absorber designed to minimize mechanical response to broadband excitation. If we use an equivalent circuit approach, with uniform field and strain assumptions for the piezoelectric element, the results for tuning the parameters (inductance L and resistance R) of the shunt circuit closely parallel classical damped vibration absorber tuning results. As shown in the equations below, the inductance is tuned to adjust the natural frequency of the shunt circuit, while the resistance is tuned to adjust the different response levels over some frequency range.

$$\frac{\omega_{electrical}^S}{\omega_{mechanical}^E} = \frac{1}{\sqrt{LC}\omega_{mechanical}^E} = \sqrt{1+k_{system}^2}$$

$$\tau_{electrical}^S \omega_{mechanical}^E = RC^S \omega_{mechanical}^E = \sqrt{2} \frac{k_{system}}{1+k_{system}^2}$$

Key: $\omega_{electrical}^S$ is the electrical resonant frequency

$\omega_{mechanical}^E$ is the mechanical system's natural frequency with the piezoelectric open-circuited

k is the electro-mechanical coupling coefficient, defined as the square root of the ratio of the stored energy of one kind (electrical or mechanical) to the input energy of the second kind (mechanical or electrical)

Passive inductors needed for reasonably sized mechanical structures can be massive, as the size varies inversely with both the square of the tuning frequency and with the piezoelectric capacitance.

Inductive shunts have also been considered for use when the piezoelectric element is to be driven actively, as an actuator. For instance, Niezrecki and Cudney (1993) addressed power factor correction using inductive shunting (see Chapter 5).

Resistive Shunting

Resistive shunting dissipates energy through Joule heating, which has the effect of structural damping. Using monolithic piezoelectric elements, this approach has been considered as a kind of alternative to conventional constrained layer damping treatments.

If we consider the case of a monolithic piezoelectric element attached to a structure and shunted with a resistor, we can note that as the shunt resistance increases from zero, the effective loss factor increases, peaks, and then decreases; the effective stiffness increases monotonically between low and high asymptotic values. The peak structural loss factor depends on the system coupling coefficient: the higher the coupling, the higher the damping.

For a given resistance the stiffness of the piezoelectric changes from its short circuit value at low frequencies to its open circuit value at high frequencies. The frequency of this transition is determined by the shunting resistance. The material also exhibits a maximum loss factor at this transition point.

The value of this maximum loss factor can be found to be

$$\eta_{\max-ij}^{RES} = k_{ij}^2 / \sqrt{1 - k_{ij}^2} \quad (k \text{ is the electromechanical coupling coefficient})$$

at a non-dimensional frequency of

$$\rho_i = R_i C_{pi}^S \omega = \sqrt{1 - k_{ij}^2} \quad \text{with} \quad C_{pi}^S = C_{pi}^T [1 - k_{ij}^2]$$

($\rho_i = \omega / \omega_d$ where ω_d is the open-circuit natural vibration frequency and C_{pi}^T is the capacitance between the surfaces perpendicular to the i th direction at constant stress)

Thus by appropriate choice of resistor, the peak of the loss factor curve can be moved to the desired frequency.

It is worthwhile to draw a comparison between resistively shunted piezoelectrics and viscoelastic materials. For common viscoelastic materials, the peak loss factor occurs in a narrow frequency and temperature range where the viscoelastic is in transition from its rubbery state to its glassy state. This placement is directly analogous to the peak loss factor of the piezoelectric occurring at the transition from short circuit to open circuit stiffness.

It should be noted that the loss factor curve takes the same form as the standard relaxation curve for material damping, but can lead to material loss factors as high as 8.2% in the transverse case and 42.5% in the longitudinal or shear cases for commonly available piezoelectric ceramic materials. While these loss factor levels are not as high as those for viscoelastic materials, the high stiffness (about 63GPa) of the shunted piezoelectric materials (typically a ceramic) gives them advantages over viscoelastic materials (about 1MPa) since for a given strain they can store many times the strain energy of the viscoelastic and thus contribute to higher system loss factors. The piezoelectric material properties are also relatively temperature independent below their Curie temperature (temperature at which they lose their piezoelectric properties). For commonly available piezoelectrics this is typically the range of several hundred degrees centigrade. However, the piezoelectric material density is much higher than that of viscoelastic materials. The net effect is that in most cases resistively shunted piezoelectric materials can provide higher total structural damping levels per unit mass with higher temperature stability than viscoelastic materials.

Capacitive Shunting

A capacitive shunt effectively changes the stiffness of a piezoelectric element without affecting its damping. Little research has addressed the application of this shunt method to date. However, this approach enabled the development of a tunable mechanical vibration absorber.

Switched Shunting

The key feature of shunting approaches in this category is rapid response to the instantaneous conditions of the structure/shunt system, with *rapid* meaning on a time scale much shorter than a characteristic period of vibration. Systems that slowly tune themselves based on some kind of mean structural response are included in the categories described in the preceding sections.

A switched shunt offers the possibilities of controlling the energy transfer to reduce frequency-dependent behavior.

Summary

Shunted piezoelectrics are a relatively recent addition to the structural vibration control engineer's toolbox. The general approach involves the following:

1. Incorporation of piezoelectric elements in a structure in such a way that they deform when the structure vibrates. Familiar concepts such as modal strain energy can be used to guide placement and sizing of the elements, but the system electromechanical coupling coefficients should be carefully determined to ensure the potential for satisfactory performance.
2. Design of an appropriate shunt network to accomplish specific vibration control objectives. The main options include the following:
 - a) For tonal (narrowband) excitation, an electrical or mechanical vibration absorber might be appropriate. An electrical vibration absorber involves the use of an inductive shunt, perhaps with low resistance; a mechanical vibration absorber involves the use of capacitive shunting to vary the stiffness of a piezoelectric element. If the excitation frequency varies, the resonance frequencies of both kinds of absorbers can be actively tuned. As an alternative to active tuning, damping can be added to either kind of absorber by providing resistance in the shunt network. If resonant response is a concern, relative or switched shunting can also be used to increase effective modal damping.
 - b) For broadband or transient excitation in which the structural response is dominated by specific modes of vibration, an inductive-resistive (damped resonant) shunt might be appropriate. The resonance frequency and damping of the shunt can be passively tuned to minimize structural mean-square response. Alternatively, a switched shunt might be used to remove energy from structural vibration and dissipate or store it into the shunt.

Advantages that shunted piezoelectrics might exhibit over alternative approaches include design flexibility, relative insensitivity to temperature (compared to viscoelastic materials) and high effective loss modulus in resistive shunting applications (the product of loss factor and modulus of elasticity). Once a piezoelectric element has been incorporated in the structure and a shunting approach is selected, fine-tuning can be accomplished by adjusting the values of discrete electrical components.

Features that could be regarded as advantages or disadvantages, depending on the application, include the ability to be adjusted electronically, either for slow tuning or rapid switching. Since it does not do work on the structure (as a purely active vibration control system would), a shunt controller requires very little power, just enough to keep some electronics warm. If a synthetic inductor were used in a resonant shunting application, such

power would be available already. The disadvantage, of course, is that synthetic inductors and active shunt controllers are not purely passive systems.

Potential disadvantages in the use of shunted piezoelectric elements include relatively low tensile strain to failure (for piezoceramics), relatively high density, little data on fatigue properties, and issues related to mechanical bonding and electrical wiring.

Continued research and development of methods for using shunted piezoelectrics for vibration damping and control are needed.

VII. Application: Adding Damping to a Plate

The goal of the active control tests was to establish a technique for vibration suppression in a representative aircraft component. This technique combined the technology of optical fiber sensors with piezoelectric actuators to minimize the vibration levels in the test article. The specific control law used for the active control tests is called Positive Position Feedback (PPF). This control law uses a generalized displacement measurement from the test article to accomplish the vibration suppression.

The test panel used for the active control tests is a 500mm X 600mm, 20-gauge, galvanized steel plate with two 2.85in X 2.85in piezoelectric actuators bonded to its surface. The test plate can be seen in Figure 7.1.

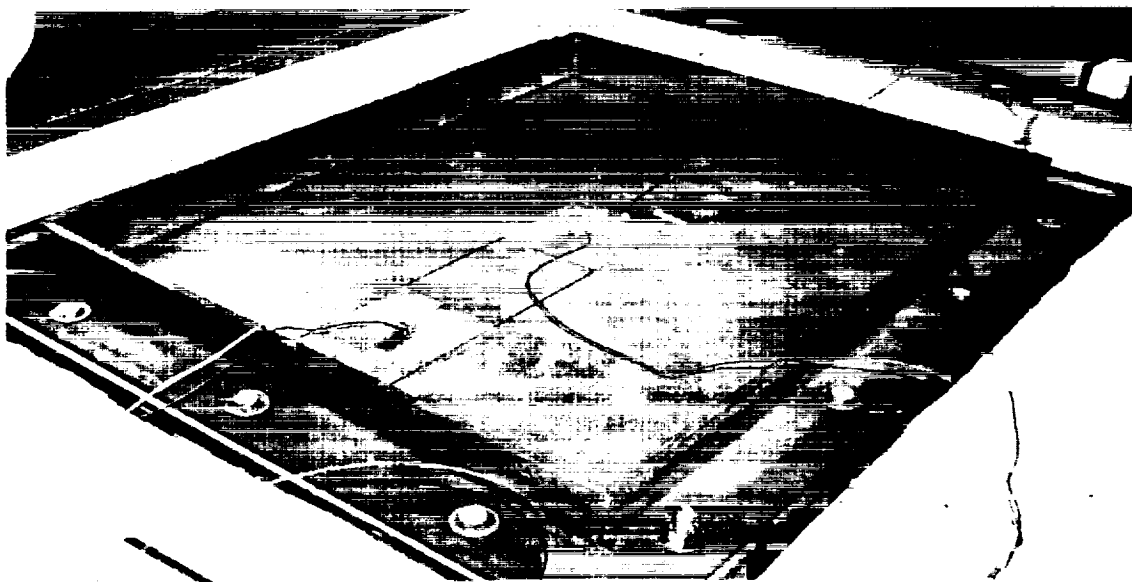


Figure 7.1. Placement of Piezoelectric Actuators

These two locations were chosen for the actuators because the plate has a large amount of strain energy in these regions for the modes that needed to be controlled. In general, the control authority of an actuator is increased when it is placed in a region of high strain energy. Although the test plate has two piezoelectric actuators attached to its surface, it was determined that the center PZT was more effective at minimizing the levels of vibration.

The sensor used for control was a modal domain optical fiber sensor for vibration monitoring. This sensor is based upon a laser that focuses coherent light through a lens into one end of a multimode optical fiber. One end of the fiber was attached to the plate and the other end of the optical fiber passed through a spatial filter and into a photodetector. The output of the photodetector is a variable voltage that is fed into a monitoring unit such as an oscilloscope. The optical fiber sensor was placed on the center PZT and can be seen in Figure 7.2.

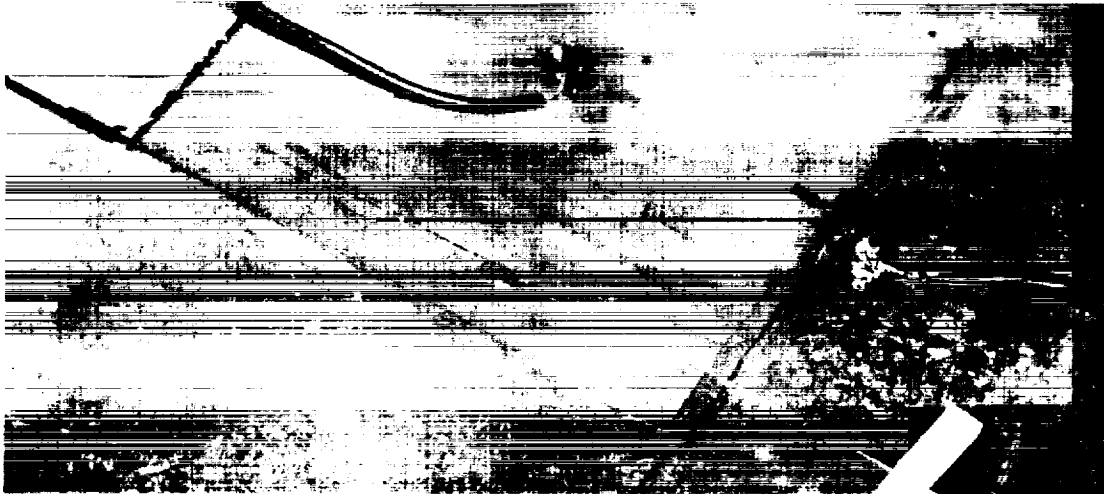


Figure 7.2. Placement of Optical Fiber Sensor

Positive Position Feedback (PPF)

Positive position feedback is a relatively new technique for vibration suppression that uses a displacement measurement to accomplish control. PPF control is a stable and relatively simple control method for vibration suppression [1]¹. The control law for a PPF controller consists of two equations, one describing the structure and one describing the compensator:

$$\text{Structure: } \xi'' + 2\gamma\omega\xi' + \omega^2 \xi = g\omega^2 \eta \quad (7.1)$$

$$\text{Compensator: } \eta'' + \gamma_f \omega_f^2 \eta = \omega_f^2 \xi \quad (7.2)$$

where g is the scalar gain >0 , ξ is the modal coordinate, η is the filter coordinate, ω and ω_f are the structural and filter frequencies, respectively, and γ and γ_f are the structural and filter damping ratios, respectively. The positive position terminology in the name PPF comes from the fact that the position coordinate of the structure equation is positively fed to the filter, and the position coordinate of the compensator equation is positively fed back to the structure. The block diagram of a PPF filter can be seen in Figure 7.3. In effect, a PPF controller behaves much like an electronic vibration absorber.

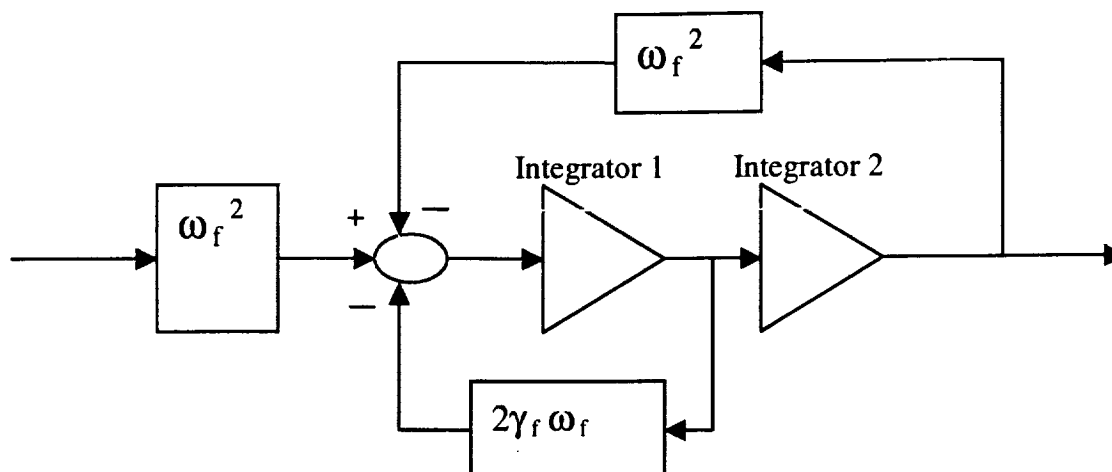


Figure 7.3. Block Diagram of PPF Filter

dSPACE and Simulink Block Diagram

The block diagram for the PPF filter and for the rest of the control system was setup in Matlab's Simulink Toolbox in conjunction with a dSPACE control board. Simulink is a graphical program that allows the user to input a block diagram and generate the corresponding ANSI C-code. The C-code is generated from Matlab's target files, which specify the particular code for each block used in the Simulink model. The control system's Simulink block diagram can be seen in Figure 7.4.

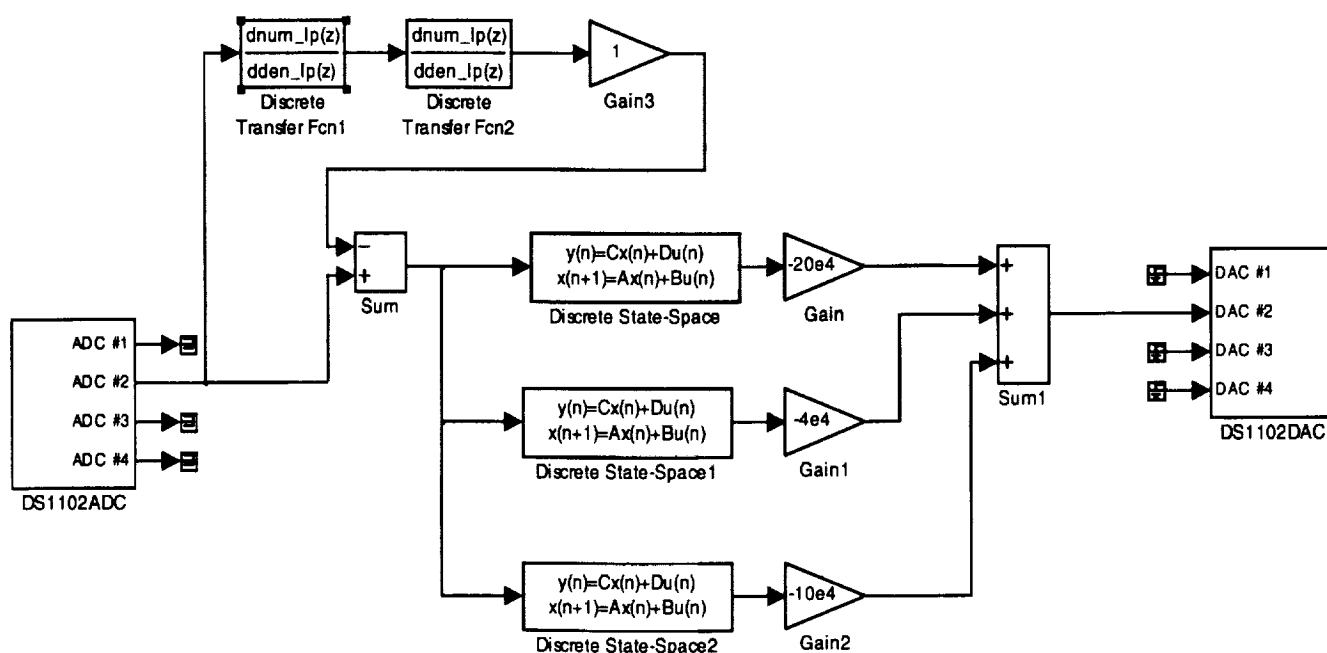


Figure 7.4. Simulink Control System Block Diagram

Each block in Figure 7.4 corresponds to a particular part of the control system. The block at the far left, labeled DS1102ADC, and at the far right, labeled DS1102DAC, are the analog to digital and the digital to analog converters, respectively. The two blocks labeled Discrete Transfer Function 1 and Discrete Transfer Function 2 are high-pass filters, which eliminate any DC-offset that the optical fiber sensor may contain. The Discrete State Space blocks contain the PPF filters for each mode of the representative aircraft panel that needs to be controlled (See Figure 7.3 for the model of each PPF filter). The active control system was designed by tuning each PPF filter to control one or more of the modes of the representative aircraft panel. The entire control system block diagram can be seen in Figure 7.5, which shows how the Simulink model and dSPACE board fit into the control system.

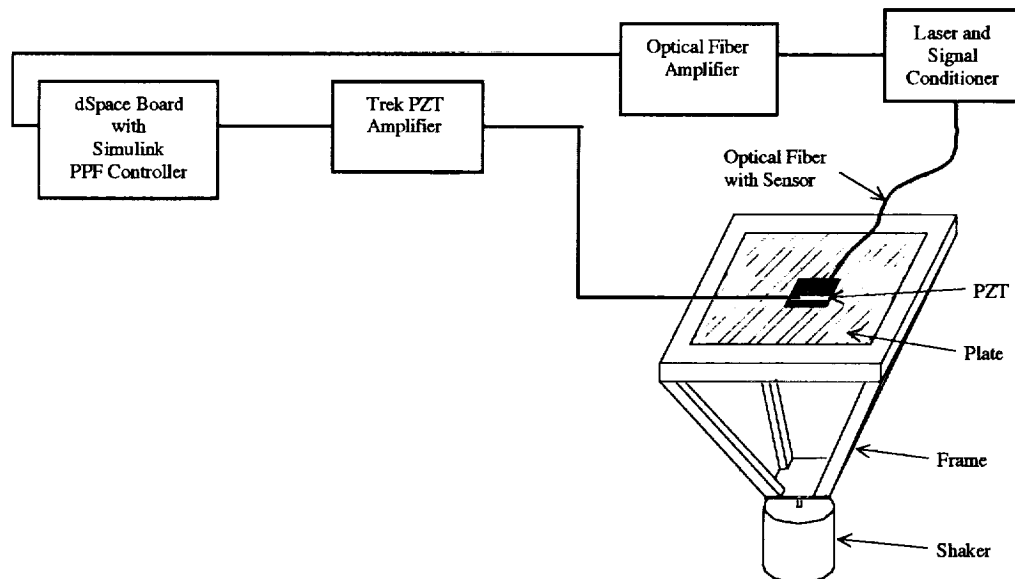


Figure 7.5. Control System Block Diagram

The control system was set up such that the optical fiber sensor sends a signal through a signal conditioner and amplifier into the dSPACE board. Once the signal was processed through the PPF control law it was sent out to an amplifier to drive the PZT actuator.

Active Control Test Setup and Procedure

The system's parameters and the overall control system's performance were measured using a two channel HP Dynamic Signal Analyzer. This signal analyzer was used to get the frequency response function between the plate and the clamping frame using two accelerometers, one on the bottom center of the

plate and one on the clamping frame. A complete system block diagram showing the overall test setup can be seen in Figure 7.6 below.

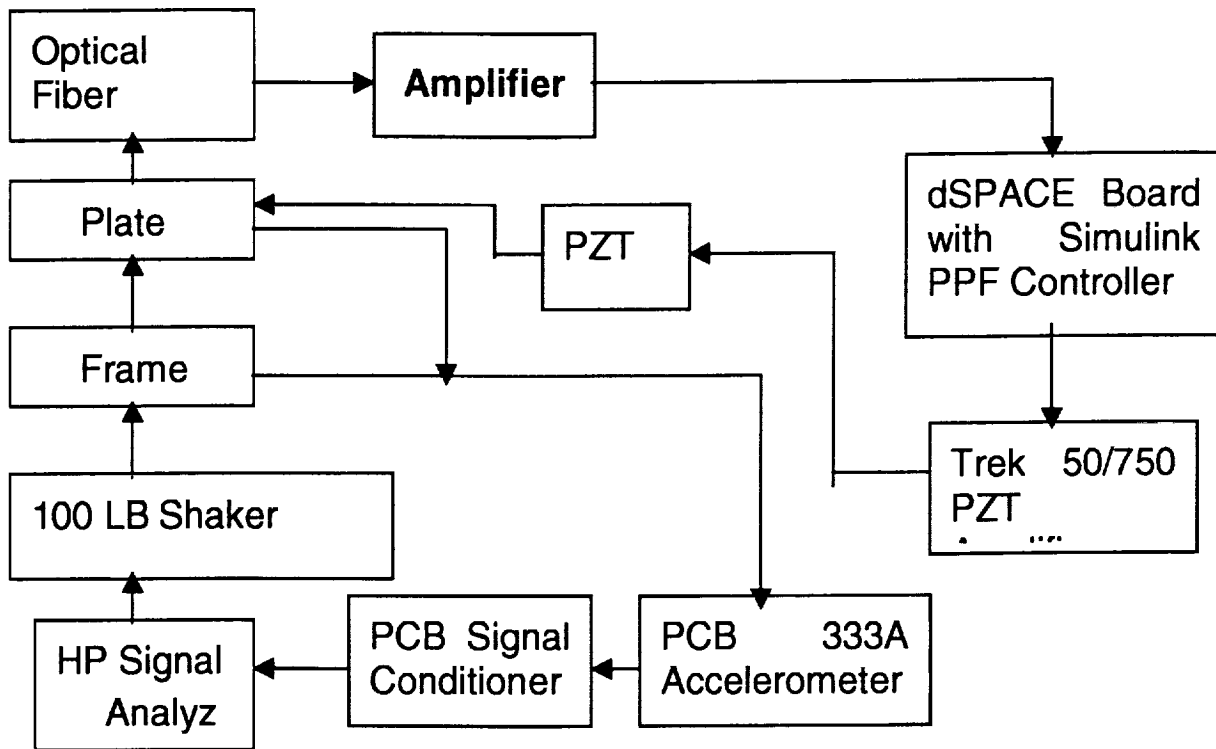


Figure 7.6. Active Control Test Setup

The active control tests were conducted in a controlled environment in the Advanced Vehicle Dynamics Laboratory at Virginia Tech. The testing procedure for the active control tests is as follows:

1. Turn on the equipment (PC, HP Analyzer, Amplifiers, and Signal Conditioners).
2. Set the HP Dynamic Signal Analyzer for two channels, uniform window, anti-aliasing filter on, 20 averages, span of 400 Hz, periodic chirp input, and 800 spectral lines.
3. Set the gain on the Trek 50/750 PZT amplifier to 100.
4. Set the gain on the PCB signal conditioner at 10 for both channels.
5. Set the filter frequency and the damping ratios for the PPF filters in the Simulink model.
6. Turn on the shaker and the controller.
7. Take data on the HP Dynamic Signal Analyzer.

Active Control Test Results

A series of tests were run to determine the optimum parameters for the active vibration suppression of a representative aircraft panel. These parameters, ranging from the gains assigned to the various amplifiers to the damping ratios of the PPF filters, were based upon the tuned frequency and the number of modes assigned to each PPF filter. The final Simulink Model used for the active control tests, shown in Figure 7.4, uses three PPF filters to provide active damping to most of the modes from 0-400 Hz. However, you can achieve significant active damping of a mode or modes with one PPF filter tuned properly.

There were two different means of supplying energy to the plate for the active control tests. The first method used a 100 lb shaker to excite the plate mechanically, and the second method used a 10" sub-woofer to excite the plate acoustically. Both the shaker and the speaker were driven with a 0-400 Hz periodic chirp input signal, which is shown in Figures 4.5 and 4.6.

The initial design procedure for the active control system was to create a Simulink model with one PPF filter to control as many modes as possible. This design method involved determining the frequency range at which the system had control authority over multiple modes. The tests results show that the control system with one PPF filter was most effective when tuned to a frequency between 60 and 70 Hz. Figures 7.7 and 7.8 show some of the best results obtained with the one PPF filter controller. In each of these tests the 100 lb shaker excited the plate mechanically.

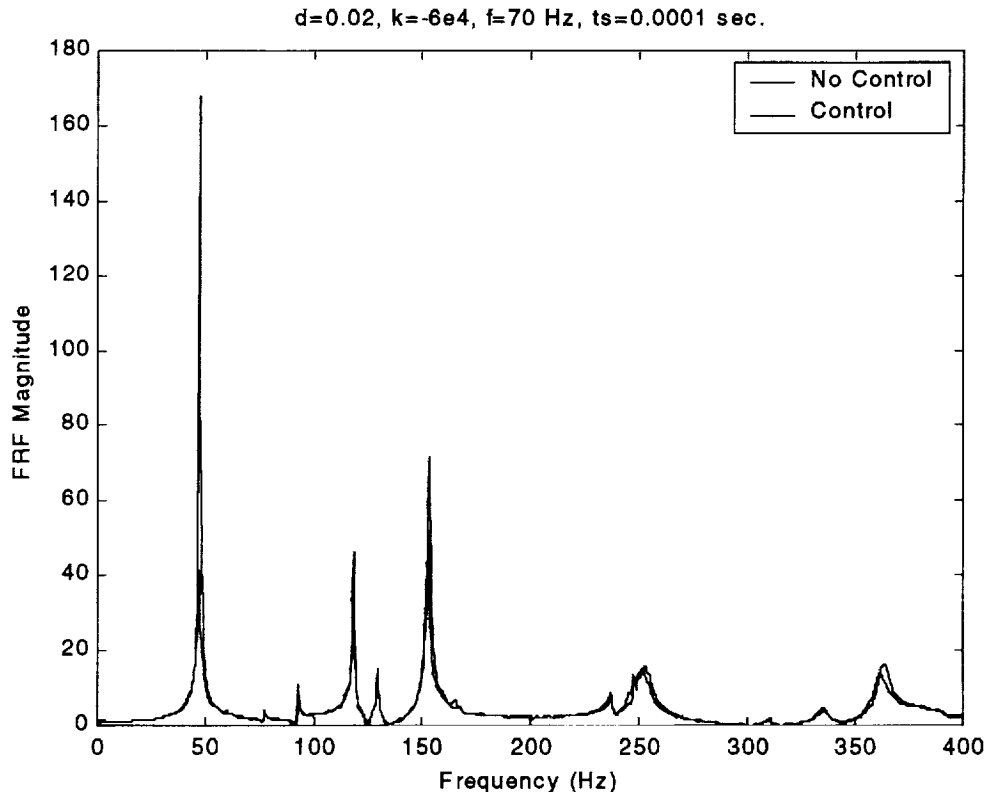


Figure 7.7. Active Control with 1 PPF Filter (Mechanically Excited)

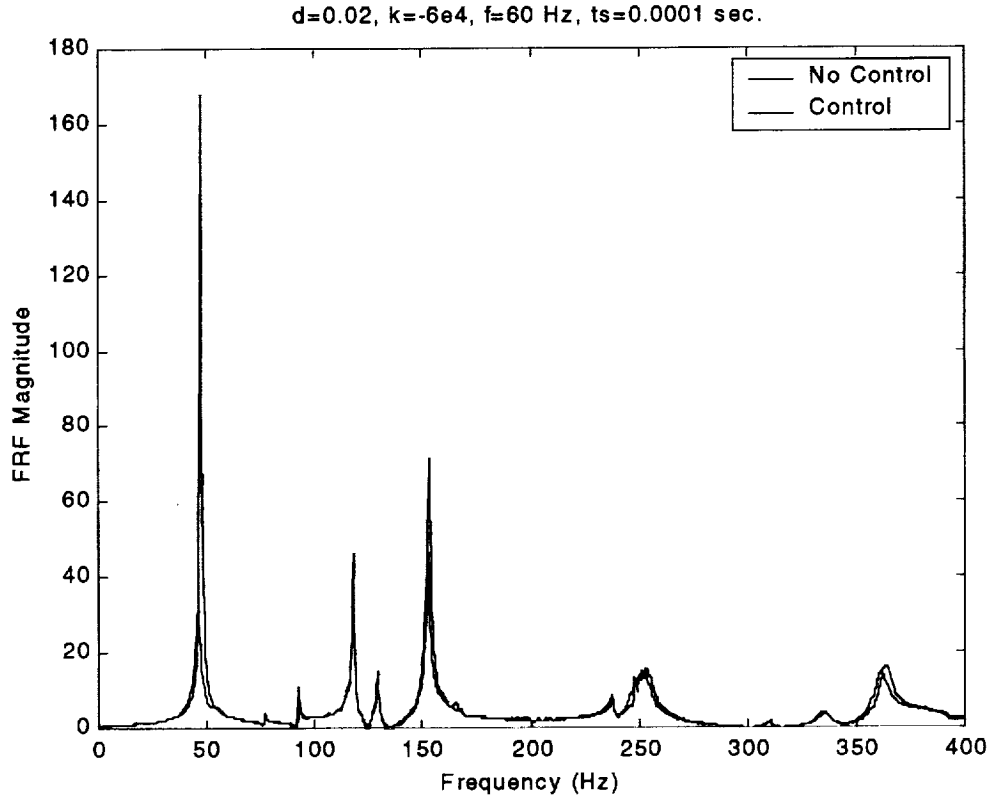


Figure 7.8. Active Control Test with 1 PPF Filter (Mechanically Excited)

The active control test shown in Figure 7.7 was run with a PPF filter damping ratio of 0.02, a Simulink gain of $-60,000$, a sampling time of 0.0001 seconds, and tuned to a frequency of 70 Hz. The active control test shown above in Figure 7.8 was run with the same parameters as the test shown in Figure 7.7 except the filter was tuned for 60 Hz. These figures show that the control authority of the first mode is increased as the frequency of the PPF filter approaches the frequency of the first mode, 47 Hz. It should be noted that as the frequency of the PPF filter was decreased to below 60 Hz, the control authority of the higher modes were also decreased.

In the acoustic tests, a 10 in. sub-woofer was placed just under the center of the plate, approximately 2 inches away. The plate was excited with the same 0-400 Hz periodic chirp input signal, however, the frequency response function had to be taken differently. Instead of taking the input as the frame accelerometer, the input of the frequency response function was changed to the generated input signal to the speaker. Figure 7.9 shows the results obtained with a one PPF filter controller when the plate was excited acoustically with a 10 in. sub-woofer.

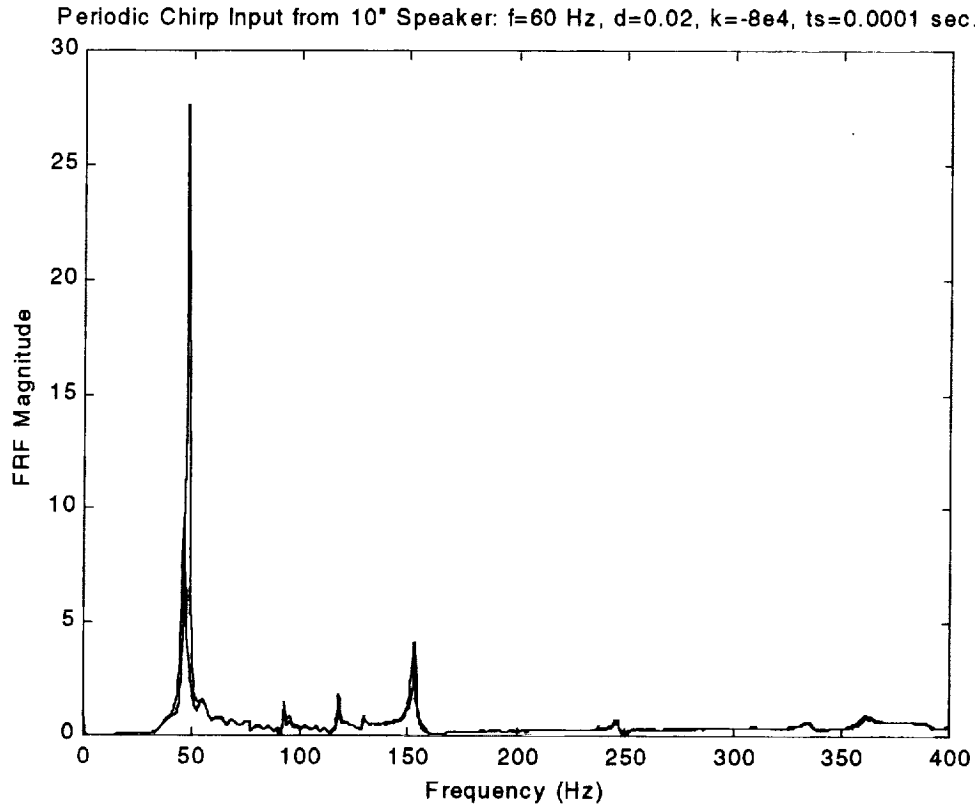


Figure 7.9. Active Control Test with 1 PPF Filter (Acoustically Excited)

The active control test shown in Figure 7.9 was run with a PPF filter damping ratio of 0.02, a Simulink gain of $-80,000$, a sampling time of 0.0001 seconds, and tuned to a frequency of 60 Hz.

Additional tests were run using pure tone inputs at the resonant frequencies of the plate. These tests were performed to determine the effectiveness of the controller in the suppression of the structure born noise resulting from the vibration of the test plate. Most of these tests were run at the first resonant frequency of the plate (47 Hz) because this mode produced the most audible structure born noise. The test results proved that the controller reduced the noise from the plate significantly. Figure 7.10 shows the best reduction achieved by the controller with a 47 Hz pure tone input signal.

47 Hz Pure Tone Input from 100 lb Shaker: $f=60$ Hz, $d=0.02$, $k=-8e4$, $t_s=0.0001$ sec.

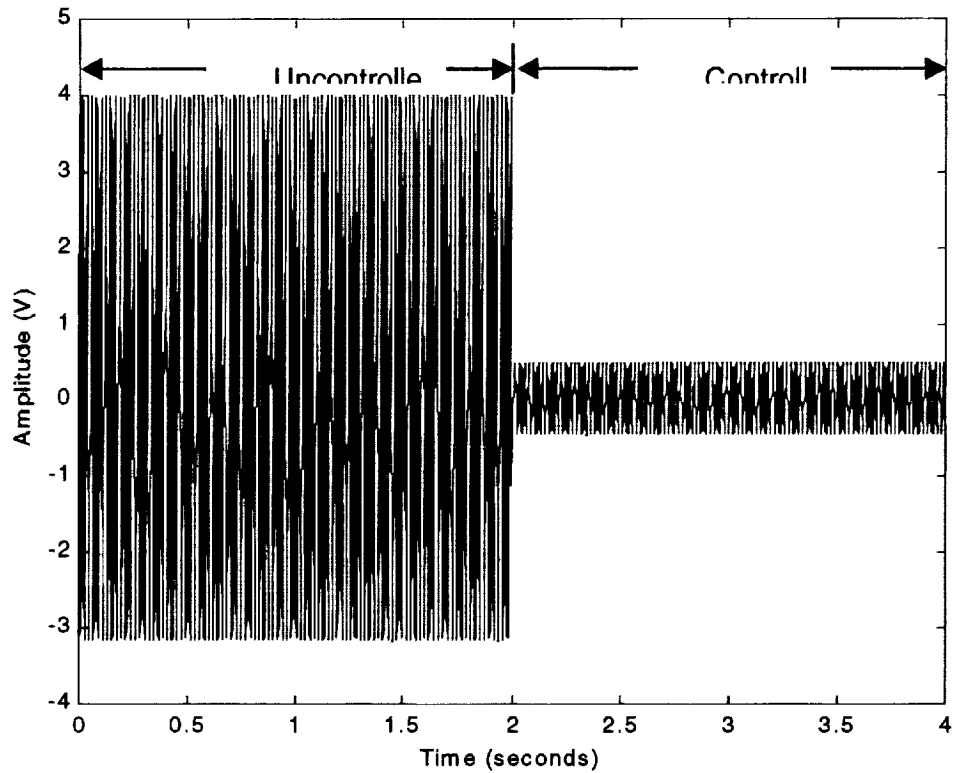


Figure 7.10. 47 Hz Pure Tone Active Control Test

The final controller design, as shown in Figure 7.4, has three PPF filters to attack multiple modes in the 0-400 Hz frequency range. This controller has an advantage over the one PPF filter controller because it can be tuned to three frequencies and, therefore, have more control authority over the structure. Figure 7.11 shows some of the best results obtained with the three PPF filter controller.

3 PPF Filters: $d_1=d_2=d_3=0.02$, $k_1=-8e4$, $k_2=-6e4$, $k_3=-9e4$, $f_1=60$ Hz, $f_2=130$ Hz, $f_3=160$ Hz

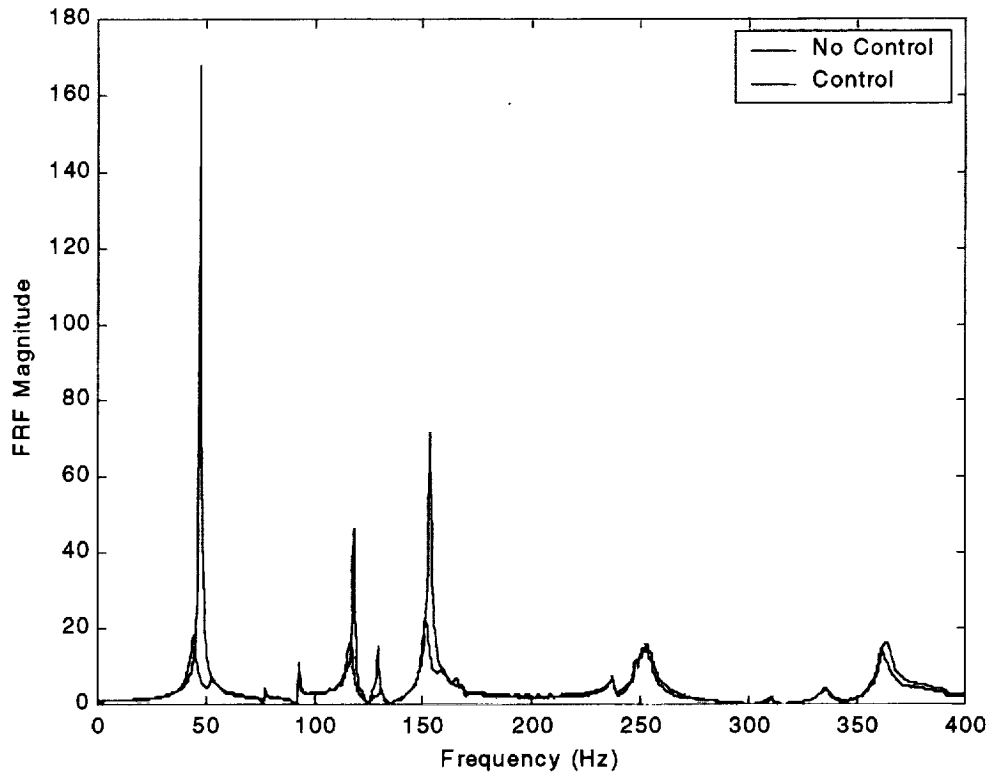


Figure 7.7. Active Control Test Results with 3 PPF Filters

The parameters listed at the top of Figure 7.7 correspond to the damping ratios, the Simulink gains, and the frequencies of the three PPF filters, respectively. The results from this figure show that the three PPF filter controller can achieve a reduction in the first mode of the plate up to 89% with an added weight of only 0.11 lb.

VII. Impedance-based Health Monitoring Technique

Impedance Method

A new smart health monitoring technique capable of in-situ, on-line incipient damage detection in complex structures was employed after an extensive search of possible damage detection methods.. The basic concept of this impedance-based structural health monitoring technique is to monitor the variations in the structural mechanical impedance caused by the presence of damage. Since structural mechanical impedance measurements are difficult to obtain, this non-destructive evaluation technique utilizes the electromechanical coupling property of piezoelectric materials.

This health monitoring method uses one PZT patch for both the actuating and sensing the of the structure response. The interaction of a PZT patch with the host structure can be described by a simple impedance model. Figure 7.1 presents the elements of the model. The PZT is considered as a thin bar undergoing axial vibrations in response to the applied sinusoidal voltage.

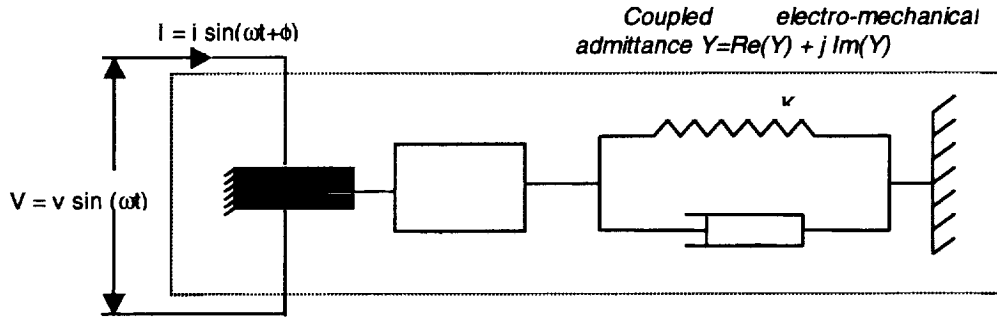


Figure 7.1. 1-D model used to represent a PZT-driven dynamic structural system.

Solving the equation for the PZT bar connected to the external mechanical point impedance of the structure leads to Equation (1) for the frequency dependent complex electrical admittance $Y(\omega)$ (inverse of impedance). The variables Z_a and Z_s represent the PZT's and the structure's mechanical impedance, respectively. Y_{xx}^E is the Young's modulus of the PZT at zero electric field, d_{3x} is the piezoelectric coupling constant in an arbitrary x-direction at zero stress, ϵ_{33}^T is the dielectric constant at zero stress, δ represents the dielectric loss tangent of the PZT, and a is the geometric constant of the PZT. Equation (7.1) clearly indicates the direct relation of the mechanical impedance of the structure to the electrical impedance bonded onto this structure.

$$Y(\omega) = i\omega a \left(\bar{\epsilon}_{33}^T (1 - i\delta) - \frac{Z_s(\omega)}{Z_s(\omega) + Z_a(\omega)} d_{3x}^2 \hat{Y}_{xx}^E \right) \quad (7.1)$$

Damage in the structure is reflected in changes of the parameters such as mass, stiffness, or damping. Assumed that the PZT's parameters remain constant any changes in the mechanical impedance Z_s change the overall admittance. Previous

Experiments in the laboratories have shown that the real part of the overall impedance contains sufficient information about the structure and is more reactive to damage than the magnitude or the imaginary part. Therefore, all impedance analyses are confined to the real part of the complex impedance. The actual health monitoring is done by saving a healthy impedance signature of the structure and comparing the signatures taken over the structure's service life.

Implementing the NDE in the Test Setup

First laboratory tests on the uncontrolled plate showed the ability of the impedance method to detect certain forms of damage on the plate. The tests used the same PZT patches as for the control system. The impedance measurements were taken with an HP 4194A impedance analyzer. A frequency range from 45 kHz to 55 kHz proved to be an optimum for this structure. To simulate damage on the plate one or two bolts of the clamping frame were loosened from 25 ft-lb. to 10 ft-lb. Figure 7.2 shows a sketch of the frame and names the bolts to be loosened. Adding mass to the test specimen could not be used to simulate damage, because the mechanical impedance is mostly defined by the boundary conditions of the clamped plate.

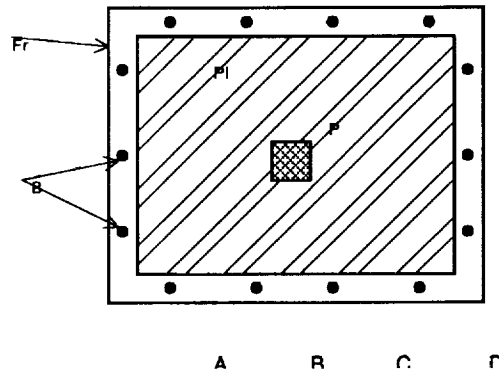


Figure 7.2. Clamping Frame with Bolts.

Since the task consisted of simultaneous health monitoring and active control with the same actuators for both the control and the health monitoring system needed to be de-coupled. The impedance method is very sensitive to disturbing voltages in the measuring circuit. The controller however creates exactly those disturbances by generating the control signal. A simple capacitor of 390 nF in series with the impedance analyzer blocked efficiently the control signal from the impedance analyzer. The block diagram of the test setup is presented in Figure 7.3. All health monitoring data presented in this report was taken while the shaker was exciting the plate with a periodic chirp signal from 0 to 200 Hz. The active controller was also switched on and increased the damping of the first three modes of the plate significantly.

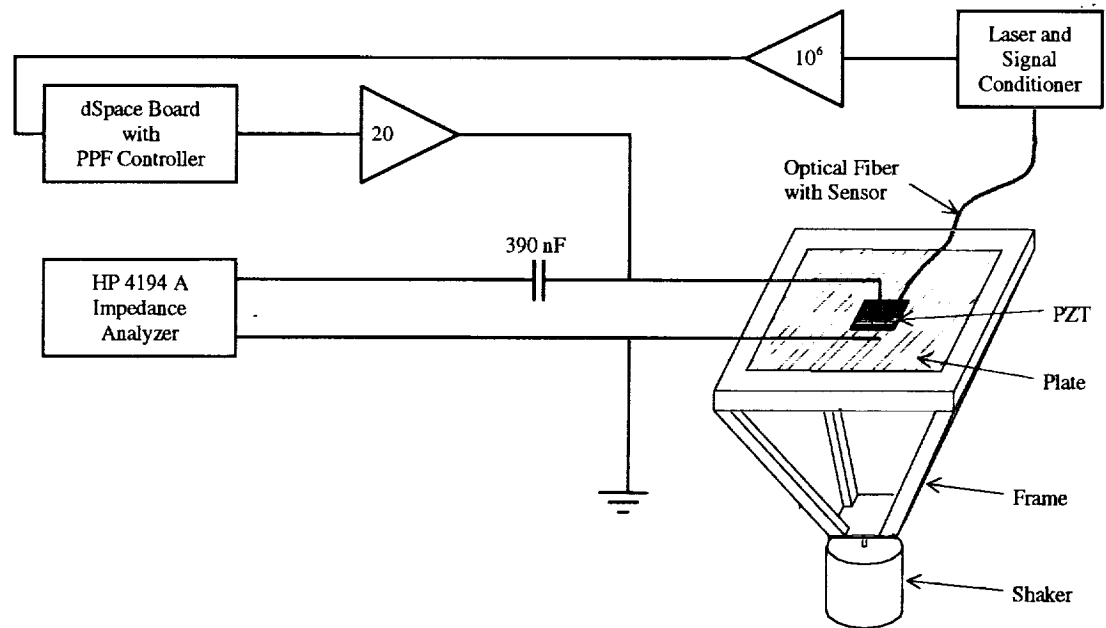


Figure 7.3. Block Diagram for Health Monitoring and Active Control

Health Monitoring Results

Figure 7.4 shows the impedance signatures of the undamaged and damaged plate. To simulate damage the bolts B and C were loosened to 10 ft-lb. torque from 25 ft-lb. Only the frequency range from 45 to 55 kHz is shown. The signature change is significant because both bolts are very close to the PZT patch.

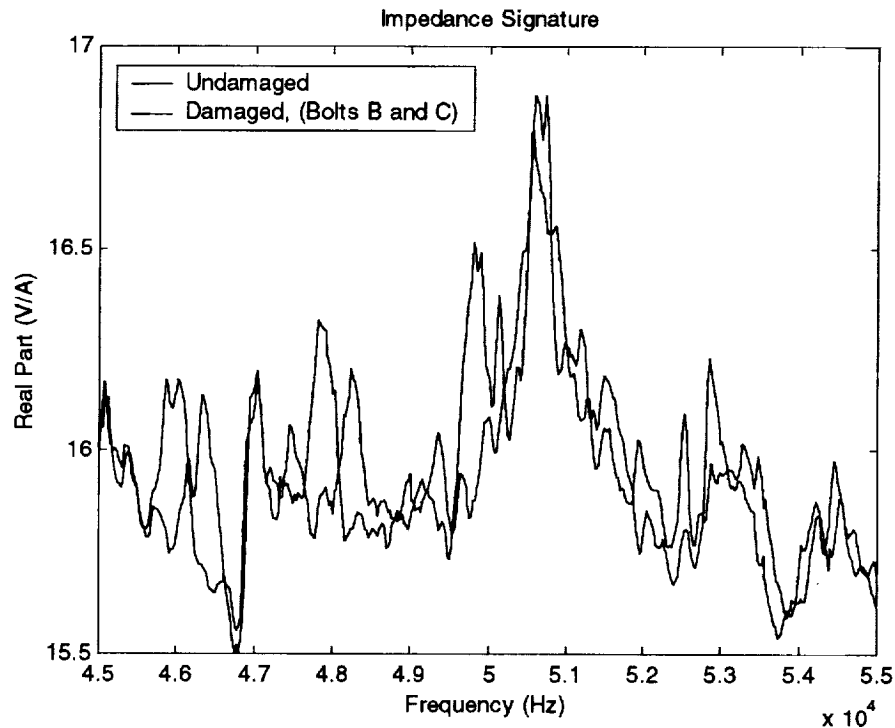


Figure 7.4. Impedance Signatures for Undamaged and Damaged Plate.

For comparing impedance signatures, a qualitative damage assessment has been developed. The assessment is made by computing a scalar damage metric, defined as the sum of the squared differences of the real impedance at every frequency step. Equation 7.2 gives the damage metric M in a mathematical form. The used variables include: $Y_{i,1}$ the healthy impedance at the frequency step i , $Y_{i,2}$ the impedance of the structure after the structure has been altered, and n the number of frequency steps.

$$M = \sum_{i=1}^n [\text{Re}(Y_{i,1}) - \text{Re}(Y_{i,2})]^2 \quad (7.2)$$

The damage metric simplifies the interpretation of the impedance variations and summarizes the information obtained by the impedance curves. Different damage metric values of the plate are presented in Figure 7.5. Note the difference in the metric between one bolt loosened and two bolts loosened. It supports the idea of a damage threshold value to warn an operator when this threshold value has been reached.

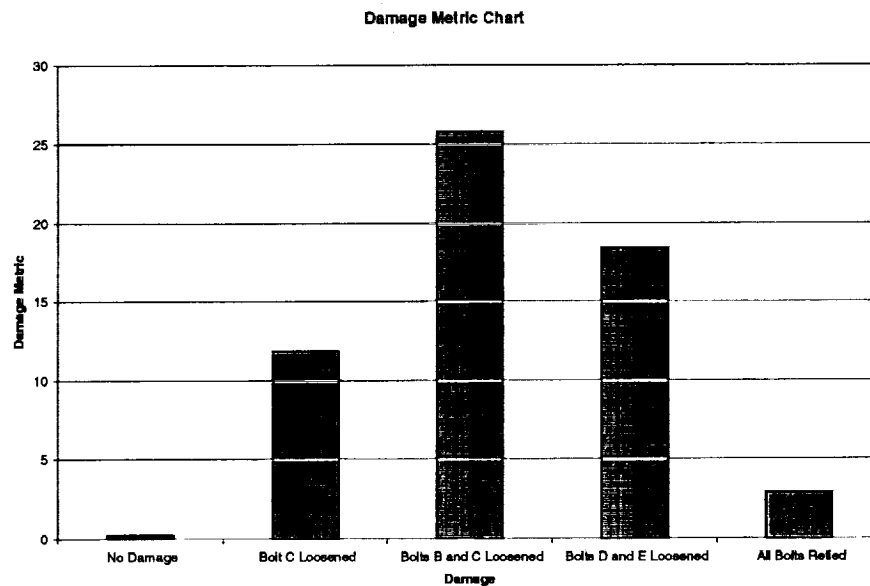


Figure 7.5. Damage Metric Chart of Different Impacts to the Plate.

The chart also illustrates that the closer the damage to the sensor happens the earlier the damage can be detected. Loosening bolts D and E surely represent a similar damage then loosening bolts B and C. However, the damage metric of bolts D and C loosened is smaller than the damage metric of bolts B and C loosened. This is due to the relative distance of the damage impact to the PZT sensor.

Figure 7.5 also shows a problem of the impedance technique. After retying all bolts back to 25 foot-pounds torque, another set of impedance values was taken and the damage metric was computed. The metric value on the right demonstrates that the impedance signatures from the undamaged plate and the "repaired" plate were noticeable different. The impedance technique is so sensitive that it is almost impossible to achieve the same impedance signature as before altering after the structure was altered and re-altered.

To prove the reliability of the NDE technique several measurements in intervals of several hours were taken. During all measurements, the shaker applied a periodic chirp vibration signal to the plate and the active controller was in operation. No damage was induced to the test specimen for this experiment. The results are presented in Figure 7.6. The hours in the graph specify the time passed after the first data set was taken. Figure 7.6 also contrasts the repeatability metrics to an actual impact on the structure.

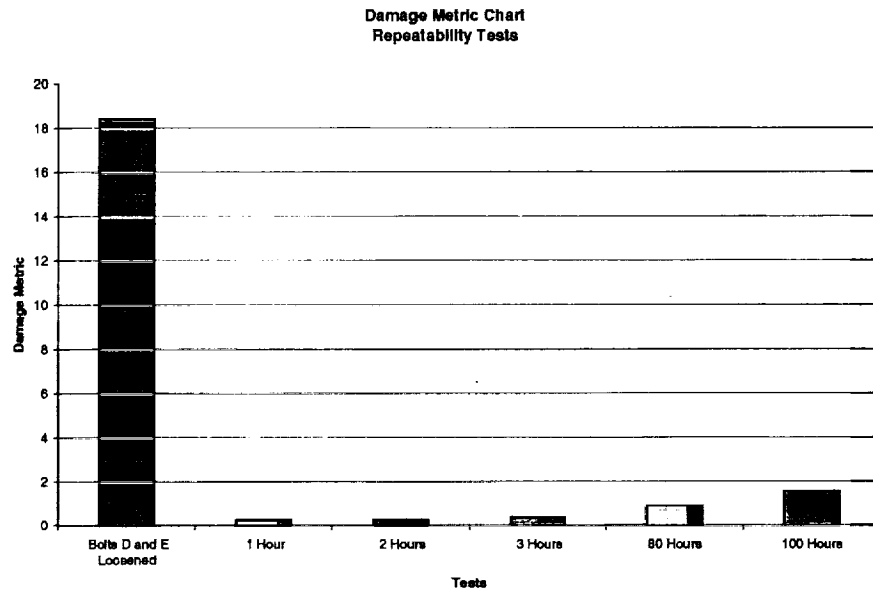


Figure 7.6. Damage Metric Chart, Repeatability Tests.

The plot shows that there is a slight drift in the scalar damage metric over time due to changing environment conditions. Compared to values of damage metrics of altered structures this drift could be neglected.

IX. Mathematical Symbols

Symbol	Meaning	Unit
A	cross-sectional area	mm^2
I	moment of inertia	mm^4
b	beam (actuator) width	mm
t	beam (actuator) thickness	mm
T	beam-actuator thickness ratio	-
E	Young's modulus	N/mm^2
ψ	beam-actuator stiffness ratio	-
σ	axial stress	N/mm^2
ε	axial strain	-
Λ	actuator free induced strain	-
F	actuator force	N
M	moment generated by actuator	Nm
κ	beam curvature	mm^{-1}

X. Suppliers of Piezoceramic Materials and Engineered Actuators

Piezoceramic Suppliers

Company	Telephone / Fax	Address	Comments
American Piezoceramics	717-726-6961 / 717-726-7466	Duck Run, PO Box 180, Mackeyville, PA 17750	Piezoceramics, bimorphs, simple actuators
AVX Corporation	803-349-6261 / 803-347-0873	2875 Highway 501 West, Conway, SC 29526	Piezoceramics, actuators
Channel Industries	805-967-0171 / 805-683-3420	839 Ward Dr, Santa Barbara, CA 93111	Piezoceramics, actuators
EDO Acoustics Division	801-486-2115 / 801-486-2115	2645 South 300 West, Salt Lake City, UT 84115	Piezoceramics, actuators, partially finished actuators
Keramos Inc.	317-876-4670 / 317-876-4681	5460 West 84th Street, Indianapolis, IN 46268	Piezoceramics, sensors
Morgan Matrox Inc	216-232-8600 / 216-232-8731	232 Forbes Rd, Bedford, OH 44146	Piezoceramics, sensors
Motorola (Components Div.)	505-822-8801 / 505-822-8812	4800 Alameda Blvd N.E., Albuquerque, NM 87113	Piezoceramics, sensors
PCB Piezotronics	716-684-0001 / 716-684-0987	3425 Walden Avenue, Depew, NY 14043-2495	Finished actuators, transducers, sensors
Piezo Kinetics	814-355-1593 / 814-355-4342	PO Box 756, Mill Rd & Pine Street, Bellefonte, PA 16823	Piezoceramics, actuators, partially finished actuators
Piezo Systems	617-547-1777 / 617-354-2200	186 Massachusetts Ave., Cambridge, MA 02139	Piezoceramics, design kits, speciality design
Polytec PI	508-832-3456 / 508-832-0506	23 Midsate Dr, Suite 104, Auburn, MA 01501	Piezoceramics, actuators, partially finished actuators
Rockwell	805-373-4608 / 805-373-4423	1049 Camino Dos Rios, MC A9, Thousand Oaks, CA 91360	Piezoceramics
Sensor Technology Ltd.	705-444-1440 / 705-444-6787	20 Stewart Road, Collingwood, Ontario, Canada, L9Y 3Z4	Piezoceramics, actuators, partially finished actuators
Tokin America Inc	408-946-4887 / 408-434-0375	2261 Fortune Dr, San Jose, CA 95131	Piezoceramics, actuators

Piezoceramic Actuator Manufacturers

Company	Telephone / Fax	Address	Comments
Active Control Experts	617-577-0700 / 617-577-0656	215 First Street, Cambridge, MA 02142-1227	Actuators, partially finished actuators
EDO Acoustics Division	801-486-2115 / 801-486-2115	2645 South 300 West, Salt Lake City, UT 84115	Piezoceramics, actuators, partially finished actuators
Face International Corp.	757-624-2121 / 757-624-2128	427 West 35th Street, Norfolk, VA 23508	Thunder Actuators
Material Systems Inc	978-486-0404 / 978-486-0706	521 Great Road, Littleton, MA 01460	Actuators, partially finished actuators
PCB Piezotronics	716-684-0001 / 716-684-0987	3425 Walden Avenue, Depew, NY 14043-2495	Finished actuators, transducers, sensors
Polytec PI	508-832-3456 / 508-832-0506	23 Midsate Dr, Suite 104, Auburn, MA 01501	Piezoceramics, actuators, partially finished actuators
DSM, Inc.	615-292-7022 / 615-292-7076	2909 12th Street, Franklin, TN 37204	Actuators, partially finished actuators

XI. References

Smart Materials/Actuators

"Investigation of Active Vibration Damping Using Magnetostrictive Mini Actuator," Bi, J. & Anjanappa, M., 1994. Purely numerical simulation of using magnetostrictive actuators to control beam vibration. No description of the physical practicality (mounting the actuator).

"Engineering Feasibility of Induced Strain Actuators for Rotor Blade Active Vibration Control," Giurgiutiu, V., Chaudhry, Z., Rogers, C. A., 1994. Looked at induced strain actuators (PZT, PMN, magnetostrictive) to control a helicopter rotor blade. PMN & magnetostrictive produce only positive strains, no tension. Discusses strain as a function of loading and energy per unit mass. The induced twist concept for rotor blades is not practical with PZT's and requires a new generation of PZT's having higher strain/volt capabilities. Direct actuation is not feasible due to a lack of displacement for a given stack length. The servo flap concept requires a displacement amplifier and is not feasible for primary flap control. Energy feasibility has been established for this application but not weight.

"A New Terfenol-D Actuator Design with Applications to Multiple DOF Active Vibration Control," Haynes, L., Geng, Z., Teter, J., 1993. They have created a magnetostrictive actuator with a stroke of +/- 5 mil. However, it is 8 inches long and 2" in diameter. Length of the rod determines stroke and area determines the force. The actuator requires a magnetic bias and a spring preload. The actuator is used in a vibration isolation experiment.

"Modal Sensors and Actuators for Individual Blade Control," Nitzsche, F., 1993. PZT's are the most promising candidate to be employed in the active control of helicopter rotor vibration. PZT's have saturation limits one or two orders of magnitude less than required to suppress helicopter rotor vibration.

"Development and Analysis of a Self-Sensing Magnetostrictive Actuator Design," Pratt, J., Flatau, A. B., 1993. Discusses the development of a self-sensing magnetostrictive actuator. The present design is unrealizable due to the non-linear behavior.

"Feasibility Study to Build a Smart Rotor: Trailing Edge Flap Actuation," Samak, K. D., Chopra, I., 1993. Experimentally use PZT bimorphs to control a helicopter rotor blade. The paper basically describes the experiment and its results.

"A Study of the Feasibility of Using Adaptive Structures in the Attenuation of Vibration Characteristics of Rotary Wings," Nitzsche, F., Breitbach, E., 1992.

The best candidate for a smart actuator is the PZT. The damping ratio of highly damped modes can not be increased very much by state feedback. Only lightly damped modes will benefit. In low-damped, lightly-loaded modes, piezoceramics have enough power to provide attenuation.

"A Comparison of Piezoelectric and Electrostrictive Actuator Stacks," Galvagni, J. & Rawal, B., 1991. This paper has a brief comparison of PZT's and electrostrictive materials. The major differences between them are: 1. electrostrictive actuators have little hysteresis (<2%) while PZT's do (15-20%). Also electrostrictive materials have a limited temperature range +/- 20 deg. C and have only positive strains which are not linear but quadratic wrt applied voltage (PZT's have a linear relationship).

"Development of an Active Member Using Piezoelectric and Electrostrictive Actuation for Control of Precision Structures," Anderson, E. H., Moore, D. M., Fanson, J. L., Ealey, M. A., 1990. Compares PZT and PMN actuator. Electrostrictive: The strain is proportional to the square of the applied voltage, for small strains; for larger strains it becomes more linear. The PZT strain coefficient and loss tangent varies w/strain. PZT loss tangent is 20-30% while the PMN loss tangent is about 1%. for a given voltage and current the PZT consumes more power because of the larger loss tangent. The PZT dielectric coefficient is 1500 while PMN dielectric coefficient is about 15000. So PMN's have higher capacitance and require higher current for a given voltage. Both required a large DC bias voltage. For PZT's the gain (displacement/voltage) increases as the displacement increases while for PMN's it decreases. PMN's also have a large variation of the gain and capacitance with temperature. PZT hysteresis is approximately 15% while PMN hysteresis 1%.

"Active Vibration Control of Flexible Beams Using Shape Memory Actuators," Baz, A., Imam, K., McCoy, J., 1990. Nitinol is used to control a cantilever beam. Bandwidth < 10 Hz.

"Exploratory Study of the Acoustic Performance of Piezoelectric Actuators," Santa Maria, O. L., Thurlow, E. M., Jones, M. G., 1990. Experimentally determined the actuating ability of the PZT. The goal was for the PZT to reproduce a SPL created by a ducted fan engine (150 dB). The acoustic output were far below the levels required to control the engine. The PZT can diminish reflected acoustic waves. To be useful for active noise control, the response of the PZT must be increased by several orders of magnitude.

"Attenuation and Transformation of Vibration Through Active Control of Magnetostrictive Terfenol," Hiller, M. W., Bryant, M. D., Umegaki, J., 1989. Discusses the design of a Terfenol actuator which is used to experimentally control vibrations. The terfenol is brittle under tension and requires a DC bias coil or magnet for AC applications. The bias current in this case was 7 Amperes!

"Electrostrictive Actuators: Materials and Applications," Uchino, K., 1986. Gives a general review of the application of PZT's & PMN devices (deformable

mirrors, impact dot-matrix printer, ultrasonic motor) and cites some differences between them (strains, hysteresis). Durability of these actuators is a problem.

Actuators (General)

"Advances in Active Vibration Isolation Technology," Hyland, D. C. & Phillips, D. J., 1994. Provides an analytical and experimental description of the Active Isolation Fitting (AIF). The AIF works pretty well from 10 to 200 Hz and is independent of the structure. The actuator is based on a PZT stack and reduced vibration levels 20-30 dB.

"Recent Advances in Active Noise Control," Stevens, J. C. & Ahuja, K. K., 1991. Provide an overview of the recent developments of active noise control using anti-sound. Sound can be attenuated over most of the cross section of a cylinder with four secondary sources. A study was performed on ducts and found that an active/passive combination could achieve better performance. This paper has a lot of good references.

"Optimal Design of Piezo-Actuators for Active Noise and Vibration Control," Kim, S. J. & Jones, J. D., 1990. This paper discusses the optimal PZT thickness for a plate and the optimal bonding layer thickness.

"Model of a Bilaminar Actuator for Active Acoustic Control Systems," Bao, X. Q., Varadan, V. V., Varadan, V. K., Howarth, T. R., 1990. A bilaminar piezoelectric actuator is modeled for underwater acoustic control.

"Modal Sensors/Actuators," Lee, C. K. & Moon, F. C., 1988. Shaped sensors and actuators are used to create modal sensors/actuators.

"On the Control of Vibratory Actuators," Brockett, R. W., 1987. The idea in this paper is to use a bending standing wave to induce the motion in the longitudinal direction. Not applicable to fairings.

"Use of Piezoelectric Actuators as Elements of Intelligent Structures," Crawley, E. F. & de Luis, J., 1986

Plates

"Analysis of Active Control with On-Line System Identification on Sound Transmission Through an Elastic Plate," Koshigoe, Shozo, 1995. A simulation of PZT's actively controlling the sound transmission through a plate into a cavity. An adaptive control algorithm has been simulated and future study involves implementing an experiment on an actual fairing.

"A Time Domain Study of Active Control of Sound Transmission due to Acoustic Pulse Excitation," Koshigoe, S., Teagle, A., Gordon, A., 1995. Developed a model for noise transmission through a plate into a cavity and modeled the acoustic soundfield. Numerical simulation of the model is

performed. Cavity controlled modes are not observable through plate motion. If the sensing is based on pressure, both types of resonant modes can be suppressed using PZT actuators. Damping substances (viscoelastic materials) are ineffective against cavity-controlled modes. It is predicted that the max Q phase presents less difficulty in controlling sound transmission compared to the lift off phase.

"Bending-Vibration Control of Composite and Isotropic Plates Through Intelligent Constrained-Layered Treatments," Shen, I. Y., 1994. Provides an analytical model and a numerical simulation of an intelligent constrained-layer (viscoelastic shear layer sandwiched between a piezoelectric cover sheet and the structure to be damped). The simulation shows that the constrained layer is an improvement over active damping alone, but doesn't compare to passive damping alone.

"Optimal Design of Enclosures for Active Noise Control and Isolation," Varadan, V. V., Kim, J., Varadan, V. K., 1994. Numerical simulation of a single PZT mounted at the center of a plate in a reverberation chamber. The goal is to minimize the sound radiated into the structure by varying the size, thickness, voltage, and phase of the actuator.

"Optimal Placement of Piezoelectric Actuators for Active Structural Acoustic Control," Wang, B. T., Burdisso, R. A., Fuller, C. R., 1994. Discusses the optimal placement and sizing of PZT's. Different excitation frequencies will result in different optimal locations (this implies the solution is valid only at one frequency). Properly locating one actuator produces higher reduction than several randomly chosen locations due to control spillover.

"Distributed Transducer Design for the Active Control of Multidimensional Elastic Structures," Sullivan, J. M., 1994. Discusses the modeling of actuators with arbitrary shapes and orientations on plates and beams via shape functions and Laplacians. Discusses shading and gain weighting of actuators and sensors, develops a control algorithm for a plate and performs a simulation and experiment on a simply supported plate (see thesis).

"A Unified Analysis of Both Active and Passive Damping for a Plate with Piezoelectric Transducers," Koshigoe, S. & Murdock, J. W., 1993. Presents a good review of the constitutive equations of PZT's and their interaction with a plate. Piezoelectricity has been recognized as the favorable mechanism because the integration with load-bearing structures can be accomplished by surface bonding or embedding. To their knowledge, active control of acoustically induced noise has not been performed in a payload fairing or launch vehicle (The Aerospace Corporation).

"Modeling Approach for Two-Dimensional Distributed Transducers of Arbitrary Spatial Distribution," Sullivan, J. M., Hubbard Jr., J. E., Burke, S. E., 1993

"Controlling Plate Vibrations Using Piezoelectric Actuators," Falangas, E. T., Dworak, J. A., Koshigoe, S., 1994 "Vibro-Acoustic Control Using PZT Actuators," Dworak, J. A., Falangas, E. T., Koshigoe, S., Tseng, G.T., 1992, "Methods for Controlling Plate Vibrations Using Piezoelectric Actuators," Falangas, E. T., Dworak, J. A., Koshigoe, S., 1993. They controlled plate vibrations by using 3 control loops with rate and Hinfinty feedback. They feel a combination of active (low freq.) and passive (high freq.) will be most effective since it is much easier to design active controllers for the low frequency modes when the high frequency modes are attenuated passively.

"A New Approach for Active Control of Sound Transmission through an Elastic Plate Backed by a Rectangular Cavity," Koshigoe, S., Gillis, J. T., Falangas, E. T., 1993. A new control method is developed which can control both plate and cavity modes. Plate velocity feedback is only effective for plate controlled modes not the cavity controlled modes. A complete set of equations for the plate-cavity system with PZT's is described. The new approach utilizes sound pressure information inside the cavity. A simulation is performed and shows the new technique reduces both the plate & cavity controlled modes.

"Vibration Control of a Laminated Plate with Piezoelectric Sensor/Actuator: Finite Element Formulation and Modal Analysis," Hwang, W. S., Park, H. C., Hwang, W., 1993. Provides an analytical/numerical solution of a composite plate modeled by Hamilton's principle, being controlled actively (piezoelectric) and passively.

"Graphite/Epoxy Composite Laminates with Co-Cured Interlaminar Damping Layers," Pereira, J. M., 1993. Damping was shown to increase by using a co-cured damping layer on a composite plate.

"Piezoelectric Actuators for Distributed Vibration Excitation of Thin Plates: A Comparison Between Theory and Experiment," Clark, R. L., Flemming, M. R., Fuller, C. R., 1993. Compared the theoretical model of a plate with bonded PZT actuators (Dimitriadis) with an experiment.

"Multiple-mode Piezoelectric Passive Damping Experiments for an Elastic Plate," Browning, D. R. & Wynn, W., 1992. Passively shunted PZT's to reduce plate vibrations at a few modes that had the LCR combination tuned to those frequencies. 20 dB reduction was achieved over 12 modes (100-600 Hz).

"Optimal Placement of Piezoelectric Actuators and Polyvinylidene Fluoride Error Sensors in Active Structural Acoustic Control Approaches," Clark, R. L. & Fuller, C. R., 1992. Discusses the optimal size and location of a piezoelectric actuator and sensor. In controlling structure-borne sound, only those modes with high radiation efficiency must be controlled to obtain significant far-field attenuation. Optimization is performed to actuate the efficient radiators. Significant acoustic radiation occurs at the boundaries of the plate.

"Piezoelectric Actuators for Distributed Vibration Excitation of Thin Plates," Dimitriadis, E. K., Fuller, C. R., Rogers, C. A., 1991. Theoretical and

experimental work is presented on piezoelectric actuators exciting a plate. Geometry of the actuator shape affects the distribution of the modal response and the location of the actuator strongly affects the ability of an actuator to excite certain modes as well as spillover.

"Active Control of Noise Transmission through a Panel into a Cavity: I. Analytical Study," Pan, J., Hansen, C. H., Bies, D. A., 1990. Numerical/analytical study of the control of noise transmitted through a panel via point force actuators. There are two different control mechanisms wrt. sound transmission, panel-controlled modes and cavity-controlled modes.

"Active Control of Sound Transmission/Radiation from Elastic Plates by Vibration Inputs: I. Analysis," Fuller, C. R., 1990. Analytical/numerical study of how one or two point forces can be used to reduce the sound transmitted through a plate. For global attenuation many acoustic control sources are needed even for a monopole source when the control sources are more than $1/4$ wavelength from the noise. 15 dB attenuation of a cylinder can be achieved with one or two control sources. It was found that the number of interior acoustic sources needed to achieve a comparable attenuation is at least twice the circumferential modal order of the interior response.

"Active Control of Structurally Radiated Noise Using Piezoceramic Actuators," Fuller, C. R., Hansen, C. H., Snyder, S. D., 1989. Experimentally have reduced the radiated sound of modes (1,1) and (3,1) by using a PZT patch mounted on a plate. The patch reduced the radiated sound at two tonal frequencies.

Design of, and Initial Experiments with, a MIMO Plate Control Testbed, Daniel G. Cole, Master's Thesis, Virginia Polytechnic Institute and State University, September 1992

Modeling Piezoelectric Materials

IEEE Std 176-1978, IEEE Standard on Piezoelectricity, The Institute of Electrical and Electronic Engineers, 1978.

C. Liang, F. P. Sun and C. A. Rogers, "An impedance method for dynamic analysis of active material systems", ASME Journal of Vibrations and Acoustics, Vol. 116, pp. 120-128, 1994.

Piezoelectric Systems

Design of an Analog Adaptive Piezoelectric Sensoriactuator, Christopher A. Fannin, Master's Thesis, Virginia Polytechnic Institute and State University, February 1997

"Power Factor Correction in Piezoelectric Actuators" by Christopher Niezrecki and Harley H. Cudney; Journal of Intelligent Materials Systems and Structures, Vol. 5-July 1994

Vibration Damping and Control Using Shunted Piezoelectric Materials, George A. Lesieutre, The Shock and Vibration Digest, Vol. 30, No. 3, May 1998 187-195